# Machine-Learning Accelerated Calculations of Reduced Density Matrices

Awwab A. Azam,<sup>1,\*</sup> Lexu Zhao,<sup>2,\*</sup> and Jiabin Yu<sup>2,3,†</sup>

<sup>1</sup>Department of Electrical and Computer Engineering, University of Florida, Gainesville, USA

<sup>2</sup>Department of Physics, University of Florida, Gainesville, Florida 32611, USA

<sup>3</sup>Quantum Theory Project, University of Florida, Gainesville, FL, USA

n-particle reduced density matrices (n-RDMs) play a central role in understanding correlated phases of matter. Yet the calculation of n-RDMs is often computationally inefficient for stronglycorrelated states, particularly when the system sizes are large. In this work, we propose to use neural network (NN) architectures to accelerate the calculation of, and even predict, the n-RDMs for large-size systems. The underlying intuition is that n-RDMs are often smooth functions over the Brillouin zone (BZ) (certainly true for gapped states) and are thus interpolable, allowing NNs trained on small-size n-RDMs to predict large-size ones. Building on this intuition, we devise two NNs: (i) a self-attention NN that maps random RDMs to physical ones, and (ii) a Sinusoidal Representation Network (SIREN) that directly maps momentum-space coordinates to RDM values. We test the NNs in three 2D models: the pair-pair correlation functions of the Richardson model of superconductivity, the translationally-invariant 1-RDM in a four-band model with short-range repulsion, and the translation-breaking 1-RDM in the half-filled Hubbard model. We find that a SIREN trained on a  $6 \times 6$  momentum mesh can predict the  $18 \times 18$  pair-pair correlation function with a relative accuracy of 0.839. The NNs trained on  $6 \times 6 \sim 8 \times 8$  meshes can provide high-quality initial guesses for  $50 \times 50$  translation-invariant Hartree-Fock (HF) and  $30 \times 30$  fully translationbreaking-allowed HF, reducing the number of iterations required for convergence by up to 91.63% and 92.78%, respectively, compared to random initializations. Our results illustrate the potential of using NN-based methods for interpolable n-RDMs, which might open a new avenue for future research on strongly correlated phases.

#### I. INTRODUCTION

Understanding strongly correlated phases of matter has been a central topic in the field of condensed matter physics. The rapid progress of neural-network (NN) methods has created new opportunities for gaining deeper insights into strongly correlated quantum phases via NN-based wavefunction ansatzes which have been applied to various systems including Hubbard model [52–57]. One notable type of such NN ansatze uses the self-attention mechanism [58] to construct correlated orbitals from single-particle orbitals, expressing the many-body wavefunction as a linear combination of a small number of Slater determinants formed from these correlated orbitals [7, 45, 59]. In this work, we propose a different way of using machine learning (or NNs) to understand strongly correlated states—by focusing on their reduced density matrices.

Given a many-body Hamiltonian, the zero-temperature n-particle reduced density matrix (n-RDM) is defined as

$$O_{\mathbf{k}_{1}\alpha_{1},\mathbf{k}_{2}\alpha_{2},...,\mathbf{k}_{n}\alpha_{n},\mathbf{k}'_{1}\alpha'_{1},\mathbf{k}'_{2}\alpha'_{2},...,\mathbf{k}'_{n}\alpha'_{n}} = \left\langle c^{\dagger}_{\mathbf{k}_{1}\alpha_{1}}c^{\dagger}_{\mathbf{k}_{2}\alpha_{2}}...c^{\dagger}_{\mathbf{k}_{n}\alpha_{n}}c_{\mathbf{k}'_{1}\alpha'_{1}}c_{\mathbf{k}'_{2}\alpha'_{2}}...c_{\mathbf{k}'_{n}\alpha'_{n}} \right\rangle ,$$

$$(1)$$

where  $\langle ... \rangle$  represents the average with respect to the ground state(s), and  $c_{\mathbf{k}\alpha}^{\dagger}$  creates a particle with Bloch

momentum k and intra-unit-cell degree of freedom  $\alpha$  (which labels sub-lattice, orbital, spin, etc).

The *n*-RDM plays a vital role in understanding strongly correlated states [60–64]. First, the Hamiltonians of realistic condensed matter systems almost always involve only one-body and two-body terms, implying that the 1-RDM and 2-RDM are sufficient to evaluate the total energy [60, 65, 66]. This observation lies at the heart of semidefinite programming approaches [67–73], which iteratively compute the 2-RDM. Second, the order parameters that characterize spontaneous symmetry breaking—such as charge-density waves and magnetism—often depend only on the 1-RDM [74], which explains the effectiveness of the Hartree-Fock (HF) method [75].

Given the importance of the *n*-RDMs, it would be transformative if we can design a NN that can predict *n*-RDMs for a given Hamiltonian, particularly for large systems where existing algorithms become computationally inefficient. Furthermore, the algorithms that calculate the *n*-RDMs, including the semidefinite programming and the HF algorithm, are often iterative, *i.e.*, they start from a initial guess and iteratively converge to a final result. Thus, even if the designed NN cannot precisely predict the *n*-RDMs, the NN can provide initial guesses that are very close to the converged results, which can dramatically reduce the number of steps needed for convergence.

In this work, we develop two such NNs: (i) a self-attention NN that maps random initial 1-RDMs to the predicted final 1-RDMs, and (ii) a Sinusoidal Representation Network (SIREN) that learns n-RDMs and inter-

<sup>\*</sup> These authors contributed equally to this work.

<sup>†</sup> yujiabin@ufl.edu

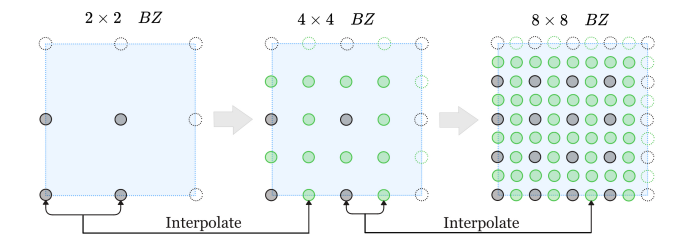


FIG. 1. Interpolability of n-RDMs in the BZ. Momentum meshes for large systems can be generated by inserting new k-points between those of the small momentum meshes. Therefore, n-RDMs in momentum space are often interpolable.

polates them to denser k-meshes. The underlying reason for the existence of such NNs lies in the interpolable nature of n-RDMs (Sec. II). These NNs are trained on small system sizes, where the n-RDMs can be efficiently computed using existing methods, and are then used to predict the n-RDMs of much larger systems. We first benchmark SIREN on the pair-pair correlation functions of the superconducting ground states of the exactly-solvable Richardson model, and find that a SIREN trained only on L=6 can achieve a relative accuracy of 0.839 on L=18 (Sec. B).

We then benchmark the self-attention NN on the translationally-invariant HF calculations for a four-band model with short-range repulsion. Our results show that an NN trained only on L=6,8 can maintain a relatively low mean squared error (MSE, below  $5\times 10^{-3}$ ) for up to L=50. Furthermore, for all L from  $10,12,\ldots 50$ , using the NN predictions as the initial 1-RDM for HF calculations results in a >90% reduction in the number of HF iterations required for convergence compared to the HF calculations with random initialization (Sec. C).

We finally benchmark both NNs on the HF calculations that allow translation breaking in half-filled Hubbard model. We again compare the HF iteration numbers between using the NN-predicted final 1-RDM as initial 1-RDMs and using the random initial 1-RDMs. We find a significant (> 70-90%) reduction in the number of HF iterations for up to L=30 using SIRENs trained only on L=8, and a self-attention NN trained only on L=8,10 (Sec. D). The remarkable reduction in iteration numbers for HF calculations—that forbids and allows translational breaking—demonstrates the potential of NNs for speeding up the calculation of or even the precise prediction of RDMs of large-size systems.

We note that our work is the first to construct NNs that predict large-size n-RDMs that exploits the interpolable structure of n-RDMs in momentum space. Previous developments of NNs for n-RDMs focuses on (i) establishing maps between n-RDM and certain physical quantities and (ii) the n-RDM in real space. [22, 76–80]. Our general idea of using NNs for interpolable n-RDMs, exemplified by our implementations for pair—pair correlation functions and 1-RDMs, might open a new avenue

for studying strongly correlated states.

#### II. INTERPOLABILITY OF n-RDM

In this section, we will first discuss the interpolability of the n-RDM in the BZ. As shown in Eq. (1), the n-RDM is a function of 2n Bloch momenta. For a finite-sized system with periodic boundary condition (which we choose throughout this work), each Bloch momentum takes a number of discrete values. Without loss of generality, let us consider a 2D system with  $L \times L$  unit cells in real space, i.e., L unit cells along the direction of either primitive lattice vector. It means that the Bloch momentum now takes values from an  $L \times L$  momentum mesh. As the system size increases to a larger commensurate value L', additional momentum points emerge in the intermediate regions of the original  $L \times L$  momentum mesh, as illustrated in Fig. 1.

If n-RDM is a smooth function of 2n Bloch momenta in the thermodynamic limit, the values of n-RDM on the extra momentum points can be interpolated from those on original  $L \times L$  momentum grid. In other words, although the n-RDMs are extrapolated from small to large system sizes in real space, they are in fact interpolated in momentum space. The condition that n-RDMs are smooth in the thermodynamic limit is naturally satisfied for gapped ground states. Even when the state of interest is gapless in the thermodynamic limit, certain combinations of n-RDMs (e.g., zero-frequency correlation functions) can still remain smooth functions of the Bloch momenta, such as the pair-pair correlation function in the Richardson model of superconductivity [81] discussed in Sec. B1d and shown in Fig. 7. Therefore, smooth n-RDMs (or smooth combinations thereof) are ubiquitous in condensed matter systems.

This interpolability is crucial for NNs to function effectively, as NNs are well known to be capable of approximating any continuous function to an arbitrary degree of precision (by the Universal Approximation Theorem [82]) when the test data is sampled within the support of the training data distribution (the interpolation regime). In contrast, if the test data is drawn from outside the convex hull of the training set (the extrapolation regime), then NNs cannot generalize reliably in the absence of additional inductive biases or priors (e.g. periodicity or symmetries) on the underlying function [83, 84]. For example, this interpolation of n-RDMs is analogous to image resolution enhancement, where additional pixel values are inferred between existing ones—a task in which NN models have demonstrated strong performance [85]. In the following Sec. III, we discuss two concrete NN architectures designed for the calculation of 1-RDMs (and any quantity that smoothly depends on at most two Bloch momenta).

#### III. NN ARCHITECTURES

We now discuss the NN architectures used in this work. We first focus on the 1-RDM in momentum space, and will discuss the generalization at the end. The general 1-RDM is

$$O_{\mathbf{k}\alpha,\mathbf{k}'\alpha'} = \langle c_{\mathbf{k}\alpha}^{\dagger} c_{\mathbf{k}'\alpha'} \rangle ,$$
 (2)

where  $\alpha$  represents intra-unit-cell degrees of freedom (sublattice, orbital, spin, etc.), taking  $\xi$  values per k, while k, k' ranges over first Brillouin zone (1BZ),

$$\mathbf{k} = \frac{\ell_1}{L} \mathbf{b}_1 + \frac{\ell_2}{L} \mathbf{b}_2, \qquad \ell_{1,2} = 0, \dots, L - 1$$
 (3)

with  $b_{1,2}$  are two primitive reciprocal lattice vectors. We work at fixed momentum transfer q and define

$$O_{\mathbf{k},\alpha\alpha'}^{\mathbf{q}} = O_{\mathbf{k}\alpha,\mathbf{k}+\mathbf{q}\alpha'} . \tag{4}$$

We have q=0 for translation-invariant cases, and we will include more than one q for spontaneous translation-symmetry breaking cases. Regardless of translation symmetry,  $O_{k,\alpha\alpha'}^q$  has dimension  $L \times L \times \xi \times \xi$ .

In this section, we introduce two NN architectures which are trained on small-size  $O^q$  and can predict large-size  $O^q$ . On small sizes, the training data can be generated by existing methods, such as the HF calculation which starts from a random initial 1-RDM and iteratively converges to a final 1-RDM.

#### A. Self-Attention NN

The first NN architecture that we construct is a self-attention model that maps the initial 1-RDM  $O_{\rm init}^{q}$  to a predicted final 1-RDM  $O_{\rm out}^{q}$  that closely approximates the true final 1-RDM  $O_{\rm tgt}^{q}$  from HF calculation.

We train on small L using numerically generated pairs  $\{O_{\mathrm{init}}^{\boldsymbol{q}}(\boldsymbol{k})\}, \{O_{\mathrm{tgt}}^{\boldsymbol{q}}(\boldsymbol{k})\}$  from self-consistent HF. The network learns the fixed-point map over the BZ and produces  $\{O_{\mathrm{out}}^{\boldsymbol{q}}(\boldsymbol{k})\}$ —a convenient initializer for HF at larger L. Fig. 2 shows our pipeline and its components. The overall structure is shown in Fig. 2(a). We first preprocess the 1-RDM  $O_{\boldsymbol{k},\alpha\alpha'}^{\boldsymbol{q}}$  to a standardized real vector,

$$\tilde{\boldsymbol{x}}_i \equiv \tilde{\boldsymbol{x}}^{(\text{init})}(\boldsymbol{k}_i) = \frac{\boldsymbol{x}^{(\text{init})}(\boldsymbol{k}_i) - \mu^{(\text{init})}}{\sigma^{(\text{init})}} \in \mathbb{R}^{2\xi^2},$$
 (5)

where  $\boldsymbol{x}(\boldsymbol{k}_i)$  is the flattened 1-RDM vector of  $O_{\text{init}}^{\boldsymbol{q}}(\boldsymbol{k}_i)$ , and  $\mu^{(\text{init})}, \sigma^{(\text{init})}$  are the mean and standard deviation computed over the training set (Sec. A 1 b). It gives the network a fixed-length, well-conditioned input per momentum point [86, 87].

Then, the standardized  $\tilde{x}_i$  is fed into the self-attention NN. The NN contains N attention layers. The input to the first attention layer is generated by the following. Each  $\tilde{x}_i$  is linearly transformed to a vector  $h_i$  of dimension equal to the model width D:

$$\boldsymbol{h}_i^{(0)} = W_{\text{in}} \tilde{\boldsymbol{x}}_i + \boldsymbol{b}_{\text{in}} \in \mathbb{R}^D, \tag{6}$$

where  $W_{\text{in}} \in \mathbb{R}^{D \times 2\xi^2}$ , and  $\boldsymbol{b}_{\text{in}} \in \mathbb{R}^D$  are learnable, and  $i \in \{1, ..., L^2\}$  labels the BZ site. Stacking the  $L^2$  sites of  $\boldsymbol{h}_i^{(0)}$  row-wise gives the input matrix

$$H^{(0)} = \begin{bmatrix} \left(\boldsymbol{h}_{1}^{(0)}\right)^{\top} \\ \vdots \\ \left(\boldsymbol{h}_{L^{2}}^{(0)}\right)^{\top} \end{bmatrix} \in \mathbb{R}^{L^{2} \times D} , \qquad (7)$$

which is the input for the first attention layer. Then, the  $\ell^{\text{th}}$  attention layer maps  $H^{(\ell-1)} \mapsto H^{(\ell)}$  with l=1,2,..,N. After N attention layers,  $H^{(N)}$  will be converted to  $\widetilde{X}_{out}$ , and we decode it back to  $O_{\text{out}}^{q}(k)$ , which is the predicted final 1–RDM (See Sec. A 1 c).

Within the  $\ell^{\text{th}}$  attention layer, we have an attention block, Dropout+LayerNorm, and a feed-forward network (FFN), as seen in Fig. 2(b). Each attention block uses  $N_{\text{head}}$  parallel heads (Fig. 2(c)); in head h, the per-head width is  $d_k \equiv D/N_{\text{head}}$ . We form the "query"  $(Q^{(h)})$ , "key"  $(K^{(h)})$ , and "value"  $(V^{(h)})$  matrices as

$$Q^{(h)} = H^{(\ell-1)} W_Q^{(h)}, \tag{8}$$

$$K^{(h)} = H^{(\ell-1)}W_K^{(h)}, (9)$$

$$V^{(h)} = H^{(\ell-1)} W_V^{(h)}, \tag{10}$$

with  $W_Q^{(h)}, W_K^{(h)}, W_V^{(h)} \in \mathbb{R}^{D \times d_k}$  learnable matrices. To encode the momentum position information, we add a learnable relative-position bias  $B_{ij}$ , which is a periodic function of  $\mathbf{k}_i - \mathbf{k}_j$ , to the attention logits  $(\Lambda_{ij}^{(h)}$  in Eq. (11)). This bias increases the value of a logit when  $\mathbf{k}_j$  is near  $\mathbf{k}_i$  or related by a lattice symmetry, and decreases it for distant, unrelated pairs (see Sec. A 1 d). Thus, we have for head h

$$\Lambda_{ij}^{(h)} = \tau \frac{\langle Q_i^{(h)}, K_j^{(h)} \rangle + B_{ij}}{\sqrt{d_k}}, \quad \tau \equiv s \log \left( L^2 \right) , \quad (11)$$

which are called the pre-softmax [58, 88] logits, a value whose relative sizes decide the final attention weights  $A_{ij}^{(h)}$  in Eq. (12). Here, the scalable factor s helps to avoid the "attention fading" phenomenon [89] as  $L^2$  grows. The final outputs of the head h are the row-normalized attention weights:

$$A_{ij}^{(h)} = \frac{e^{\tau \Lambda_{ij}^{(h)}}}{\sum_{m=1}^{L^2} e^{\tau \Lambda_{im}^{(h)}}}, \quad \sum_{j} A_{ij}^{(h)} = 1, \quad A_{ij}^{(h)} > 0 , \quad (12)$$

and outputs from all heads are concatenated and projected back to width D to form the output matrix  $Z^{(\ell)}$  of the attention block in the  $\ell^{\text{th}}$  attention layer (Sec. A 1 d).

As labeled in Fig. 2(b), from the attention output  $Z^{(\ell)}$  of the attention block of layer  $\ell$ , we apply dropout, add again  $H^{(\ell-1)}$ , and normalize per k-site (see Sec. A 1 e):

$$\hat{Z}^{(\ell)} = \text{Dropout}(Z^{(\ell)}), \tag{13}$$

$$U^{(\ell)} = \text{LayerNorm}(H^{(\ell-1)} + \hat{Z}^{(\ell)}) \in \mathbb{R}^{L^2 \times D}.$$
 (14)

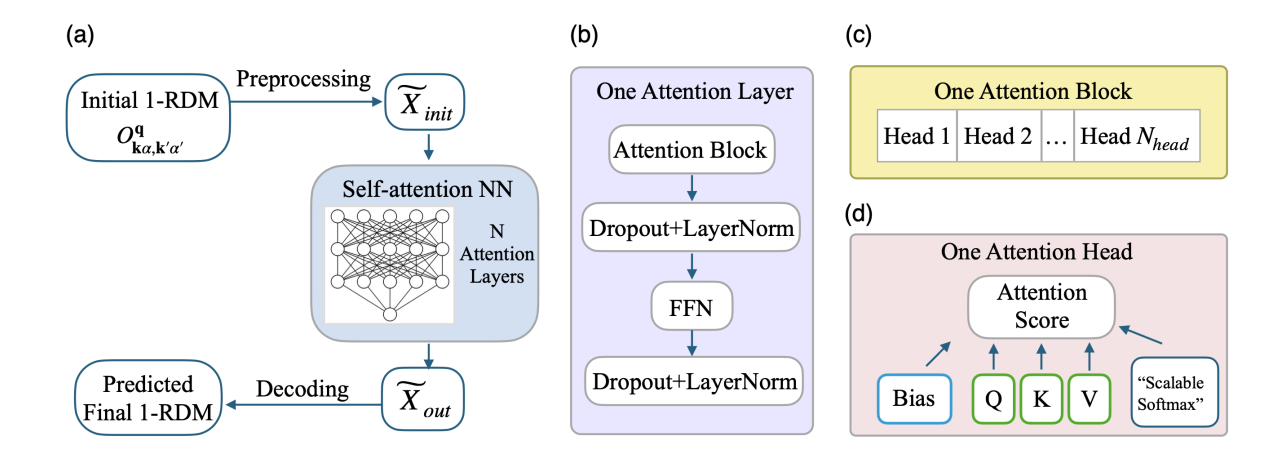


FIG. 2. Schematics of our self-attention NN. (a) An initial 1–RDM on an  $L \times L$  BZ is preprocessed to  $\tilde{X}_{\rm init}$ , transformed by the network to  $\tilde{X}_{\rm out}$ , and decoded to the predicted final 1–RDM. (b) Each layer applies an attention block and a FFN with Dropout and LayerNorm. (c) The attention block includes  $N_{\rm head}$  parallel heads. (d) Each head uses Q, K, V with a learned periodic relative-position bias and a scalable softmax temperature (e.g.,  $\tau \propto \log L^2$ ).

Dropout independently sets each entry of  $\hat{Z}^{(l)}$  to zero with some fixed probability p and keeps it with probability 1-p during training [90]. LayerNorm acts rowwise (per  $\mathbf{k}_i$ ) on  $H^{(\ell-1)}+\hat{Z}^{(\ell)}$  across the D components: letting  $U_i\equiv \left[H^{(\ell-1)}+\hat{Z}^{(\ell)}\right]_{i,:}\in\mathbb{R}^D$ , it subtracts the row mean  $\mu_i$  and divides by the row standard deviation  $\sqrt{\sigma_i^2+\epsilon}$  (with a small  $\epsilon>0$ ) over dimension D, then applies learnable scale  $\gamma$ , shift  $\beta$ , yielding the element-wise product  $\gamma\odot\frac{U_i-\mu_i\mathbf{1}}{\sqrt{\sigma_i^2+\epsilon}}+\beta$ . Then, our FFN takes  $U^{(\ell)}$ , applies a linear map, then a GELU (Gaussian Error Linear Unit) that improves optimization stability [91, 92] (see details in Sec. A 1 e), and another linear map back to the model width D, producing  $\hat{U}^{(\ell)}$ . Finally, the output of the layer is:

$$H^{(\ell)} = \text{LayerNorm}(U^{(l)} + \text{Dropout}(\hat{U}^{(l)})).$$
 (15)

#### B. SIREN

The second NN structure we use is SIREN, a network that represents the 1–RDM as a smooth, periodic function of k-coordinates, enabling evaluation on denser k-meshes by interpolation. The overall structure of this NN architecture is shown in Fig. 3(a). We first map BZ k-points (Eq. (3)) to normalized coordinates

$$\mathbf{v}(\mathbf{k}) = \left(2\frac{\ell_1}{L} - 1, 2\frac{\ell_2}{L} - 1\right) \in [-1, 1]^2.$$
 (16)

Then, for each fixed  $(\alpha, \alpha')$ , the real and imaginary parts of  $O_{\mathbf{k},\alpha\alpha'}^{\mathbf{q}}$  is a real function of  $\mathbf{v}$ , and we train a scalar function  $\Phi_{\theta}$  with  $\theta$  representing all trainable parameters  $\theta$  such that

$$\Phi_{\theta}(\boldsymbol{v}) \approx \text{Re}[O_{\alpha\alpha'}^{\boldsymbol{q}}(\boldsymbol{k})] \text{ or } \text{Im}[O_{\alpha\alpha'}^{\boldsymbol{q}}(\boldsymbol{k})].$$
(17)

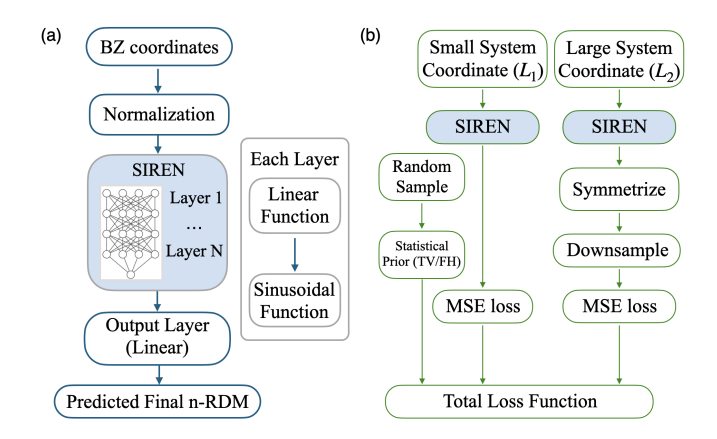


FIG. 3. Schematic of our SIREN. (a) Normalize BZ coordinates to  $v(k) \in [-1,1]^2$ , then pass v through layers of linear and sine functions to predict one component of the final n-RDM (e.g., a specific  $\alpha, \alpha'$  component for 1-RDM); aggregating components reconstructs the predicted final n-RDM. (b) We train the NN using a total loss that contains: (i) MSE on the small  $L_1 \times L_1$  mesh, and (ii) a loss computed by evaluating SIREN on a larger mesh  $L_2 \times L_2$ , symmetrizing, downsampling back to  $L_1 \times L_1$  and comparing to the true final RDMs on the  $L_1 \times L_1$  mesh. At each step we evaluate a statistical prior (TV or FH) on randomly chosen coordinates  $u_i \in [-1,1]^2$  to regularize the SIREN. Therefore, the training only invariants true final RDMs on the small  $L_1 \times L_1$  mesh.

Specifically, we construct  $\Phi_{\theta}$  using 4 sinusoidal hidden layers followed by a linear function:

$$h_{1}(\mathbf{v}) = \sin \left(6 \left(W_{1}\mathbf{v} + \mathbf{b}_{1}\right)\right) ,$$

$$h_{2}(\mathbf{v}) = \sin \left(30 \left(W_{2}\mathbf{h}_{1}(\mathbf{v}) + \mathbf{b}_{2}\right)\right) ,$$

$$h_{3}(\mathbf{v}) = \sin \left(30 \left(W_{3}\mathbf{h}_{2}(\mathbf{v}) + \mathbf{b}_{3}\right)\right) ,$$

$$h_{4}(\mathbf{v}) = \sin \left(30 \left(W_{4}\mathbf{h}_{3}(\mathbf{v}) + \mathbf{b}_{4}\right)\right) ,$$

$$\Phi_{\theta}(\mathbf{v}) = \mathbf{w}^{\top}\mathbf{h}_{4}(\mathbf{v}) + b_{\text{out}}$$

$$(18)$$

with  $\boldsymbol{v} \in [-1,1]^2, W_1 \in \mathbb{R}^{d_H \times 2}, W_2, W_3, W_4 \in \mathbb{R}^{d_H \times d_H}, \boldsymbol{b}_1 \boldsymbol{b}_2, \boldsymbol{b}_3, \boldsymbol{b}_4 \in \mathbb{R}^{d_H}, \boldsymbol{w} \in \mathbb{R}^{d_H}, b_{\text{out}} \in \mathbb{R}$ . (see Sec. A 2 d). This is SIREN, which naturally captures the smooth, periodic structure of  $O^q(\boldsymbol{k})$  across the BZ.

We train  $\Phi_{\theta}$  that maps normalized BZ coordinates  $v(k) \in [-1,1]^2$  to one component of the true final 1-RDM. For each component (and, when applicable, its real/imag part), we prepare small-mesh data by enforcing periodic boundary consistency and standardizing (Eq. (A52)). The loss has three parts (Fig. 3(b)): (i) a mean-squared error (MSE) on the system of small size  $L_1$ , (ii) a consistency term that evaluates  $\Phi_{\theta}$  on a denser mesh of size  $L_2$ , averages over a chosen symmetry subgroup  $G \subset D_4$ , downsamples back to  $L_1 \times L_1$ , and compares to the  $L_1 \times L_1$  true final 1-RDMs, and (iii) a random sampler where TV/Hessian regularization may be added. We penalize the discrepancy through the combined total loss function (see Sec. A2d). The training only invariants true final 1-RDMs on the small  $L_1 \times L_1$  mesh. After training, we evaluate  $\Phi_{\theta}$  on v coordinates, then invert the standardization in Eq. (A53) and assemble the real and imaginary parts of  $O^{q}(\mathbf{k}_{i})$  with all  $(\alpha, \alpha')$  for each  $\mathbf{k}_{i}$ to recover the predicted final 1-RDM on arbitrary mesh sizes.

#### C. Beyond 1-RDM

The two NN structures can be straightforwardly generalized to any special combination of n-RDM (with n>1) that only depends on one Bloch momentum, just like  $O_{k,\alpha\alpha'}^q$ . Beyond one-momentum quantities, the SIREN can be applied to the pair-pair correlation function (special 2-RDM) for superconductors, which depends on two momenta, as we will show in Sec. IV. In general, we expect the SIREN can be naturally used for quantities that depend on more than two momenta. The generalization of self-attention NN to quantities that depend on more than 1 momenta might require more effort as the self-attention mechanism naturally has quadratic time and space complexity which we leave for future work.

#### IV. PAIR-PAIR CORRELATION FUNCTIONS

In this section, we will apply the NN on the pairpairing correlation function for superconductivity. As a benchmark, we consider the exactly-solvable Richardson model [93-95]

$$H = \sum_{\mathbf{k},s} \varepsilon_{\mathbf{k}} c_{\mathbf{k}s}^{\dagger} c_{\mathbf{k}s} + \frac{u}{L^{2}} \left( \sum_{\mathbf{k}} A_{\mathbf{k}}^{\dagger} \right) \left( \sum_{\mathbf{k}'} A_{\mathbf{k}'} \right) , \quad (19)$$

where  $L^2$  is the number of lattice sites, u<0 is the attractive interaction strength,  $c_{\mathbf{k}s}^{\dagger}$  creates an electron with Bloch momentum  $\mathbf{k}$  and spin s. We work in the number-conserving case, where the pair–pair correlation function is just the Cooper–channel matrix channel of 2-RDM

$$C_{\boldsymbol{k}\boldsymbol{k}'} = O_{\boldsymbol{k}\uparrow,-\boldsymbol{k}\downarrow,\boldsymbol{k}'\uparrow,-\boldsymbol{k}'\downarrow} = \left\langle A_{\boldsymbol{k}}^{\dagger} A_{\boldsymbol{k}'} \right\rangle, \quad A_{\boldsymbol{k}}^{\dagger} \equiv c_{\boldsymbol{k}\uparrow}^{\dagger} c_{-\boldsymbol{k}\downarrow}^{\dagger},$$
(20)

as  $\langle A_{\mathbf{k}} \rangle = 0$ . Since  $C_{\mathbf{k}\mathbf{k}'}$  depends on two momenta, we use it as a testbed to assess the ability of our SIREN NN (discussed in Sec. III B) to learn and interpolate  $C_{\mathbf{k}\mathbf{k}'}$  across BZ grids, which is also a benchmark for our general idea. We exactly solve Eq. (19) with u = -1, electron filling  $\nu = 1/4$ , and  $\varepsilon_{\mathbf{k}} = t(\cos k_x + \cos k_y)$  with t = 0.1, and generate the truth final  $C_{\mathbf{k}\mathbf{k}'}$  for the fully paired ground state from the analytic solution for L up to 18 (see details in Sec. B).

These exact  $C_{kk'}$  values are used to train and validate our SIREN: We train the NN on the true final  $C_{kk'}$  of small L and test it against the true final  $C_{kk'}$  of larger L.

We trained two SIRENs (Sec. III B) on  $C_{kk'}$ : one was trained on L=6 and tested on  $L=8,10,\ldots 18$ , and the other was trained on L=10 and tested on  $L=12,\ldots 18$ . Results are shown in Tab. I. To evaluate performance, we use the relative accuracy  $r_n$ , defined by

$$r_n = \left(1 - \frac{\sqrt{\text{MSE}}}{\max(C) - \min(C)}\right) \tag{21}$$

(see MSE in Sec. B2). A comparison between the predicted final  $C_{kk'}$  from the SIREN trained on L=6 and the true final  $C_{kk'}$  for L=18 is shown in Fig. 4. We see that the SIREN trained on small size (e.g., L=6) can predict the  $C_{kk'}$  at large size (e.g., L=18) with a rather high accuracy  $(e.g., r_n=0.839)$ . It is reasonable that when we train the SIREN on a larger size L=10, the prediction accuracy increases significantly (to 0.9189). These results clearly verify the validity of using the SIREN trained on small sizes to predict RDMs on large sizes.

# V. TRANSLATIONALLY-INVARIANT HF

We further benchmark our self-attention NN on translationally-invariant 1-RDM. The final true 1-RDM is calculated by HF algorithm starting from random initial 1-RDM.

The model we consider is a  $L \times L$  square lattice with one atom per unit cell. At site r, we have a four-component

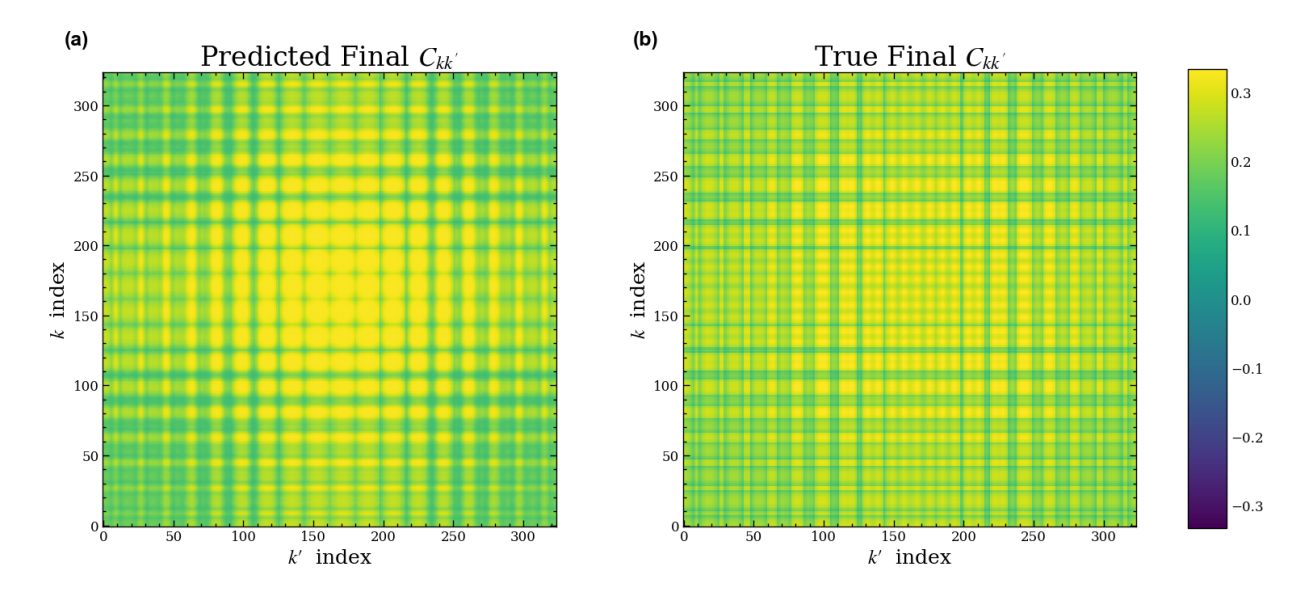


FIG. 4. Comparison between (a) the predicted final L=18  $C_{kk'}$  given by a SIREN trained on L=6 and (b) the true final  $C_{kk'}$  for L=18. Here the indices  $k,k'\in\{0,\ldots,L^2-1\}$  enumerate the  $L\times L$  BZ points by flattening  $(\ell_1,\ell_2)$  with  $\ell_{1,2}\in\{0,\ldots,L-1\}$  via  $k=\ell_1+L$   $\ell_2$ ; the corresponding momentum vector is k given in Eq. (3), and similarly for k'.

$\overline{L}$	$L_{ ext{train}}$	n = 6	$L_{\text{train}} = 10$			
	$\sqrt{\mathrm{MSE}}$	$r_n$	$\sqrt{\text{MSE}}$	$r_n$		
8	0.0779	0.7084	_	_		
10	0.0223	0.9068	_	_		
12	0.0735	0.6806	0.0750	0.6744		
14	0.0284	0.8699	0.0112	0.9487		
16	0.0715	0.6678	0.0715	0.6678		
18	0.0345	0.8390	0.0174	0.9189		

TABLE I. Pair-Pair Correlation function of Richardson model interpolation with SIREN. Metrics at evaluation mesh size  $L \times L$  for models trained on small meshes  $L_{\text{train}} = 6$  and  $L_{\text{train}} = 10$ . Columns report root-mean-square error  $(\sqrt{\text{MSE}})$  and relative accuracy  $(r_n)$  between SIREN predictions and true final 2-RDM on the evaluation mesh.

spinor  $\psi_{\boldsymbol{r}} = (\psi_{\boldsymbol{r},1}, \dots, \psi_{\boldsymbol{r},4})^\mathsf{T}$ , and the Hamiltonian reads

$$H = H_0 + H_{\text{int}}$$

$$= \sum_{r} \psi_{r}^{\dagger} h(\mathbf{0}) \psi_{r} + \sum_{r} \sum_{\delta \neq \mathbf{0}} \left( \psi_{r+\delta}^{\dagger} h(\delta) \psi_{r} + \text{h.c.} \right)$$

$$+ \frac{1}{2} \sum_{r} \sum_{\mathbf{R}} V(\mathbf{R}) n_{r} n_{r+\mathbf{R}}$$
(22)

where  $n_{r} = \psi_{r}^{\dagger} \psi_{r}$ , Bravais lattice vector  $\mathbf{R}$ , and the interaction is short ranged

$$V(\mathbf{R}) = U_0 \left[ \delta_{\mathbf{R},\mathbf{0}} + \frac{1}{2} \left( \delta_{\mathbf{R},\hat{\mathbf{x}}} + \delta_{\mathbf{R},-\hat{\mathbf{x}}} + \delta_{\mathbf{R},\hat{\mathbf{y}}} + \delta_{\mathbf{R},-\hat{\mathbf{y}}} \right) \right].$$
(23)

We choose the hopping such that the lower two single-particle bands have a nontrivial time-reversal–invariant  $\mathbb{Z}_2$  topology [96] (Sec. C1).

We perform the translationally-invariant HF calculations at filling  $\nu = 1$  for L = 6, 8, 10, 12, ... 50. Using this data, we train a self-attention NN on 10,000 (initial 1-RDM, true final 1-RDM) pairs for each of L=6,8 (see Sec. C). In order to evaluate its effectiveness, we feed 1,000 random initial 1-RDMs for each of  $L = 10, 12, \dots 50$  into the trained NN to obtain the corresponding predicted final 1-RDMs. We then use those predicted final 1-RDMs as initial conditions for the HF calculation and record the number of iterations to converge, and compare it with HF started from a random initialization. Particularly, we find that it takes an average of 8.057 iteration steps to converge when using the predicted final 1-RDMs for L = 50 as the initial 1-RDMs for HF, as compared to an average of 96.301 iterations with random initial 1-RDMs. Thus, our NN, when trained on L=6,8, results in a 91.63% reduction in the number of iterations required for HF convergence for L=50. In general, we define the percent reduction as:

$$\% \ \ Reduction = \frac{iters(random \ init) - iters(NN \ init)}{iters(random \ init)} \times 100, \eqno(24)$$

where "iters(random init)" refers to the average number of HF iterations when starting from a random initial 1-RDM and "iters(NN init)" refers to the average number of HF iterations when starting from the NN-predicted final 1-RDM. The percent reduction for other system sizes is shown in Fig. 5. Notably, they are all above 90% (see Sec. C for details).

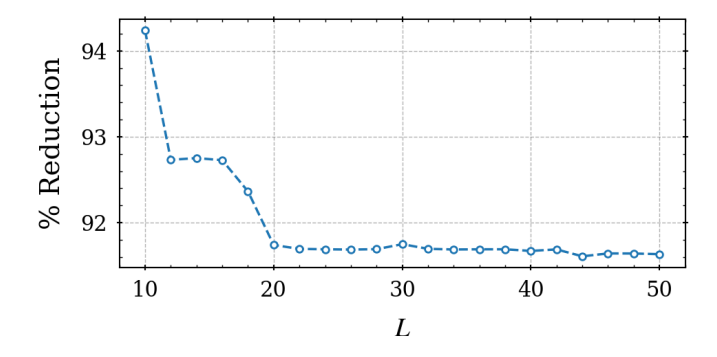


FIG. 5. **NN** for translation-invariant **HF**. Here, "% Reduction" is defined in Eq. (24), (i.e. the percent difference between the number of HF iterations using a predicted final 1-RDM from the self-attention NN as the initial 1-RDM as compared to using a random initial 1-RDM), and is plotted as a function of the system size L for the four-band model described in Eqs. (22) and (23). See Tab. V in Sec. C for the exact values. The HF calculation is forced to preserve the lattice translation symmetry.

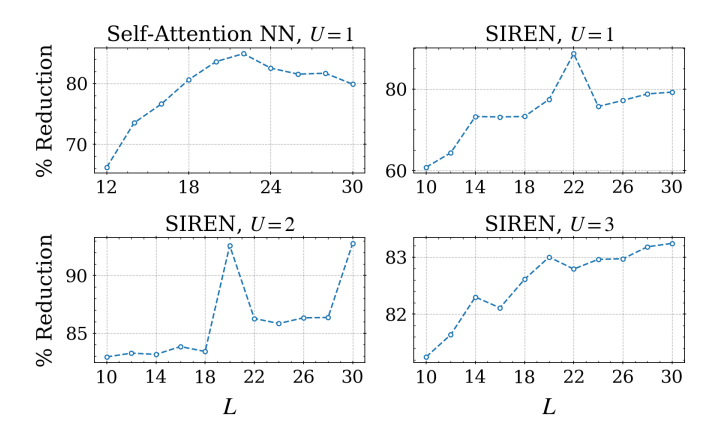


FIG. 6. NN for the Hubbard model. Summary of results for the Hubbard model using a self-attention NN (U=1) and SIRENs (U=1,2,3) showing the percent reduction (as defined in Eq. (24)) in the number of HF iterations as a function of the system size L. See Tab. VII in Sec. D for the exact values. The HF calculations here allow any kind of breaking of lattice translation symmetries that are compatible with the momentum mesh.

# VI. HF ALLOWING TRANSLATIONAL BREAKING

Finally, we benchmark both NNs for HF calculations that allow any kind of translation breaking that is compatible with the momentum meshes. We focus on the Hubbard model on a 2D square lattice [97, 98],

$$H = -t \sum_{\langle \boldsymbol{r}, \boldsymbol{r}' \rangle, \sigma} \left( c_{\boldsymbol{r}\sigma}^{\dagger} c_{\boldsymbol{r}'\sigma} + \text{h.c.} \right) + U \sum_{\boldsymbol{r}} n_{\boldsymbol{r}\uparrow} n_{\boldsymbol{r}\downarrow}, \quad (25)$$

with  $n_{r\sigma} = c_{r\sigma}^{\dagger} c_{r\sigma}$  and  $c_{r\sigma}^{\dagger}$  creates an electron at site r and spin  $\sigma$ . We consider the half filling and assume that a spin U(1) is conserved. Then, the 1-RDM that serves

as the order parameters is spin-resolved

$$[O_{\sigma}]_{kk'} = \langle c_{k'\sigma}^{\dagger} c_{k\sigma} \rangle, \quad \sigma \in \{\uparrow, \downarrow\} ,$$
 (26)

where  $c_{\boldsymbol{k}\sigma}^{\dagger}$  is the Fourier transform of  $c_{\boldsymbol{r}\sigma}^{\dagger}$  with  $\boldsymbol{k}$  the Bloch momentum. Clearly, Tr  $[O_{\sigma}^{\boldsymbol{q}}] = N_{\text{occ},\sigma}$  is the number of electrons with spin  $\sigma$ . Since we consider the half filling, we choose  $N_{\text{occ},\uparrow} = N_{\text{occ},\downarrow}$ , and perform HF calculations for  $L=8,10,\ldots,20,\ t=1$  and U=1,2,3. The lowest-energy converged  $[O_{\sigma}]_{\boldsymbol{k}\boldsymbol{k}'}$  are not zero only when  $\boldsymbol{k}'-\boldsymbol{k}$  is  $(\pi,\pi)$  and (0,0), which is consistent with the  $(\pi,\pi)$ -antiferromagnetism at half filling [99].

We train both a self-attention NN and a SIREN. The self-attention NN was trained on L=8 and L=10 for U=1 only (due to limited training data), and tested on  $L=12,\ldots 30$ . The SIRENs were trained on L=8 for U=1,2,3, and tested on  $L=10,\ldots 30$ . For the tests, we again compute the percent reduction in the number of HF iterations using the predicted final 1-RDM as the initial guess versus using a random initial 1-RDM. Fig. 6 shows the percent reduction plotted as a function of L. Particularly, for the case where U=2, it takes an average of 41.53 HF iterations to converge for L = 30 using a random initial 1-RDM. However, when using the predicted final 1-RDM from SIRENs trained on L = 8, it takes only 3 iterations to converge, which implies a 92.78% reduction in the number of HF iterations. Similarly, for U=1 the percent reduction is 79.89% for L=30 using a self-attention NN trained on L=8,10 and 79.25% when using SIRENs trained only on L=8, while for U=3 we obtain an 83.24% reduction in the number of iterations using SIRENs (also trained on L=8 only). This dramatic reduction verifies the efficiency of our NNs (more details in Sec. Ds).

#### VII. CONCLUSION AND DISCUSSION

In summary, we showed that the large-size n-RDMs can be predicted by NNs trained on small-size n-We benchmark two NNs, the self-attention RDMs. NN and SIREN, for the pair-pair correlation function in the Richardson model (SIREN), the translationallyinvariant HF in a four-band model (self-attention NN), and the translationally-breaking-allowed HF in the Hubbard model (self-attention NN and SIREN), and we find remarkable precision in the NN predictions. One immediate step is to use these NNs to help predict new correlated states in other systems. Certainly, the development of NNs for general 2-RDMs (or n-RDM with n > 2) is an important future direction. For example, the NN for the general 2-RDMs will dramatically help accelerate the energy of any Hamiltonian with up to two-body interactions, which are ubiquitous in condensed matter physics.

## VIII. ACKNOWLEDGMENTS

J.Y.'s work is supported by startup funds at University of Florida. A.A.'s work is supported by the AI Scholars program (part of the University Scholars Program) at the University of Florida, as well as by the UF Center for Condensed Matter Sciences (CCMS) Undergraduate Fellowship. The authors acknowledge UFIT Research Computing for providing computational resources and support.

- [1] G. Carleo and M. Trover, Science **355**, 602–606 (2017).
- [2] Y. Nomura, A. S. Darmawan, Y. Yamaji, and M. Imada, Physical Review B 96, 10.1103/physrevb.96.205152 (2017).
- [3] I. Glasser, N. Pancotti, M. August, I. D. Rodriguez, and J. I. Cirac, Physical Review X 8, 10.1103/physrevx.8.011006 (2018).
- [4] D. Luo and B. K. Clark, Phys. Rev. Lett. 122, 226401 (2019).
- [5] K. Choo, T. Neupert, and G. Carleo, Physical Review B 100, 10.1103/physrevb.100.125124 (2019).
- [6] N. Irikura and H. Saito, Physical Review Research 2, 10.1103/physrevresearch.2.013284 (2020).
- [7] D. Pfau, J. S. Spencer, A. G. D. G. Matthews, and W. M. C. Foulkes, Phys. Rev. Res. 2, 033429 (2020).
- [8] M. Hibat-Allah, M. Ganahl, L. E. Hayward, R. G. Melko, and J. Carrasquilla, Physical Review Research 2, 10.1103/physrevresearch.2.023358 (2020).
- [9] D. Pfau, J. S. Spencer, A. G. D. G. Matthews, and W. M. C. Foulkes, Physical Review Research 2, 10.1103/physrevresearch.2.033429 (2020).
- [10] O. Sharir, Y. Levine, N. Wies, G. Carleo, and A. Shashua, Physical Review Letters 124, 10.1103/physrevlett.124.020503 (2020).
- [11] J. Hermann, Z. Schätzle, and F. Noé, Nature Chemistry 12, 891–897 (2020).
- [12] D. Pfau, J. S. Spencer, A. G. D. G. Matthews, and W. M. C. Foulkes, Phys. Rev. Res. 2, 033429 (2020).
- [13] K. Inui, Y. Kato, and Y. Motome, Phys. Rev. Res. 3, 043126 (2021).
- [14] G. Pescia, J. Han, A. Lovato, J. Lu, and G. Carleo, Phys. Rev. Res. 4, 023138 (2022).
- [15] X. Li, C. Fan, W. Ren, and J. Chen, Fermionic neural network with effective core potential (2021), arXiv:2108.11661 [physics.chem-ph].
- [16] D. Luo, G. Carleo, B. K. Clark, and J. Stokes, Physical Review Letters 127, 10.1103/physrevlett.127.276402 (2021).
- [17] C. K. Lee, P. Patil, S. Zhang, and C. Y. Hsieh, Physical Review Research 3, 10.1103/physrevresearch.3.023095 (2021).
- [18] C. Adams, G. Carleo, A. Lovato, and N. Rocco, Physical Review Letters 127, 10.1103/physrevlett.127.022502 (2021).
- [19] M. Scherbela, R. Reisenhofer, L. Gerard, P. Marquetand, and P. Grohs, Solving the electronic schrödinger equation for multiple nuclear geometries with weightsharing deep neural networks (2021), arXiv:2105.08351 [physics.comp-ph].
- [20] J. Robledo Moreno, G. Carleo, A. Georges, and J. Stokes, Proceedings of the National Academy of Sciences 119, 10.1073/pnas.2122059119 (2022).
- [21] G. Pescia, J. Han, A. Lovato, J. Lu, and G. Carleo, Physical Review Research 4, 10.1103/physrevre-

- search.4.023138 (2022).
- [22] H. Li, Z. Wang, N. Zou, M. Ye, R. Xu, X. Gong, W. Duan, and Y. Xu, Nature Computational Science 2, 367–377 (2022).
- [23] X. Li, Z. Li, and J. Chen, Nature Communications 13, 7895 (2022).
- [24] I. L. Gutiérrez and C. B. Mendl, Quantum 6, 627 (2022).
- [25] D. R. Vivas, J. Madroñero, V. Bucheli, L. O. Gómez, and J. H. Reina, Neural-network quantum states: A systematic review (2022), arXiv:2204.12966 [quant-ph].
- [26] D. Luo, S. Yuan, J. Stokes, and B. K. Clark, Gauge equivariant neural networks for 2+1d u(1) gauge theory simulations in hamiltonian formulation (2022), arXiv:2211.03198 [hep-lat].
- [27] Z. Chen, D. Luo, K. Hu, and B. K. Clark, Simulating 2+1d lattice quantum electrodynamics at finite density with neural flow wavefunctions (2022), arXiv:2212.06835 [hep-lat].
- [28] J. M. Martyn, K. Najafi, and D. Luo, Physical Review Letters 131, 10.1103/physrevlett.131.081601 (2023).
- [29] G. Cassella, H. Sutterud, S. Azadi, N. Drummond, D. Pfau, J. S. Spencer, and W. Foulkes, Physical Review Letters 130, 10.1103/physrevlett.130.036401 (2023).
- [30] M. Wilson, S. Moroni, M. Holzmann, N. Gao, F. Wudarski, T. Vegge, and A. Bhowmik, Physical Review B 107, 10.1103/physrevb.107.235139 (2023).
- [31] W. Ren, W. Fu, X. Wu, and J. Chen, Nature Communications 14, 10.1038/s41467-023-37609-3 (2023).
- [32] C. Roth, A. Szabó, and A. H. MacDonald, Physical Review B 108, 10.1103/physrevb.108.054410 (2023).
- [33] R. Li, H. Ye, D. Jiang, X. Wen, C. Wang, Z. Li, X. Li, D. He, J. Chen, W. Ren, and L. Wang, Forward laplacian: A new computational framework for neural network-based variational monte carlo (2023), arXiv:2307.08214 [physics.comp-ph].
- [34] D. Luo, D. Dai, and L. Fu, Pairing-based graph neural network for simulating quantum materials (2023), arXiv:2311.02143 [cond-mat.str-el].
- [35] J. Kim, G. Pescia, B. Fore, J. Nys, G. Carleo, S. Gandolfi, M. Hjorth-Jensen, and A. Lovato, Neuralnetwork quantum states for ultra-cold fermi gases (2023), arXiv:2305.08831 [cond-mat.quant-gas].
- [36] I. von Glehn, J. S. Spencer, and D. Pfau, A self-attention ansatz for ab-initio quantum chemistry (2023), arXiv:2211.13672 [physics.chem-ph].
- [37] Y. Teng, D. D. Dai, and L. Fu, Solving and visualizing fractional quantum hall wavefunctions with neural network (2024), arXiv:2412.00618 [cond-mat.str-el].
- [38] G. Pescia, J. Nys, J. Kim, A. Lovato, and G. Carleo, Physical Review B 110, 10.1103/physrevb.110.035108 (2024).
- [39] Y. Qian, T. Zhao, J. Zhang, T. Xiang, X. Li, and J. Chen, Physical Review Letters 134, 10.1103/physrevlett.134.176503 (2025).

- [40] G. Goldshlager, N. Abrahamsen, and L. Lin, Journal of Computational Physics 516, 113351 (2024).
- [41] W. T. Lou, H. Sutterud, G. Cassella, W. Foulkes, J. Knolle, D. Pfau, and J. S. Spencer, Physical Review X 14, 10.1103/physrevx.14.021030 (2024).
- [42] Z. Chen, L. Newhouse, E. Chen, D. Luo, and M. Soljačić, Antn: Bridging autoregressive neural networks and tensor networks for quantum many-body simulation (2024), arXiv:2304.01996 [quant-ph].
- [43] Z. Chen and J. Lu, Exact and efficient representation of totally anti-symmetric functions (2025), arXiv:2311.05064 [math.CA].
- [44] X. Li, Y. Chen, B. Li, H. Chen, F. Wu, J. Chen, and W. Ren, Deep learning sheds light on integer and fractional topological insulators (2025), arXiv:2503.11756 [cond-mat.str-el].
- [45] M. Geier, K. Nazaryan, T. Zaklama, and L. Fu, Physical Review B 112, 10.1103/qxc3-bkc7 (2025).
- [46] I. Romero, J. Nys, and G. Carleo, Communications Physics 8, 10.1038/s42005-025-01955-z (2025).
- [47] M. Geier, K. Nazaryan, T. Zaklama, and L. Fu, Is attention all you need to solve the correlated electron problem? (2025), arXiv:2502.05383 [cond-mat.str-el].
- [48] D. Luo, T. Zaklama, and L. Fu, Solving fractional electron states in twisted mote<sub>2</sub> with deep neural network (2025), arXiv:2503.13585 [cond-mat.str-el].
- [49] D. Luo, T. Zaklama, and L. Fu, Solving fractional electron states in twisted mote<sub>2</sub> with deep neural network (2025), arXiv:2503.13585 [cond-mat.str-el].
- [50] Y. Gu, W. Li, H. Lin, B. Zhan, R. Li, Y. Huang, D. He, Y. Wu, T. Xiang, M. Qin, L. Wang, and D. Lv, Solving the hubbard model with neural quantum states (2025), arXiv:2507.02644 [cond-mat.str-el].
- [51] L. Fu, A minimal and universal representation of fermionic wavefunctions (fermions = bosons + one) (2025), arXiv:2510.11431 [cond-mat.str-el].
- [52] Y. Nomura, A. S. Darmawan, Y. Yamaji, and M. Imada, Phys. Rev. B 96, 205152 (2017).
- [53] K. Ch'ng, J. Carrasquilla, R. G. Melko, and E. Khatami, Phys. Rev. X 7, 031038 (2017).
- [54] D. Luo and B. K. Clark, Phys. Rev. Lett. 122, 226401 (2019).
- [55] E. Ibarra-García-Padilla, H. Lange, R. G. Melko, R. T. Scalettar, J. Carrasquilla, A. Bohrdt, and E. Khatami, Physical Review Research 7, 10.1103/physrevresearch 7,013122 (2025).
- [56] K. Choo, G. Carleo, N. Regnault, and T. Neupert, Phys. Rev. Lett. 121, 167204 (2018).
- [57] N. Irikura and H. Saito, Phys. Rev. Res. 2, 013284 (2020).
- [58] A. Vaswani, N. Shazeer, N. Parmar, J. Uszkoreit, L. Jones, A. N. Gomez, L. Kaiser, and I. Polosukhin, Attention is all you need (2023), arXiv:1706.03762 [cs.CL].
- [59] I. von Glehn, J. S. Spencer, and D. Pfau, A self-attention ansatz for ab-initio quantum chemistry (2023), arXiv:2211.13672 [physics.chem-ph].
- [60] A. J. Coleman, Rev. Mod. Phys. 35, 668 (1963).
- [61] D. A. Mazziotti, Phys. Rev. Lett. 108, 263002 (2012).
- [62] D. A. Mazziotti, Chemical Reviews 112, 244 (2012).
- [63] D. A. Mazziotti, Accounts of Chemical Research 39, 207 (2006).
- [64] A. E. I. DePrince, WIREs: Computational Molecular Science 14, e1702 (2024).

- [65] A. E. D. III, Variational determination of the twoelectron reduced density matrix: A tutorial review (2023), arXiv:2310.10746 [physics.chem-ph].
- [66] C. Garrod and J. K. Percus, Journal of Mathematical Physics 5, 1756 (1964).
- [67] D. A. Mazziotti, Accounts of Chemical Research 39, 207 (2006).
- [68] D. A. Mazziotti, Phys. Rev. Lett. 93, 213001 (2004).
- [69] D. A. Mazziotti, Phys. Rev. Lett. 106, 083001 (2011).
- [70] M. G. Scheer, Hamiltonian bootstrap (2024) arXiv:2410.00810 [cond-mat.str-el].
- [71] Z. Zhao, B. J. Braams, M. Fukuda, M. L. Overton, and J. K. Percus, The Journal of Chemical Physics 120, 2095 (2004).
- [72] M. Nakata, H. Nakatsuji, M. Ehara, M. Fukuda, K. Nakata, and K. Fujisawa, The Journal of Chemical Physics 114, 8282 (2001).
- [73] D. A. Mazziotti, Phys. Rev. A 72, 032510 (2005).
- [74] K. J. Giesbertz and M. Ruggenthaler, Physics Reports 806, 1–47 (2019).
- [75] A. Szabo and N. S. Ostlund, Modern Quantum Chemistry: Introduction to Advanced Electronic Structure Theory (Dover Publications, 1989).
- [76] X. Shao, L. Paetow, M. E. Tuckerman, and M. Pavanello, Machine learning electronic structure methods based on the one-electron reduced density matrix (2023), arXiv:2302.10741 [physics.chem-ph].
- [77] K. Ma, C. Yang, J. Zhang, Y. Li, G. Jiang, and J. Chai, Entropy 26 (2024).
- [78] L. H. Delgado-Granados, L. M. Sager-Smith, K. Trifonova, and D. A. Mazziotti, The Journal of Physical Chemistry Letters 16, 2231 (2025).
- [79] S. Hazra, U. Patil, and S. Sanvito, Journal of Chemical Theory and Computation 20, 4569–4578 (2024).
- [80] X. Gong, H. Li, N. Zou, R. Xu, W. Duan, and Y. Xu, Nature Communications 14, 10.1038/s41467-023-38468-8 (2023).
- [81] M. B. Hastings and T. Koma, Communications in Mathematical Physics 265, 781–804 (2006).
- [82] T. Nishijima, Universal approximation theorem for neural networks (2021), arXiv:2102.10993 [cs.LG].
- [83] Z. Xu, Y. Zhang, and M. Raginsky, arXiv preprint arXiv:2106.03947 (2021).
- [84] N. Rahaman, A. Baratin, D. Arpit, F. Draxler, M. Lin, F. Hamprecht, Y. Bengio, and A. Courville, arXiv preprint arXiv:1806.08734 (2019).
- [85] J. Kim, J. K. Lee, and K. M. Lee, in Proceedings of the IEEE Conference on Computer Vision and Pattern Recognition (CVPR) (2016) pp. 1646–1654.
- [86] I. Goodfellow, Y. Bengio, and A. Courville, Deep Learning (MIT Press, 2016) http://www.deeplearningbook. org.
- [87] Y. LeCun, L. Bottou, G. B. Orr, and K.-R. Müller, in Neural Networks: Tricks of the Trade, Lecture Notes in Computer Science, Vol. 1524, edited by G. B. Orr and K.-R. Müller (Springer, Berlin, Heidelberg, 1998) pp. 9-50
- [88] O. Press, N. A. Smith, and M. Lewis, Train short, test long: Attention with linear biases enables input length extrapolation (2022), arXiv:2108.12409 [cs.CL].
- [89] K. M. Nakanishi, Scalable-softmax is superior for attention (2025), arXiv:2501.19399 [cs.CL].
- [90] N. Srivastava, G. Hinton, A. Krizhevsky, I. Sutskever, and R. Salakhutdinov, Journal of Machine Learning Re-

- search 15, 1929 (2014).
- [91] D. Hendrycks and K. Gimpel, Gaussian error linear units (gelus) (2023), arXiv:1606.08415 [cs.LG].
- [92] M. Lee, Gelu activation function in deep learning: A comprehensive mathematical analysis and performance (2023), arXiv:2305.12073 [cs.LG].
- [93] R. W. Richardson, Physics Letters 3, 277 (1963).
- [94] R. W. Richardson and N. Sherman, Nuclear Physics 52, 221 (1964).
- [95] J. Dukelsky, S. Pittel, and G. Sierra, Rev. Mod. Phys. 76, 643 (2004).
- [96] C. L. Kane and E. J. Mele, Phys. Rev. Lett. 95, 146802 (2005).
- [97] J. Hubbard, Proceedings of the Royal Society of London Series A 276, 238 (1963).
- [98] J. Hubbard, Proceedings of the Royal Society of London Series A 277, 237 (1964).
- [99] J. E. Hirsch and S. Tang, Phys. Rev. Lett. 62, 591 (1989).
- [100] A. Vaswani, N. Shazeer, N. Parmar, J. Uszkoreit, L. Jones, A. N. Gomez, L. u. Kaiser, and I. Polosukhin, in Advances in Neural Information Processing Systems, Vol. 30, edited by I. Guyon, U. V. Luxburg, S. Bengio, H. Wallach, R. Fergus, S. Vishwanathan, and R. Garnett (Curran Associates, Inc., 2017).
- [101] D. Bahdanau, K. Cho, and Y. Bengio, Neural machine translation by jointly learning to align and translate (2016), arXiv:1409.0473 [cs.CL].
- [102] P. Shaw, J. Uszkoreit, and A. Vaswani, Selfattention with relative position representations (2018), arXiv:1803.02155 [cs.CL].
- [103] B. Mildenhall, P. P. Srinivasan, M. Tancik, J. T. Barron, R. Ramamoorthi, and R. Ng, in Computer Vision ECCV 2020: 16th European Conference, Glasgow, UK, August 23–28, 2020, Proceedings, Part I (Springer-Verlag, Berlin, Heidelberg, 2020) p. 405–421.
- [104] V. Sitzmann, J. N. P. Martel, A. W. Bergman, D. B. Lindell, and G. Wetzstein, Implicit neural representations with periodic activation functions (2020), arXiv:2006.09661 [cs.CV].
- [105] I. Loshchilov and F. Hutter, Decoupled weight decay regularization (2019), arXiv:1711.05101 [cs.LG].
- [106] C. E. Rasmussen and C. K. I. Williams, Gaussian Processes for Machine Learning (MIT Press, Cambridge, MA, 2006).
- [107] T. Gneiting, Journal of Multivariate Analysis 83, 493 (2002).
- [108] M. D. Buhmann, Radial Basis Functions: Theory and Implementations, Cambridge Monographs on Applied and Computational Mathematics, Vol. 12 (Cambridge University Press, Cambridge, 2003).
- [109] S. Li, C. You, G. Guruganesh, J. Ainslie, S. Ontanon, M. Zaheer, S. Sanghai, Y. Yang, S. Kumar, and S. Bhojanapalli, arXiv preprint arXiv:2310.04418 (2023).
- [110] Y. Zhou, U. Alon, X. Chen, X. Wang, R. Agarwal, and D. Zhou, Transformers can achieve length generalization but not robustly (2024), arXiv:2402.09371 [cs.LG].
- [111] J. S. Bridle, in NATO Neurocomputing (1989).
- [112] R. G. Keys, IEEE Transactions on Acoustics, Speech, and Signal Processing 29, 1153 (1981).
- [113] D. P. Mitchell and A. N. Netravali, in Proceedings of the 15th Annual Conference on Computer Graphics and Interactive Techniques (SIGGRAPH '88) (ACM, Atlanta, Georgia, USA, 1988) pp. 221–228.

- [114] D. P. Kingma and J. Ba, Adam: A method for stochastic optimization (2017), arXiv:1412.6980 [cs.LG].
- [115] J. Bardeen, L. N. Cooper, and J. R. Schrieffer, Phys. Rev. 108, 1175 (1957).
- [116] A. Faribault, P. Calabrese, and J.-S. Caux, Phys. Rev. B 77, 064503 (2008).
- [117] P. W. Claeys, S. De Baerdemacker, M. Van Raemdonck, and D. Van Neck, Phys. Rev. B 91, 155102 (2015).
- [118] X. Guan, K. D. Launey, M. Xie, L. Bao, F. Pan, and J. P. Draayer, Phys. Rev. C 86, 024313 (2012).
- [119] J. Bergstra, D. Yamins, and D. Cox, in *Proceedings of the 30th International Conference on Machine Learning*, Proceedings of Machine Learning Research, Vol. 28, edited by S. Dasgupta and D. McAllester (PMLR, Atlanta, Georgia, USA, 2013) pp. 115–123.
- [120] S. Li, C. You, G. Guruganesh, J. Ainslie, S. Ontanon, M. Zaheer, S. Sanghai, Y. Yang, S. Kumar, and S. Bhojanapalli, Functional interpolation for relative positions improves long context transformers (2024), arXiv:2310.04418 [cs.LG].
- [121] K. He, X. Zhang, S. Ren, and J. Sun, in 2015 IEEE International Conference on Computer Vision (ICCV) (2015) pp. 1026–1034.
- [122] X. Glorot and Y. Bengio, in Proceedings of the Thirteenth International Conference on Artificial Intelligence and Statistics, Proceedings of Machine Learning Research, Vol. 9, edited by Y. W. Teh and M. Titterington (PMLR, Chia Laguna Resort, Sardinia, Italy, 2010) pp. 249–256.
- [123] I. Loshchilov and F. Hutter, in *International Conference* on Learning Representations (2017).

# CONTENTS

I.	Introduction	1
II.	Interpolability of $n$ -RDM	2
III.	NN Architectures A. Self-Attention NN B. SIREN C. Beyond 1-RDM	3 3 4 5
IV.	Pair-Pair Correlation Functions	5
V.	Translationally-Invariant HF	5
VI.	HF Allowing Translational Breaking	7
VII.	Conclusion and Discussion	7
III.	Acknowledgments	8
	References	8
	NN Architecture  1. Self-Attention NN Architecture for the 1-RDM a. physical set-up b. Preprocessing (transform 1-RDM to NN input) c. Overall Structure of Attention Layers d. Attention Block (multiple attention heads) e. Dropout, Layer Normalization, and FFN  2. SIREN with Custom Loss Function a. physical set-up b. NN input c. SIREN architecture d. Datasets, standardization, and evaluation grids e. Loss function  Richardson Model  1. Model Formulation a. Analytic Solution via the Richardson Equations b. Pair-Pair Correlators: Gaudin Matrix and Exact Formula c. Complex Rapidities, Conjugation Pairing, and Reality of Energy and Correlators d. Numerical Exact Pair-Pair Correlator Data e. Exact-Diagonalization (ED) Validation  2. ML Results	12 12 12 12 13 15 16 17 17 18 18 18 19 20 20 25 28 29 32
C.	Translation-invariant 1-RDM in a four-band model  1. Model Set-Up  2. ML Results     a. Hyperparameters     b. Standardization     c. Weight Initialization     d. Results	34 34 37 37 37 38 38
D.	Square-lattice Hubbard model  1. Model Set-Up  2. ML Results a. Self-Attention NN b. SIREN	39 39 41 41 42

c. Results 42

#### Appendix A: NN Architecture

We train NNs on n-RDMs computed on small  $L \times L$  lattices and use them to predict n-RDMs for larger systems, exploiting their smooth, periodic structure over the BZ. We use two complementary architectures: (i) a self-attention NN that treats momenta as tokens and learns n-RDMs via self-attention [58, 100–102], and (ii) an implicit neural representation (INR) in the style of NeRF/SIREN that models n-RDMs as a continuous periodic function evaluable at arbitrary system sizes [103, 104].

#### 1. Self-Attention NN Architecture for the 1-RDM

We start with the self-attention NN for 1-RDM.

a. physical set-up

The self-attention NN is applied on a 1-RDM in two spatial dimensions (2D) for the examples in Sec. C and Sec. D. Therefore, in this part, we will first discuss 1-RDM that will be fed into the NN. The 1-RDM has the general form

$$O_{\mathbf{k}\alpha,\mathbf{k}'\alpha'} = \langle c_{\mathbf{k}\alpha}^{\dagger} c_{\mathbf{k}'\alpha'} \rangle \tag{A1}$$

where k and k' ranges over the first BZ,  $\alpha$  represents intra-unit-cell degrees of freedom (sublattice, orbital, spin, etc.), taking  $\xi$  different values of them per k.  $c_{k\alpha}^{\dagger}$  is the creation operator for a state with Bloch momentum k and index  $\alpha$ , and  $\langle ... \rangle$  is the ground state average. k takes  $L \times L$  different values:

$$\mathbf{k} = (l_1/L)\mathbf{b}_1 + (l_2/L)\mathbf{b}_2 , \qquad (A2)$$

where  $l_1, l_2 = 0, 1, 2, ..., L - 1$ , and  $\boldsymbol{b}_1$  and  $\boldsymbol{b}_2$  are two primitive reciprocal lattice vectors. When the translation symmetry is not spontaneously broken, the 1-RDM is reduced to

$$O_{\mathbf{k},\alpha\alpha'} = \langle c_{\mathbf{k}\alpha}^{\dagger} c_{\mathbf{k}\alpha'} \rangle, \quad O_{\mathbf{k}} \in \mathbb{C}^{\xi \times \xi},$$
 (A3)

so the tensor has shape  $L \times L \times \xi \times \xi$ . This is the case for Sec. C. When the translation symmetry is spontaneously broken, we will look at  $O_{\mathbf{k}\alpha,\mathbf{k}'\alpha'}$  with fixed  $\mathbf{q} \equiv \mathbf{k}' - \mathbf{k}$ , *i.e.*,

$$O_{\mathbf{k},\alpha\alpha'}^{\mathbf{q}} = O_{\mathbf{k}\alpha,\mathbf{k}+\mathbf{q}\alpha'} . \tag{A4}$$

For a fixed q,  $O^q$  is also a tensor of dimension  $L \times L \times \xi \times \xi$ . In the notation of  $O^q_{k,\alpha\alpha'}$ , the translational invariant case is just to focus on  $O^{q=0}_{k,\alpha\alpha'}$ . Therefore, regardless of the translation symmetry,  $O^q_{k,\alpha\alpha'}$  has dimension  $L \times L \times \xi \times \xi$ .

b. Preprocessing (transform 1-RDM to NN input)

With the 1-RDM  $O^q$  defined above, we now show how they are transformed into fixed-length vectors and standardized to form the input for our self-attention NN, which is preprocessing part of Fig. 2(a). From Eq. (A2), the BZ grid has  $L \times L$  momenta with the *i*th momentum labelled as  $k_i$  ( $i = 1, 2, ..., L^2$ ).

For each  $k_i$ , we consider the corresponding 1-RDM block,  $O^q(k_i)$ . We transform (flatten) this matrix into a real vector  $x(k_i) \in \mathbb{R}^{2\xi^2}$  in the following way. For the translation-invariant case,  $O^q(k_i) \in \mathbb{C}^{\xi \times \xi}$  and q = 0 (Sec. C),

$$\boldsymbol{x}(\boldsymbol{k}_i) \equiv \begin{bmatrix} vec(\operatorname{Re} O^{\boldsymbol{q}}(\boldsymbol{k}_i)) \\ vec(\operatorname{Im} O^{\boldsymbol{q}}(\boldsymbol{k}_i)) \end{bmatrix} \in \mathbb{R}^{2\xi^2}.$$
 (A5)

Here the operation vec(...) simply turns a matrix into a long column vector by transposing and then stacking its rows from top to bottom. Namely,

$$[vec(M)]_{(\alpha-1)\xi+\alpha'} \equiv M_{\alpha\alpha'}, \qquad \alpha, \alpha' = 1, \dots, \xi.$$
 (A6)

For the specific translational-symmetry-breaking case in Hubbard model discussed in Sec. D, we have  $O^{q}(\mathbf{k}_{i})$  real. Furthermore,  $\mathbf{q}$  only takes two values ,  $\mathbf{q} \in \{0, \mathbf{Q}\}$  with  $\mathbf{Q} = (\pi, \pi)$ . Thus, in this case, we do not split the 1-RDM into real/imaginary parts; instead we stack the two q-blocks:

$$\boldsymbol{x}(\boldsymbol{k}_i) \equiv \begin{bmatrix} vec(O^0(\boldsymbol{k}_i)) \\ vec(O^{\boldsymbol{Q}}(\boldsymbol{k}_i)) \end{bmatrix} \in \mathbb{R}^{2\xi^2}.$$
 (A7)

Therefore, both cases (Eqs. (A5) and (A7)) leads to  $\boldsymbol{x}(\boldsymbol{k}_i)$  with the same shape, thus the components of  $\boldsymbol{x}(\boldsymbol{k}_i)$  can be labeled by  $f \in \{1, \dots, 2\xi^2\}$ . See Sec. C and Sec. D for more details about the preprocessing steps for each model. For one BZ mesh, stack the  $L^2$  vectors  $\boldsymbol{x}(\boldsymbol{k}_i)$  row-wise to form

$$X \equiv \begin{bmatrix} \boldsymbol{x}(\boldsymbol{k}_1)^{\top} \\ \vdots \\ \boldsymbol{x}(\boldsymbol{k}_{L^2})^{\top} \end{bmatrix} \in \mathbb{R}^{L^2 \times 2\xi^2}.$$
 (A8)

A single training sample consists of two 1-RDMs over the entire BZ, an initial  $O_{\text{init}}^q$  and a final (target)  $O_{\text{tgt}}^q$ . Here, "init" means the 1-RDM we used to start HF; "tgt" means the true final 1-RDM we obtained at zero temperature after self-consistent HF convergence. After flattening in Eqs. (A5) and (A7), they become:

$$X^{(\beta)} \equiv \begin{bmatrix} \boldsymbol{x}^{(\beta)}(\boldsymbol{k}_1)^{\top} \\ \vdots \\ \boldsymbol{x}^{(\beta)}(\boldsymbol{k}_{L^2})^{\top} \end{bmatrix} \in \mathbb{R}^{L^2 \times 2\xi^2}, \qquad \beta \in \{\text{init}, \text{tgt}\}.$$
(A9)

Define means and standard deviations over all  $k_i$  and all  $N_{\text{sample}}$  training samples with  $\beta \in \{\text{init}, \text{tgt}\}$ , for each feature  $f \in \{1, \dots, 2\xi^2\}$ :

$$\mu_f^{(\beta)} \equiv \frac{1}{N_{\text{sample}} L^2} \sum_{\text{sample}} \sum_{i=1}^{L^2} X_{i,f}^{(\beta)}, \qquad \left(\sigma_f^{(\beta)}\right)^2 \equiv \frac{1}{N_{\text{sample}} L^2 - 1} \sum_{\text{sample}} \sum_{i=1}^{L^2} \left(X_{i,f}^{(\beta)} - \mu_f^{(\beta)}\right)^2. \tag{A10}$$

Note that for the translation-invariant case (Sec. C), we calculate the mean and standard deviation across all features (see Eq. (C24)). We then standardize  $X_{\text{init}}$ ,  $X_{\text{tgt}}$  (computing the z-score):

$$\widetilde{X}_{i,f}^{(\text{init})} \equiv \frac{X_{i,f}^{(\text{init})} - \mu_f^{(\text{init})}}{\sigma_f^{(\text{init})}}, \qquad \widetilde{X}_{i,f}^{(\text{tgt})} \equiv \frac{X_{i,f}^{(\text{tgt})} - \mu_f^{(\text{tgt})}}{\sigma_f^{(\text{tgt})}}, \tag{A11}$$

Equivalently, for each  $k_i$ 

$$\tilde{\boldsymbol{x}}^{(\beta)}(\boldsymbol{k}_i) \equiv \left(\tilde{X}_{i,1}^{(\beta)}, \dots, \tilde{X}_{i,2\xi^2}^{(\beta)}\right)^{\top} \in \mathbb{R}^{2\xi^2}.$$
(A12)

In what follows, the NN input is the standardized  $\tilde{x}^{(\text{init})}(k_i)$ ; for brevity we write  $\tilde{x}_i \equiv \tilde{x}^{(\text{init})}(k_i)$  unless stated otherwise. Standardization ensures that both the input and output data in the training dataset have a mean of 0 and a standard deviation of 1, which improves numerical conditioning and speeds training [86, 87]. This combined set of transformations (flattening in Eq. (A5) and standardization in Eq. (A11)) is denoted in the preprocessing part of Fig. 2. Note that since these transformations are invertible, we can easily reverse the process to recover the predicted final 1-RDMs from the NN outputs. The matrices  $\tilde{X}^{(\text{init})}$  and  $\tilde{X}^{(\text{tgt})}$ , containing exactly the information from  $O_{\text{init}}^q$  and  $O_{\text{tgt}}^q$ , are thus the data we use to train the NN. During the training process, the self-attention NN parameters are optimized so that, starting from  $O_{\text{init}}^q$  defined on all  $L^2$  momenta, it produces  $O_{\text{out}}^q$  whose values at each  $k_i$  closely matches the  $O_{\text{tgt}}^q$ . After the training, we would expect the NN to be able to make accurate predictions for  $O_{\text{tgt}}^q$  not only for the training system size but also for larger L.

### c. Overall Structure of Attention Layers

With each local  $O^{q}(\mathbf{k}_{i})$  now flattened and standardized (Eq. (A5)-Eq. (A7)) into token features  $\tilde{\mathbf{x}}_{i}$ , we now describe the overall structure of how our model processes them through stacked attention layers to produce the predicted final 1-RDM, as shown in Fig. 2(b).

Input layer. As shown in Eqs. (A5) and (A7), at each momentum  $k_i$  we have a normalized real feature vector  $\tilde{x}_i \in \mathbb{R}^{2\xi^2}$  (flattened entries of the 1-RDM at some  $k_i$ ). We first map it to a vector of dimension D (where D is the "model width"):

$$\boldsymbol{h}_i^{(0)} = W_{\text{in}} \tilde{\boldsymbol{x}}_i + \boldsymbol{b}_{\text{in}} \in \mathbb{R}^D, \tag{A13}$$

where  $W_{\rm in}, \boldsymbol{b}_{\rm in}$  are learnable parameters. Stacking all  $\boldsymbol{h}_i^{(0)}$  gives us a matrix  $H^{(0)}$ ,

$$H^{(0)} = \begin{bmatrix} (\boldsymbol{h}_1^{(0)})^\top \\ \vdots \\ (\boldsymbol{h}_{L^2}^{(0)})^\top \end{bmatrix} \in \mathbb{R}^{L^2 \times D}. \tag{A14}$$

Attention layers. We then apply N attention layers (Fig. 2(a)) to  $H^{(0)}$  in sequence in order to produce  $H^{(N)} \in \mathbb{R}^{L^2 \times D}$ , where the i-th row is  $h_i^{(N)} \in \mathbb{R}^D$ . In general, we denote the matrix  $H^{(\ell-1)} \in \mathbb{R}^{L^2 \times D}$  as the input to the  $\ell^{\text{th}}$  layer of our model,  $\ell \in \{1, \dots N\}$ . The structure of one attention layer consists of three components: (a) one attention block discussed in Sec. A 1 d, (b) Dropout and LayerNorm discussed in Sec. A 1 e and (c) one FFN, also discussed in Sec. A 1 e. As we will see in Sec. A 1 e, the first FFN layer (see construction in Sec. A 1 e) maps  $\mathbb{R}^D \to \mathbb{R}^{D_{\text{ff}}}$  and the second maps back  $\mathbb{R}^{D_{\text{ff}}} \to \mathbb{R}^D$ .

Output head. Finally, we define a linear head with which learnable parameters  $W_{\text{out}} \in \mathbb{R}^{2\xi^2 \times D}$ ,  $\boldsymbol{b}_{\text{out}} \in \mathbb{R}^{2\xi^2}$  that maps each  $\boldsymbol{h}_i$  back to a vector  $\hat{\boldsymbol{x}}_i$ :

$$\widehat{\boldsymbol{x}}_i = W_{\text{out}} \, \boldsymbol{h}_i^{(N)} + \boldsymbol{b}_{\text{out}} \, . \tag{A15}$$

Stacking all  $\hat{x}_i$  gives

$$\widetilde{X}_{\text{out}} = \begin{bmatrix} \widehat{\boldsymbol{x}}_{1}^{\top} \\ \vdots \\ \widehat{\boldsymbol{x}}_{L^{2}}^{\top} \end{bmatrix} \in \mathbb{R}^{L^{2} \times 2\xi^{2}}.$$
(A16)

To recover the physics of 1-RDM, we de-standardize elementwise (reverse of Eq. (A11)):

$$(X_{\text{out}})_{i,f} \equiv (\widetilde{X}_{\text{out}})_{i,f} \sigma_f^{\text{tgt}} + \mu_f^{\text{tgt}}.$$
 (A17)

Note that when testing the trained NN for larger L, we use the same  $\mu_f^{\rm tgt}$  and  $\sigma_f^{\rm tgt}$  computed from the smaller system size, since the assumption is that they possess similar distributions. We then reshape  $X_{\rm out}$  to  $L \times L \times \xi \times \xi$  and recombine the real/imag halves to invert the flattening in Eq. (A5) - Eq. (A7), yielding the final predicted 1-RDM:

$$\boldsymbol{x}_{\mathrm{out}}(\boldsymbol{k}_i) \equiv \left(\widetilde{\boldsymbol{x}}_{\mathrm{out}}(\boldsymbol{k}_i)\right)_f \sigma_f^{\mathrm{tgt}} + \mu_f^{\mathrm{tgt}}, \qquad f = 1, \dots, 2\xi^2.$$
 (A18)

$$\operatorname{Re} O_{\operatorname{out}}^{q}(\boldsymbol{k}_{i}) \equiv \operatorname{vec}^{-1}\left(\left(\boldsymbol{x}_{\operatorname{out}}(\boldsymbol{k}_{i})\right)_{1:\xi^{2}}\right), \qquad \operatorname{Im} O_{\operatorname{out}}^{q}(\boldsymbol{k}_{i}) \equiv \operatorname{vec}^{-1}\left(\left(\boldsymbol{x}_{\operatorname{out}}(\boldsymbol{k}_{i})\right)_{\xi^{2}+1:2\xi^{2}}\right), \tag{A19}$$

$$O_{\text{out}}^{q}(\mathbf{k}_{i}) = \operatorname{Re} O_{\text{out}}^{q}(\mathbf{k}_{i}) + i \operatorname{Im} O_{\text{out}}^{q}(\mathbf{k}_{i}), \tag{A20}$$

where  $\mu_f$ ,  $\sigma_f$  are defined in Eq. (A10). And  $\text{vec}^{-1}$  is the inverse of the vec in Eq. (A5), which takes a length- $\xi^2$  vector and reshapes it back into a  $\xi \times \xi$  matrix using the same stacking convention from vec (see Eq. (A5)). The process from Eq. (A17) to Eq. (A20) are shown as the decoding step in Fig. 2.

**Training.** For computational efficiency, we divide the training dataset into several "minibatches" (according to standard practice), where each minibatch consists of  $N_b$  ( $\widetilde{X}_{\rm init}$ ,  $\widetilde{X}_{\rm tgt}$ ) pairs. For our loss function, we use the MSE between  $\widetilde{X}_{\rm out}$  and  $\widetilde{X}_{\rm tgt}$  (both of which have a total of  $L^2$  elements):

$$\mathcal{L} = \frac{1}{N_b L^2 (2\xi^2)} \sum_{b=1}^{N_b} \sum_{i=1}^{L^2} \sum_{f=1}^{2\xi^2} \left( \widetilde{X}_{\text{out},i,f}^{(b)} - \widetilde{X}_{\text{tgt},i,f}^{(b)} \right)^2.$$
(A21)

as indicated in Fig. 2, then take the gradient of the loss  $\mathcal{L}$  with respect to the trainable parameters (defined in Sec. A 1 e) and update the values of parameters using the AdamW optimizer [105].

#### d. Attention Block (multiple attention heads)

Here we describe the detailed structure of the attention block we first mentioned in Sec. A 1 c as part of each attention layer. Each attention block includes  $N_{\text{head}}$  attention heads (Fig. 2(c)). The structure of one attention head is shown in Fig. 2(d). We first introduce the *Bias* block in Fig. 2(d). The bias block is constructed based on the geometry-aware relative positional bias that will be used in attention heads. Intuitively speaking, attention [100] decides "which  $\mathbf{k}_j$  should influence  $\mathbf{k}_i$ ." We want this decision to respect BZ geometry and periodicity. Precisely, for each ordered pair of momenta  $(\mathbf{k}_i, \mathbf{k}_j)$  with  $\mathbf{k}_i = \frac{l_{i,1}}{L} \mathbf{b}_1 + \frac{l_{i,2}}{L} \mathbf{b}_2$  and  $\mathbf{k}_j = \frac{l_{j,1}}{L} \mathbf{b}_1 + \frac{l_{j,2}}{L} \mathbf{b}_2$  defined in Eq. (A2), we stack them to form the vector

$$\left(\frac{l_{i,1}}{L}, \frac{l_{i,2}}{L}, \frac{l_{j,1}}{L}, \frac{l_{j,2}}{L}\right) \in [0,1)^4.$$
 (A22)

In each attention head, we then define a learnable continuous function  $f_{\theta}: \mathbb{R}^4 \to \mathbb{R}$  that maps each such pair of momenta to a scalar bias that represents how closely correlated they are. In general, this  $f_{\theta}$  can be parameterized as a standard NN, as in Sec. C. However, we can also explicitly incorporate our physical assumptions by using a carefully-chosen ansatz with a periodic basis, as is used in Sec. D and described below. Let  $W_r \in \mathbb{R}^{m \times 2}$  be a learnable matrix, where m is a hyperparameter that determines the number of frequencies. Project each  $k_i, k_j$ , separately:

$$\boldsymbol{u}_{i} = W_{r} \begin{bmatrix} l_{i,1} \\ \overline{L} \\ l_{i,2} \\ \overline{L} \end{bmatrix} \in \mathbb{R}^{m}, \qquad \boldsymbol{u}_{j} = W_{r} \begin{bmatrix} l_{j,1} \\ \overline{L} \\ \underline{l_{j,2}} \\ \overline{L} \end{bmatrix} \in \mathbb{R}^{m}.$$
(A23)

We build periodic features

$$\phi(\mathbf{k}) \equiv \cos \mathbf{u} + \sin \mathbf{u} \in \mathbb{R}^m$$
 (applied elementwise), (A24)

and take the difference

$$\Delta_{ij} = \phi(\mathbf{k}_i) - \phi(\mathbf{k}_j) \in \mathbb{R}^m. \tag{A25}$$

With a learnable vector of coefficients  $C \in \mathbb{R}^m$  (which is initially set to all 1's before being optimized during training), we define a scalar, nonnegative "periodic distance"  $\sigma_{ij}$ ,

$$\sigma_{ij} \equiv \left| \langle \mathbf{\Delta}_{ij}, \mathbf{C} \rangle \right| \ge 0, \tag{A26}$$

(here <, > means standard dot-product) and convert it to a decaying bias [102]  $f_{\theta}$ :

$$f_{\theta}(\mathbf{k}_i, \mathbf{k}_j) \equiv \exp\left[-\left(\sigma_{ij} + \varepsilon\right)^p\right], \qquad \varepsilon = 10^{-6},$$
 (A27)

where  $p \in [0.5, 3]$  is an exponent that serves as a practical stability constraint [106–108]. Repeating this process for each pair of momenta, we obtain a matrix  $B \in \mathbb{R}^{L^2 \times L^2}$ , where we define

$$B_{ij} \equiv f_{\theta}(\mathbf{k}_i, \mathbf{k}_j), \quad i, j \in \{1, \dots L^2\}. \tag{A28}$$

Thus  $B_{ij}$  acts as a smooth, periodic bias on the 1BZ [109, 110], which is shown as the Bias block in Fig. 2(d).

Besides the bias block, the attention head also involves the query Q matrix, key K matrix, value V matrix, and Scalable Softmax. For each attention head  $h \in \{1, \ldots, N_{\text{head}}\}$  with  $N_{\text{head}}$  the number of heads, we make matrices  $Q^{(h)}, K^{(h)}, V^{(h)} \in \mathbb{R}^{L^2 \times d_k}$  [100] by multiplying  $H^{(\ell-1)}$  (the current layer's input) with learnable matrices  $W_Q^{(h)}, W_K^{(h)}, W_V^{(h)} \in \mathbb{R}^{D \times d_k}$ , where  $d_k \equiv D/N_{\text{head}}$  is the width of each head and D is the model width as defined in Sec. A 1 c. Then we have:

$$Q^{(h)} = H^{(\ell-1)} W_Q^{(h)}, \qquad K^{(h)} = H^{(\ell-1)} W_K^{(h)}, \qquad V^{(h)} = H^{(\ell-1)} W_V^{(h)}. \tag{A29}$$

With  $B_{ij}$  from Eq. (A28), define the pre-softmax logits [58, 88] as:

$$\Lambda_{ij}^{(h)} = \tau \left( \frac{\langle Q_i^{(h)}, K_j^{(h)} \rangle + B_{ij}}{\sqrt{d_k}} \right), \quad \text{where } \tau \equiv s \log \left( L^2 \right) ,$$
(A30)

and s is a learnable parameter. (We use the notation of  $Q_i, K_i$ , and  $V_i$  for the  $i^{\text{th}}$  row of Q, K, and V, respectively, with  $i \in \{1, \dots L^2\}$ ). Notice that  $B_{ij} \in (0,1]$  is large when  $k_i$  and  $k_j$  are close on 1BZ, so it adds extra preference

to mix nearby momenta. Meanwhile, the multiplication by  $s \log (L^2)$  implements Scalable Softmax [89] to avoid the phenomenon of "attention fading"; that is, it ensures that for a large number of k-points [88], the maximum value of the attention weights does not drop to 0, which could otherwise hinder the NN's capacity for length generalization. The attention weights and head outputs are

$$A_{ij}^{(h)} = \frac{e^{\tau \Lambda_{ij}^{(h)}}}{\sum_{m=1}^{L^2} e^{\tau \Lambda_{im}^{(h)}}}, \qquad \sum_{j} A_{ij}^{(h)} = 1, \quad A_{ij}^{(h)} > 0.$$
 (A31)

*i.e.*, Softmax [111] is applied here (row-wise normalization that turns attention scores into positive weights summing to 1). Then,

$$\boldsymbol{z}_{i}^{(h)} = \sum_{j=1}^{L^{2}} A_{ij}^{(h)} V_{j}^{(h)} \in \mathbb{R}^{d_{k}}.$$
(A32)

We can stack all the  $z_i$ 's constructed in this way to form a matrix:

$$Z^{(h)} = \begin{bmatrix} \boldsymbol{z}_1^{(h)} \\ \vdots \\ \boldsymbol{z}_{L^2}^{(h)} \end{bmatrix} \in \mathbb{R}^{L^2 \times d_k}. \tag{A33}$$

Therefore, a summary of the attention head we just discussed in Eq. (A29)-Eq. (A31) is the following (see the red box in Fig. 2):

$$\begin{cases} Q^{(h)} = H^{(\ell-1)} W_Q^{(h)}, \quad K^{(h)} = H^{(\ell-1)} W_K^{(h)}, \quad V^{(h)} = H^{(\ell-1)} W_V^{(h)}, \\ \Lambda_{ij}^{(h)} = \tau \left( \frac{\left\langle Q_i^{(h)}, K_j^{(h)} \right\rangle + B_{ij}}{\sqrt{d_k}} \right), \text{ where } \tau \equiv s \log \left( L^2 \right), \\ A_{ij}^{(h)} = \frac{e^{\tau \Lambda_{ij}^{(h)}}}{\sum_{L=1}^{L^2} e^{\tau \Lambda_{im}^{(h)}}}, \quad \sum_j A_{ij}^{(h)} = 1, \quad A_{ij}^{(h)} > 0, \\ Z^{(h)} = A^{(h)} V^{(h)}. \end{cases}$$

Finally, the  $N_{\text{head}} \geq 1$  attention heads form an attention block. Parameters are not shared between different attention heads (even if they are in the same attention block), (i.e., each individual attention head has its own set of learnable parameters which are optimized independently from the others). For all  $i \in \{1, \dots L^2\}$ , we concatenate (i.e. "stack") the output vectors  $\mathbf{z}_i^{(h)} \in \mathbb{R}^{d_k}$  from each attention head into a single vector of size  $N_{\text{head}}d_k = D$ :

$$\operatorname{Concat}(Z^{(1)}, \dots, Z^{(N_{\text{head}})}) = \begin{bmatrix} Z^{(1)} & Z^{(2)} & \cdots & Z^{(N_{\text{head}})} \end{bmatrix} \in \mathbb{R}^{L^2 \times D}.$$
(A35)

and then apply an output linear map with learnable parameters  $W_O \in \mathbb{R}^{D \times D}, b_O \in \mathbb{R}^D$ :

$$Z = \operatorname{Concat}\left(Z^{(1)}, \dots, Z^{(N_{\text{head}})}\right) W_O + \mathbf{1}\boldsymbol{b}_O^{\top},\tag{A36}$$

and here 1 is a length- $L^2$  column of ones. This mixes information across heads and returns to the model width D.

e. Dropout, Layer Normalization, and FFN

We now discuss the dropout, layer normalization, and FFN in each each attention layer (we first introduced them in Sec. A1c) as shown in Fig. 2(b).

Applying Dropout to a vector or matrix means that we randomly set each element of the vector or matrix to zero with a probability p or keep it with a probability of 1 - p [90]. We apply dropout to the attention output Z (Eq. (A37)), add the result to the layer input  $H^{(\ell-1)}$  (Eq. (A38)), and then apply LayerNorm per  $k_i$ :

$$\hat{Z} = \text{Dropout}(Z), \quad \text{where } \text{Dropout}(Z)_{ij} = \frac{m_{ij}Z_{ij}}{1-p}, \quad m_{ij} \sim \text{Bernoulli}(1-p),$$
 (A37)

$$U_i = \text{LayerNorm} \left( H_i^{(\ell-1)} + \hat{Z}_i \right), \quad U \in \mathbb{R}^{L^2 \times D}.$$
 (A38)

Here LayerNorm is applied independently to each  $U_i \in \mathbb{R}^D$ , and is defined as follows: define the mean and variance over  $d = 1, \dots, D$ :

$$\mu_i \equiv \frac{1}{D} \sum_{d=1}^{D} U_{i,d}, \qquad \sigma_i^2 \equiv \frac{1}{D} \sum_{d=1}^{D} (U_{i,d} - \mu_i)^2,$$
(A39)

then, with learnable parameters  $\gamma, \beta \in \mathbb{R}^D$  and a small  $\epsilon > 0$ , we set

LayerNorm
$$(U_i) \equiv \gamma \odot \frac{U_i - \mu_i \mathbf{1}}{\sqrt{\sigma_i^2 + \epsilon}} + \beta \in \mathbb{R}^D,$$
 (A40)

where  $\odot$  is the element-wise product. Namely,

$$\left[\text{LayerNorm}(U_i)\right]_d = \gamma_d \frac{U_{i,d} - \mu_i}{\sqrt{\sigma_i^2 + \epsilon}} + \beta_d, \qquad d = 1, \dots, D.$$
(A41)

For every  $\mathbf{k}_i$ , take its current vector  $\mathbf{U}_i \in \mathbb{R}^D$  and apply a learned linear map which increases the dimension to a larger width  $D_{\mathrm{ff}}$ , to get  $\mathbf{F}_i = W_1 \mathbf{U}_i + \mathbf{b}_1$  with  $W_1 \in \mathbb{R}^{D \times D_{\mathrm{ff}}}$  and  $\mathbf{b}_1 \in \mathbb{R}^{D_{\mathrm{ff}}}$ :

$$F = UW_1 + \mathbf{1}\boldsymbol{b}_1^{\top} \in \mathbb{R}^{L^2 \times D_{\text{ff}}}.$$
 (A42)

Apply the GELU ("Gaussian Error Linear Unit" [91]) element-wise to F, which smoothly gates each component of F: small negative values are damped, large positive values pass through almost linearly. It is written using the error function erf, then mapped back from the hidden width to the model width:

$$\widehat{U} = W_2 \operatorname{GELU}(F) + \mathbf{1} \mathbf{b}_2^{\top} \in \mathbb{R}^{L^2 \times D} \quad \text{where} \quad \operatorname{GELU}(F) \equiv \frac{F}{2} \left( \mathbf{1} + \operatorname{erf} \left( \frac{F}{\sqrt{2}} \right) \right), \tag{A43}$$

with  $W_2 \in \mathbb{R}^{D_{\mathrm{ff}} \times D}$ ,  $\boldsymbol{b}_2 \in \mathbb{R}^D$ , and  $\boldsymbol{1} \in \mathbb{R}^{L^2}$  (column of ones). Then,

$$H^{(\ell)} = \text{LayerNorm}\left(\boldsymbol{U} + \text{Dropout}(\widehat{\boldsymbol{U}})\right).$$
 (A44)

Eq. (A43) is labeled as FFN in Fig. 2.

#### 2. SIREN with Custom Loss Function

Alternatively, rather than learning a map from a random initial n-RDM to a final n-RDM, we may treat the task purely as interpolation: we learn a continuous function  $\Phi$  (the interpolant) represented by a NN that takes momentum–space coordinates  $\mathbf{k}$  (or normalized coordinates  $\mathbf{v} \in [-1,1]^2$ , see Eq. (A46)) as input, and outputs a matrix  $O^q(\mathbf{k}_i)$  representing the n-RDM, e.g.  $\Phi(\mathbf{k}) \approx O^q_{\alpha\alpha'}(\mathbf{k})$  (or Re/Im  $O^q_{\alpha\alpha'}(\mathbf{k})$  when training the real/imaginary parts separately). The explicit structure is in Sec. A 2 c. One way to achieve this interpolation is the SIREN architecture. In the following, we will discuss it using the example of fixed- $\mathbf{q}$  1-RDM that only depends on one  $\mathbf{k}$ . Nevertheless, the discussion holds for a matrix that depends on more than one Bloch momenta, as shown in Sec. B.

a. physical set-up

We keep the BZ discretization of Eq. (A2). All n-RDM are defined as in Sec. A1a. As discussed in Sec. A1a, we focus on considering the fixed- $\mathbf{q}$  1-RDMs  $(O_{\mathbf{k},\alpha\alpha'}^{\mathbf{q}})$  over BZ with a shape of  $L \times L \times \xi \times \xi$ . The overall goal of the SIREN [104] approach is to train one continuous function  $\Phi(k_x, k_y)$  that predicts each 1-RDM block over the BZ. In particular, we train a function  $\Phi(k_x, k_y)$  per  $(\alpha, \alpha')$  and per real/imaginary part of  $O_{\mathbf{k},\alpha\alpha'}^{\mathbf{q}}$  if needed, such that

$$\Phi(\mathbf{k}) \approx \operatorname{Re}\left[O_{\mathbf{k},\alpha\alpha'}^{\mathbf{q}}\right] \quad \text{or} \quad \operatorname{Im}\left[O_{\mathbf{k},\alpha\alpha'}^{\mathbf{q}}\right].$$
(A45)

(In practice, both the Hubbard (Sec. D) and the Richardson (Sec. B) model exhibit a vanishing imaginary part, so we only consider the real part for training in those cases.) Stacking all different  $\Phi$  for all different values of  $(\alpha, \alpha')$  reconstructs  $O^q(k)$ . We will train on smaller BZ grids, and then evaluate  $\Phi$  on denser BZ grids.

b. NN input

For an  $L \times L$  BZ with  $\mathbf{k}_i$  from Eq. (A2), we define the normalized coordinate

$$\boldsymbol{v}(\boldsymbol{k}) \equiv \left(2\frac{\ell_1}{L} - 1, 2\frac{\ell_2}{L} - 1\right) \in [-1, 1]^2, \quad \text{for } \boldsymbol{k} = \frac{\ell_1}{L}\boldsymbol{b}_1 + \frac{\ell_2}{L}\boldsymbol{b}_2.$$
(A46)

For each fixed  $(\alpha, \alpha')$ , evaluate  $\text{Re}[O^q(\mathbf{k})]$  and  $\text{Im}[O^q(\mathbf{k})]$  for all  $\mathbf{k}$ . To enforce periodicity at the boundaries, extend each to a wrapped array

$$\operatorname{Re}[\widetilde{O}^{q}], \operatorname{Im}[\widetilde{O}^{q}] \in \mathbb{R}^{(L+1)\times(L+1)}$$
 (A47)

by repeating the first row and column:

$$\tilde{O}_{m,n}^{q} \equiv O_{m \bmod L, n \bmod L}^{q}, \qquad m, n \in \{0, 1, \dots, L\}$$
(A48)

So  $\widetilde{O}^q$  is just  $O^q$  with its first row/column copied to the end—this "closes" the matrix at finite L. For pair-pair correlation functions like in the Richardson model, normalized coordinates can be constructed in an analogous manner, except in that case  $v(k) \in [-1, 1]^4$ . See Sec. B 2 for more details.

#### c. SIREN architecture

Given input to our NN in the form of Eq. (A46), we build one SIREN [104] (depicted in Fig. 3) to predict each block of the 1-RDM respectively (e.g.,  $Re[O(\mathbf{k})]$  or  $Im[O(\mathbf{k})]$ ). Each SIREN has 4 hidden sine layers:  $\mathbf{h}_1, \mathbf{h}_2, \mathbf{h}_3, \mathbf{h}_4$ , followed by a final linear layer. Explicitly,

$$h_{1}(\mathbf{v}) = \sin\left(6\left(W_{1}\mathbf{v} + \mathbf{b}_{1}\right)\right) \in \mathbb{R}^{d_{H}},$$

$$h_{2}(\mathbf{v}) = \sin\left(30\left(W_{2}\mathbf{h}_{1}(\mathbf{v}) + \mathbf{b}_{2}\right)\right) \in \mathbb{R}^{d_{H}},$$

$$h_{3}(\mathbf{v}) = \sin\left(30\left(W_{3}\mathbf{h}_{2}(\mathbf{v}) + \mathbf{b}_{3}\right)\right) \in \mathbb{R}^{d_{H}},$$

$$h_{4}(\mathbf{v}) = \sin\left(30\left(W_{4}\mathbf{h}_{3}(\mathbf{v}) + \mathbf{b}_{4}\right)\right) \in \mathbb{R}^{d_{H}},$$

$$\Phi_{\theta}(\mathbf{v}) = \mathbf{w}^{\top}\mathbf{h}_{4}(\mathbf{v}) + b_{\text{out}} \in \mathbb{R}.$$
(A49)

where

$$\boldsymbol{v} \in \mathbb{R}^2, \quad W_1 \in \mathbb{R}^{d_H \times 2}, W_2, W_3, W_4 \in \mathbb{R}^{d_H \times d_H}, \boldsymbol{b}_1, \boldsymbol{b}_2, \boldsymbol{b}_3, \boldsymbol{b}_4 \in \mathbb{R}^{d_H}, \boldsymbol{w} \in \mathbb{R}^{d_H}, b_{\text{out}} \in \mathbb{R}.$$
 (A50)

Eq. (A49) maps a BZ coordinate from Eq. (A46),  $\mathbf{v} = (v_x, v_y) \in [-1, 1]^2$ , to a scalar  $\Phi_{\theta}(\mathbf{v}) \in \mathbb{R}$  that predicts the corresponding element of either  $\text{Re}[O^q](\mathbf{k}_i)$  or  $\text{Im}[O^q](\mathbf{k}_i)$ . The layer widths are:  $d_0 = 2$  for the input vector  $\mathbf{v}$  (from Eq. (A46)), and  $d_1 = d_2 = d_3 = d_4 = d_H$  for the hidden layers  $(h_{1,2,3,4} \text{ in Eq. (A49)})$  for which we usually select  $d_H \in [256, 800]$ . We choose sines because they naturally model smooth, periodic patterns across the BZ. Additionally, to keep gradients healthy, we incorporate a special weight initialization scheme [104]: define  $W \sim \mathcal{U}(a,b)$  to mean "sample uniformly at random between a and b." Here  $W \sim \mathcal{U}$  denotes element-wise initialization: each entry  $W_{ij}$  is drawn independently from  $\mathcal{U}(a,b)$ . Then we initialize the weights in Eq. (A49) with:

$$W_1 \sim \mathcal{U}\left(-\frac{1}{d_0}, \frac{1}{d_0}\right), \quad \text{and } w^\top, W_\ell \sim \mathcal{U}\left(-\frac{\sqrt{6/d_H}}{30}, \frac{\sqrt{6/d_H}}{30}\right) \text{ elementwise}, \quad 2 \le \ell \le 4.$$
 (A51)

The full model can then be written as  $\Phi_{\theta}$ , where  $\theta$  represents all the tunable parameters mentioned above.

d. Datasets, standardization, and evaluation grids

For  $\text{Re}[\tilde{O}^q] \in \mathbb{R}^{(L+1)\times(L+1)}$  defined in Eq. (A47), we compute the mean and standard deviation over all entries:

$$\mu = \text{mean}(\text{Re}[\tilde{O}^q]), \qquad \sigma = \text{std}(\text{Re}[\tilde{O}^q]),$$
(A52)

and form the standardized version of  $\widetilde{O}^q$  :

$$Z_L \equiv \frac{\operatorname{Re}[\tilde{O}^q] - \mu}{\sigma} \in \mathbb{R}^{(L+1)\times(L+1)}.$$
 (A53)

A similar standardization procedure applies for  $\operatorname{Im}[\tilde{O}^q]$ . For evaluation on larger L, we use the same  $\mu$  and  $\sigma$  (computed from the  $O^q$  used for training) to normalize the data. Also notice that the unstandardized SIREN predictions for the target channel can be recovered after training by reversing Eq. (A53). Each input point is a normalized BZ coordinate  $\nu \in [-1,1]^2$  (see Eq. (A46)). Define the coordinate grid  $X_L \equiv \{v(k_{ij}): i,j=0,\ldots,L\} \subset [-1,1]^{(L+1)\times(L+1)\times2}$ ,  $k_{ij} \equiv \frac{i}{L}b_1 + \frac{j}{L}b_2$ . Our training data thus consists of the set of input coordinates  $X_L \in [-1,1]^{(L+1)\times(L+1)\times2}$  and the normalized values  $Z_L$ .

When calculating the loss, we also evaluate SIREN on a  $L' \times L'$  mesh with L' > L and output  $Z_{L'} \in [-1,1]^{(L'+1)\times(L'+1)\times2}$ , as seen in Sec. A 2 e. However, we will eventually downsample the  $Z_{L'}$  back to  $L \times L$  mesh to compare to the training data. In this process, we do *not* use any true final RDMs on the  $L' \times L'$  mesh as training data, since doing so would defeat our entire purpose of generalizing to larger system sizes.

#### e. Loss function

Define  $\Phi_{\theta}: [-1,1]^2 \to \mathbb{R}$  to be the SIREN we constructed in Sec. A 2 c with tunable parameters denoted as  $\theta$ , which takes a normalized BZ coordinate  $\boldsymbol{v}(\boldsymbol{k}) \in [-1,1]^2$  as input and outputs a scalar prediction for the corresponding element of the chosen 1-RDM block:

$$\widehat{Z}(\mathbf{k}) \equiv \Phi_{\theta}(\mathbf{v}(\mathbf{k})), \tag{A54}$$

For small-mesh MSE,

$$\mathcal{L}_{\text{small}}(\theta) = \frac{1}{(L+1)^2} \sum_{\boldsymbol{v} \in X_L} \left( \widehat{Z}(X_L)[\boldsymbol{v}] - Z_L[\boldsymbol{v}] \right)^2. \tag{A55}$$

Let G be any finite symmetry subgroup of the symmetry group of the system acting on normalized BZ coordinates  $v \in [-1,1]^2$  (e.g., rotations/reflections of the square). Define the symmetrization operator  $S_G$  by averaging over the group action. For example, for a square lattice we take  $G = D_4$  (order 8, consisting of four rotations  $0^{\circ}$ ,  $90^{\circ}$ ,  $180^{\circ}$ ,  $270^{\circ}$  and four reflections across the two axes and two diagonals). Let  $\zeta$  be a fixed downsampler (e.g. bilinear or bicubic interpolation [112, 113]), which is effectively a classical algorithm used to interpolate the SIREN predictions on the denser coordinate mesh  $X_{L'}$  back to the training system size. This allows us to control behavior at finer scales, without the need for additional training data (e.g.  $Z_{L'}$ ) from the larger system. As such, we evaluate the SIREN on the dense grid  $X_{L'}$ , symmetrize, and then downsample back down to  $X_L$ :

$$\widehat{Z}^{\downarrow}(X_L) \equiv \zeta \big( \mathcal{S}_G[\widehat{Z}(X_{L'})] \to X_L \big), \tag{A56}$$

$$\mathcal{L}_{\text{cons}}(\theta) = \frac{1}{(L+1)^2} \sum_{\boldsymbol{v} \in X_L} \left( \widehat{Z}^{\downarrow}(X_L)[\boldsymbol{v}] - Z_L[\boldsymbol{v}] \right)^2.$$
 (A57)

Randomly sample N points  $U = \{u_i\}_{i=1}^N \subset [-1,1]^2$ . With  $\nabla_u$  the gradient and  $\text{Hess}_u$  the Hessian w.r.t. u, and with  $\|\cdot\|_1$  the  $\ell^1$  norm and  $\|\cdot\|_F$  the Frobenius norm:

$$\mathcal{P}_{\text{TV}}(\theta) \equiv \frac{1}{N} \sum_{i=1}^{N} \left\| \nabla_{u} \Phi_{\theta}(u_{i}) \right\|_{1}, \qquad \mathcal{P}_{\text{FH}}(\theta) \equiv \frac{1}{N} \sum_{i=1}^{N} \left\| \text{Hess}_{u} \Phi_{\theta}(u_{i}) \right\|_{F}. \tag{A58}$$

The total loss is:

$$\mathcal{L}(\theta) = \mathcal{L}_{\text{small}}(\theta) + \mathcal{L}_{\text{cons}}(\theta) + \lambda \mathcal{P}(\theta), \qquad \mathcal{P} \in \{\mathcal{P}_{\text{TV}}, \mathcal{P}_{\text{FH}}, 0\}, \tag{A59}$$

with  $\lambda \in [10^{-7}, 10^{-5}]$  in practice. We then take the gradient of  $\mathcal{L}$  w.r.t.  $\theta$  and train the SIREN using the Adam optimizer [114]. For all trainings using a SIREN-based NN in this paper, we set the constant learning rate for the optimizer equal to  $1 \times 10^{-4}$ .

#### Appendix B: Richardson Model

#### 1. Model Formulation

We start by reviewing the Richardson model for superconductivity [93–95].

a. Analytic Solution via the Richardson Equations

We begin with deriving the Richarson model for spinful fermions on a Bravis lattice with one atom per unit cell. We label the hopping by  $t_{rr'}$  and introduce an attraction  $V(r-r') \leq 0$  that depends only on separation r-r' [115]:

$$H = \sum_{\boldsymbol{r},\boldsymbol{r}',s} t_{\boldsymbol{r}\boldsymbol{r}'} c_{\boldsymbol{r}s}^{\dagger} c_{\boldsymbol{r}'s} + \frac{1}{2} \sum_{\boldsymbol{r},\boldsymbol{r}'} V(\boldsymbol{r}-\boldsymbol{r}') c_{\boldsymbol{r}\uparrow}^{\dagger} c_{\boldsymbol{r}'\downarrow}^{\dagger} c_{\boldsymbol{r}'\downarrow} c_{\boldsymbol{r}\uparrow} , \qquad (B1)$$

Introduce lattice Fourier modes

$$c_{\boldsymbol{r},s} = \frac{1}{L} \sum_{\boldsymbol{k} \in \mathbb{R}^{Z}} e^{i\boldsymbol{k} \cdot \boldsymbol{r}} c_{\boldsymbol{k},s}, \qquad c_{\boldsymbol{k},s} = \frac{1}{L} \sum_{\boldsymbol{r}} e^{-i\boldsymbol{k} \cdot \boldsymbol{r}} c_{\boldsymbol{r},s}, \quad \sum_{\boldsymbol{r}} e^{i(\boldsymbol{k} - \boldsymbol{k}') \cdot \boldsymbol{r}} = L^{2} \delta_{\boldsymbol{k},\boldsymbol{k}'}. \tag{B2}$$

so that the kinetic term diagonalizes as

$$H_0 = \sum_{\boldsymbol{r}, \boldsymbol{r}', s} t_{\boldsymbol{r} - \boldsymbol{r}'} c_{\boldsymbol{r}s}^{\dagger} c_{\boldsymbol{r}'s} \tag{B3}$$

$$= \sum_{\boldsymbol{r},\boldsymbol{r'},s} t_{\boldsymbol{r}-\boldsymbol{r'}} \left[ \frac{1}{L} \sum_{\boldsymbol{k}} e^{-i\boldsymbol{k}\cdot\boldsymbol{r}} c_{\boldsymbol{k}s}^{\dagger} \right] \left[ \frac{1}{L} \sum_{\boldsymbol{k'}} e^{i\boldsymbol{k'}\cdot\boldsymbol{r'}} c_{\boldsymbol{k'}s} \right]$$
(B4)

$$= \frac{1}{L^2} \sum_{\mathbf{k}, \mathbf{k}', s} \left[ \sum_{\mathbf{r}, \mathbf{r}'} t_{\mathbf{r} - \mathbf{r}'} e^{-i\mathbf{k} \cdot \mathbf{r}} e^{i\mathbf{k}' \cdot \mathbf{r}'} \right] c_{\mathbf{k}s}^{\dagger} c_{\mathbf{k}'s}$$
(B5)

$$= \frac{1}{L^2} \sum_{\mathbf{k}, \mathbf{k}', s} \left[ \sum_{\mathbf{r} - \mathbf{r}'} t_{\mathbf{r} - \mathbf{r}'} \sum_{\mathbf{r}'} e^{-i\mathbf{k} \cdot (\mathbf{r}' + (\mathbf{r} - \mathbf{r}'))} e^{i\mathbf{k}' \cdot \mathbf{r}'} \right] c_{\mathbf{k}s}^{\dagger} c_{\mathbf{k}'s}$$
(B6)

$$= \frac{1}{L^2} \sum_{\mathbf{k}, \mathbf{k'}, s} \left[ \sum_{\mathbf{r} = \mathbf{r'}} t_{\mathbf{r} - \mathbf{r'}} e^{-i\mathbf{k} \cdot (\mathbf{r} - \mathbf{r'})} \right] \left[ \sum_{\mathbf{r'}} e^{i(\mathbf{k'} - \mathbf{k}) \cdot \mathbf{r'}} \right] c_{\mathbf{k}s}^{\dagger} c_{\mathbf{k'}s}$$
(B7)

$$= \sum_{\mathbf{k},s} \left[ \sum_{\mathbf{r}-\mathbf{r}'} t_{\mathbf{r}-\mathbf{r}'} e^{i\mathbf{k}\cdot(\mathbf{r}-\mathbf{r}')} \right] c_{\mathbf{k}s}^{\dagger} c_{\mathbf{k}s} \qquad \left( \sum_{\mathbf{r}'} e^{i(\mathbf{k}'-\mathbf{k})\cdot\mathbf{r}'} = L^2 \delta_{\mathbf{k},\mathbf{k}'} \right)$$
(B8)

$$= \sum_{\mathbf{k}..s} \varepsilon_{\mathbf{k}} c_{\mathbf{k}s}^{\dagger} c_{\mathbf{k}s}, \tag{B9}$$

where

$$\varepsilon_{\mathbf{k}} = \sum_{\mathbf{r} - \mathbf{r}'} t_{\mathbf{r} - \mathbf{r}'} e^{i\mathbf{k} \cdot (\mathbf{r} - \mathbf{r}')}.$$
 (B10)

The interaction becomes a pair-pair scattering in momentum space,

$$H_{\text{int}} = \frac{1}{2} \sum_{\boldsymbol{r}, \boldsymbol{r}'} V(\boldsymbol{r} - \boldsymbol{r}') c_{\boldsymbol{r}\uparrow}^{\dagger} c_{\boldsymbol{r}'\downarrow}^{\dagger} c_{\boldsymbol{r}'\downarrow} c_{\boldsymbol{r}\uparrow}$$
(B11)

$$= \frac{1}{2} \sum_{\boldsymbol{r}, \boldsymbol{r}'} V(\boldsymbol{r} - \boldsymbol{r}') \left[ \frac{1}{L} \sum_{\boldsymbol{k}} e^{-i\boldsymbol{k}\cdot\boldsymbol{r}} c_{\boldsymbol{k}\uparrow}^{\dagger} \right] \left[ \frac{1}{L} \sum_{\boldsymbol{p}} e^{-i\boldsymbol{p}\cdot\boldsymbol{r}'} c_{\boldsymbol{p}\downarrow}^{\dagger} \right] \left[ \frac{1}{L} \sum_{\boldsymbol{p}'} e^{i\boldsymbol{p}'\cdot\boldsymbol{r}'} c_{\boldsymbol{p}'\downarrow} \right] \left[ \frac{1}{L} \sum_{\boldsymbol{k}'} e^{i\boldsymbol{k}'\cdot\boldsymbol{r}} c_{\boldsymbol{k}'\uparrow} \right]$$
(B12)

$$= \frac{1}{2L^4} \sum_{\mathbf{k}, \mathbf{k'}, \mathbf{p}, \mathbf{p'}} \left[ \sum_{\mathbf{r}, \mathbf{r'}} V(\mathbf{r} - \mathbf{r'}) e^{-i\mathbf{k}\cdot\mathbf{r}} e^{-i\mathbf{p}\cdot\mathbf{r'}} e^{i\mathbf{p'}\cdot\mathbf{r'}} e^{i\mathbf{k'}\cdot\mathbf{r}} \right] c_{\mathbf{k}\uparrow}^{\dagger} c_{\mathbf{p}\downarrow}^{\dagger} c_{\mathbf{p'}\downarrow} c_{\mathbf{k'}\uparrow}$$
(B13)

$$= \frac{1}{2L^4} \sum_{\boldsymbol{k},\boldsymbol{k}',\boldsymbol{p},\boldsymbol{p}'} \left[ \sum_{\boldsymbol{r}-\boldsymbol{r}'} V(\boldsymbol{r}-\boldsymbol{r}') \sum_{\boldsymbol{r}'} e^{-i\boldsymbol{k}\cdot(\boldsymbol{r}'+(\boldsymbol{r}-\boldsymbol{r}'))} e^{-i\boldsymbol{p}\cdot\boldsymbol{r}'} e^{i\boldsymbol{p}'\cdot\boldsymbol{r}'} e^{i\boldsymbol{k}'\cdot(\boldsymbol{r}'+(\boldsymbol{r}-\boldsymbol{r}')))} \right] c_{\boldsymbol{k}\uparrow}^{\dagger} c_{\boldsymbol{p}\downarrow}^{\dagger} c_{\boldsymbol{p}'\downarrow} c_{\boldsymbol{k}'\uparrow}$$
(B14)

$$= \frac{1}{2L^4} \sum_{\mathbf{k}, \mathbf{k}', \mathbf{p}, \mathbf{p}'} \left[ \sum_{\mathbf{r} - \mathbf{r}'} V(\mathbf{r} - \mathbf{r}') \sum_{\mathbf{r}'} e^{i(\mathbf{k}' - \mathbf{k}) \cdot (\mathbf{r} - \mathbf{r}'))} e^{-i\mathbf{k} \cdot \mathbf{r}' + i\mathbf{k}' \cdot \mathbf{r}' - i\mathbf{p} \cdot \mathbf{r}' + i\mathbf{p}' \cdot \mathbf{r}'} \right] c_{\mathbf{k}\uparrow}^{\dagger} c_{\mathbf{p}\downarrow}^{\dagger} c_{\mathbf{p}\downarrow} c_{\mathbf{k}'\uparrow}$$
(B15)

$$= \frac{1}{2L^2} \sum_{\mathbf{k}, \mathbf{k'}, \mathbf{p}, \mathbf{p'}} \left[ \sum_{\mathbf{r} - \mathbf{r'}} V(\mathbf{r} - \mathbf{r'}) e^{i(\mathbf{k'} - \mathbf{k}) \cdot (\mathbf{r} - \mathbf{r'})} \right] \delta_{\mathbf{k} + \mathbf{p}, \ \mathbf{k'} + \mathbf{p'}} c_{\mathbf{k}\uparrow}^{\dagger} c_{\mathbf{p}\downarrow}^{\dagger} c_{\mathbf{p'}\downarrow} c_{\mathbf{k'}\uparrow}$$
(B16)

Define Fourier transform

$$V(q) \equiv \sum_{r=r'} V(r-r')e^{iq\cdot(r-r')}, \qquad (q \equiv k'-k)$$
(B17)

and use p' = k + p - k' from the Kronecker delta to obtain,

$$H_{\text{int}} = \frac{1}{2L^2} \sum_{\mathbf{k}, \mathbf{p}, \mathbf{q}} V(\mathbf{q}) c_{\mathbf{k}\uparrow}^{\dagger} c_{\mathbf{p}\downarrow}^{\dagger} c_{\mathbf{p}-\mathbf{q},\downarrow} c_{\mathbf{k}+\mathbf{q},\uparrow}.$$
(B18)

To obtain the Richardson model from Eq. (B1), we select the subspace of time-reversed pairs with the following constraint in order to get the Richardson model from Eq. (B1):

$$k + p = 0,$$
  $k' + p' = 0 \iff p = -k, p' = -k'.$  (B19)

(Since k and p are the crystal momenta of the two electrons that form a pair, we set their total momentum to be zero.) Equivalently, we restrict to the sector selected by  $\delta_{k+p, 0}$  and  $\delta_{k'+p', 0}$ :

$$H_{\text{int}}^{\text{red}} = \frac{1}{2L^2} \sum_{\mathbf{k}, \mathbf{k}'} V(\mathbf{k}' - \mathbf{k}) c_{\mathbf{k}\uparrow}^{\dagger} c_{-\mathbf{k}\downarrow}^{\dagger} c_{-\mathbf{k}'\downarrow} c_{\mathbf{k}'\uparrow} = \frac{1}{2L^2} \sum_{\mathbf{k}, \mathbf{k}'} V(\mathbf{k}' - \mathbf{k}) A_{\mathbf{k}}^{\dagger} A_{\mathbf{k}'}, \tag{B20}$$

with

$$A_{\mathbf{k}}^{\dagger} \equiv c_{\mathbf{k}\uparrow}^{\dagger} c_{-\mathbf{k}\downarrow}^{\dagger}, \text{ and } A_{\mathbf{k}} \equiv c_{-\mathbf{k}\downarrow} c_{\mathbf{k}\uparrow}.$$
 (B21)

The Richardson model is

$$H = \sum_{\mathbf{k}.s} \varepsilon_{\mathbf{k}} c_{\mathbf{k}s}^{\dagger} c_{\mathbf{k}s} + g \left( \sum_{\mathbf{k}} A_{\mathbf{k}}^{\dagger} \right) \left( \sum_{\mathbf{k}'} A_{\mathbf{k}'} \right), \tag{B22}$$

where  $u=\frac{1}{2}V({\bf k}'-{\bf k})$  and  $g=u/L^2$  with g<0 denoting attractive pairing. Define  $N_{\bf k}\equiv n_{{\bf k}\uparrow}+n_{-{\bf k}\downarrow}=c^{\dagger}_{{\bf k}\uparrow}c_{{\bf k}\uparrow}+c^{\dagger}_{-{\bf k}\downarrow}c_{-{\bf k}\downarrow}$ . The quasi-spin algebra reads

$$[A_{\mathbf{k}}, A_{\mathbf{p}}^{\dagger}] = \delta_{\mathbf{k}\mathbf{p}} (1 - N_{\mathbf{k}}), \quad [N_{\mathbf{k}}, A_{\mathbf{p}}^{\dagger}] = 2\delta_{\mathbf{k}\mathbf{p}} A_{\mathbf{k}}^{\dagger}, \quad [A_{\mathbf{k}}^{\dagger}, A_{\mathbf{p}}^{\dagger}] = 0.$$
 (B23)

In the seniority-zero (all particles paired) sector with M pairs, eigenstates take the factorized form [95],

$$|\Psi_{2M}\rangle = \prod_{\alpha=1}^{M} B_{\alpha}^{\dagger} |0\rangle, \qquad B_{\alpha}^{\dagger} = \sum_{\mathbf{k}} \frac{A_{\mathbf{k}}^{\dagger}}{2\varepsilon_{\mathbf{k}} - E_{\alpha}},$$
 (B24)

where the unknown "rapidities"  $\{E_{\alpha}\}_{\alpha=1}^{M}$  are determined by the eigenequation. Demanding  $H|\Psi_{2M}\rangle=E|\Psi_{2M}\rangle$  and using Eq. (B23) yields the set of coupled equations

$$\frac{1}{g} + \sum_{\mathbf{k}} \frac{1}{2\varepsilon_{\mathbf{k}} - E_{\alpha}} - 2\sum_{\beta(\neq \alpha)} \frac{1}{E_{\beta} - E_{\alpha}} = 0, \quad \alpha = 1, \dots, M$$
(B25)

and the total many-body energy

$$E = \sum_{\alpha=1}^{M} E_{\alpha}.$$
 (B26)

Here, we will derive Eq. (B25) explicitly. Use  $\{c_i, c_j^{\dagger}\} = \delta_{ij}$  and  $\{c_i, c_j\} = \{c_i^{\dagger}, c_j^{\dagger}\} = 0$ , we can show Eq. (B23):

$$[A_{\mathbf{k}}, A_{\mathbf{k}}^{\dagger}] = c_{-\mathbf{k}\downarrow} c_{\mathbf{k}\uparrow} c_{\mathbf{k}\uparrow}^{\dagger} c_{-\mathbf{k}\downarrow}^{\dagger} - c_{\mathbf{k}\uparrow}^{\dagger} c_{-\mathbf{k}\downarrow}^{\dagger} c_{-\mathbf{k}\downarrow} c_{\mathbf{k}\uparrow} = \underbrace{(1 - n_{\mathbf{k}\uparrow})(1 - n_{-\mathbf{k}\downarrow})}_{A_{\mathbf{k}} A_{\mathbf{k}}^{\dagger}} - \underbrace{n_{-\mathbf{k}\downarrow} n_{\mathbf{k}\uparrow}}_{A_{\mathbf{k}}^{\dagger} A_{\mathbf{k}}} = 1 - n_{\mathbf{k}\uparrow} - n_{-\mathbf{k}\downarrow} = 1 - N_{\mathbf{k}} \quad (B27)$$

$$[N_{\mathbf{k}}, A_{\mathbf{p}}^{\dagger}] = \left[n_{\mathbf{k}\uparrow} + n_{-\mathbf{k}\downarrow}, c_{\mathbf{p}\uparrow}^{\dagger} c_{-\mathbf{p}\downarrow}^{\dagger}\right] = \underbrace{[n_{\mathbf{k}\uparrow}, c_{\mathbf{p}\uparrow}^{\dagger}]}_{\delta_{\mathbf{k}\mathbf{p}}c_{\mathbf{p}\uparrow}^{\dagger}} c_{-\mathbf{p}\downarrow}^{\dagger} + c_{\mathbf{p}\uparrow}^{\dagger} \underbrace{[n_{-\mathbf{k}\downarrow}, c_{-\mathbf{p}\downarrow}^{\dagger}]}_{\delta_{\mathbf{k}\mathbf{p}}c_{-\mathbf{p}\downarrow}^{\dagger}} = 2\delta_{\mathbf{k}\mathbf{p}} c_{-\mathbf{p}\downarrow}^{\dagger} = 2\delta_{\mathbf{k}\mathbf{p}} A_{\mathbf{k}}^{\dagger}$$
(B28)

$$[A_{\mathbf{k}}^{\dagger}, A_{\mathbf{p}}^{\dagger}] = c_{\mathbf{k}\uparrow}^{\dagger} c_{-\mathbf{k}\downarrow}^{\dagger} c_{-\mathbf{p}\downarrow}^{\dagger} - c_{\mathbf{p}\uparrow}^{\dagger} c_{-\mathbf{p}\downarrow}^{\dagger} c_{-\mathbf{k}\downarrow}^{\dagger} c_{-\mathbf{k}\downarrow}^{\dagger} = 0$$
(B29)

Note that these are precisely the su(2) quasi-spin relations. We introduce the shorthand for Eq. (B24)

$$\phi_{\alpha}(\mathbf{k}) \equiv \frac{1}{2\varepsilon_{\mathbf{k}} - E_{\alpha}}.$$
 (B30)

Thus  $B_{\alpha}^{\dagger} = \sum_{k} \phi_{\alpha}(k) A_{k}^{\dagger}$ . For later convenience define the collective pair operators

$$A^{\dagger} \equiv \sum_{\mathbf{k}} A_{\mathbf{k}}^{\dagger}, \qquad K_{\alpha} \equiv \sum_{\mathbf{k}} \phi_{\alpha}(\mathbf{k}) \left(1 - N_{\mathbf{k}}\right),$$
 (B31)

i.e.  $K_{\alpha}$  is obtained from  $B_{\alpha}^{\dagger}$  by replacing  $A_{\mathbf{k}}^{\dagger}$  with  $(1-N_{\mathbf{k}})$ . We split the Hamiltonian as

$$H = H_0 + V, \qquad H_0 = \sum_{\mathbf{k},s} \varepsilon_{\mathbf{k}} c_{\mathbf{k}s}^{\dagger} c_{\mathbf{k}s}, \qquad V = g \sum_{\mathbf{k},\mathbf{k}'} A_{\mathbf{k}}^{\dagger} A_{\mathbf{k}'} = g A^{\dagger} A.$$
 (B32)

Evaluate the following commutators using Eq. (B23):

$$[H_0, A_{\mathbf{p}}^{\dagger}] = (\varepsilon_{\mathbf{p}} + \varepsilon_{-\mathbf{p}}) A_{\mathbf{p}}^{\dagger} = 2\varepsilon_{\mathbf{p}} A_{\mathbf{p}}^{\dagger} \quad (\varepsilon_{-\mathbf{p}} = \varepsilon_{\mathbf{p}})$$
(B33)

$$[V, A_{\mathbf{p}}^{\dagger}] = g \sum_{\mathbf{k}, \mathbf{k}'} A_{\mathbf{k}}^{\dagger} [A_{\mathbf{k}'}, A_{\mathbf{p}}^{\dagger}] = g \sum_{\mathbf{k}} A_{\mathbf{k}}^{\dagger} (1 - N_{\mathbf{p}}) = g A^{\dagger} (1 - N_{\mathbf{p}})$$
(B34)

Combined with

$$[H, A_{\mathbf{p}}^{\dagger}] = 2\varepsilon_{\mathbf{p}}A_{\mathbf{p}}^{\dagger} + g A^{\dagger}(1 - N_{\mathbf{p}}). \tag{B35}$$

Using Eq. (B24),

$$[H, B_{\alpha}^{\dagger}] = \sum_{\mathbf{p}} \phi_{\alpha}(\mathbf{p}) [H, A_{\mathbf{p}}^{\dagger}] = \sum_{\mathbf{p}} \phi_{\alpha}(\mathbf{p}) 2\varepsilon_{\mathbf{p}} A_{\mathbf{p}}^{\dagger} + g A^{\dagger} \sum_{\mathbf{p}} \phi_{\alpha}(\mathbf{p}) (1 - N_{\mathbf{p}})$$
(B36)

We have the identity

$$\frac{2\varepsilon_{\mathbf{p}}}{2\varepsilon_{\mathbf{p}} - E_{\alpha}} = \frac{(2\varepsilon_{\mathbf{p}} - E_{\alpha}) + E_{\alpha}}{2\varepsilon_{\mathbf{p}} - E_{\alpha}} = 1 + \frac{E_{\alpha}}{2\varepsilon_{\mathbf{p}} - E_{\alpha}}$$
(B37)

Hence the first sum becomes

$$\sum_{\mathbf{p}} \phi_{\alpha}(\mathbf{p}) \, 2\varepsilon_{\mathbf{p}} \, A_{\mathbf{p}}^{\dagger} = \sum_{\mathbf{p}} \left[ 1 + \frac{E_{\alpha}}{2\varepsilon_{\mathbf{p}} - E_{\alpha}} \right] A_{\mathbf{p}}^{\dagger} = A^{\dagger} + E_{\alpha} \sum_{\mathbf{p}} \frac{A_{\mathbf{p}}^{\dagger}}{2\varepsilon_{\mathbf{p}} - E_{\alpha}} = A^{\dagger} + E_{\alpha} B_{\alpha}^{\dagger}. \tag{B38}$$

Therefore,

$$[H, B_{\alpha}^{\dagger}] = E_{\alpha} B_{\alpha}^{\dagger} + A^{\dagger} + g A^{\dagger} K_{\alpha}, \qquad K_{\alpha} \equiv \sum_{\mathbf{p}} \phi_{\alpha}(\mathbf{p}) (1 - N_{\mathbf{p}}). \tag{B39}$$

We will need how  $K_{\alpha}$  commutes with  $B_{\beta}^{\dagger}$ . Using Eq. (B31) with Eq. (B30),

$$[K_{\alpha}, B_{\beta}^{\dagger}] = \sum_{\mathbf{k}} \frac{1 - N_{\mathbf{k}}}{2\varepsilon_{\mathbf{k}} - E_{\alpha}} \sum_{\mathbf{p}} \frac{1}{2\varepsilon_{\mathbf{p}} - E_{\beta}} [1 - N_{\mathbf{k}}, A_{\mathbf{p}}^{\dagger}] = -2 \sum_{\mathbf{k}} \frac{A_{\mathbf{k}}^{\dagger}}{(2\varepsilon_{\mathbf{k}} - E_{\alpha})(2\varepsilon_{\mathbf{k}} - E_{\beta})}.$$
 (B40)

Using the identity  $\frac{1}{x-a} - \frac{1}{x-b} = \frac{b-a}{(x-a)(x-b)}$  with  $x \equiv 2\varepsilon_k$ ,  $a \equiv E_\alpha$ ,  $b \equiv E_\beta$ , we obtain

$$\frac{1}{(2\varepsilon_{\mathbf{k}} - E_{\alpha})(2\varepsilon_{\mathbf{k}} - E_{\beta})} = \frac{1}{E_{\beta} - E_{\alpha}} \left[ \frac{1}{2\varepsilon_{\mathbf{k}} - E_{\alpha}} - \frac{1}{2\varepsilon_{\mathbf{k}} - E_{\beta}} \right].$$
(B41)

Multiplying by  $A_{\mathbf{k}}^{\dagger}$  and summing over k gives

$$\sum_{\mathbf{k}} \frac{A_{\mathbf{k}}^{\dagger}}{(2\varepsilon_{\mathbf{k}} - E_{\alpha})(2\varepsilon_{\mathbf{k}} - E_{\beta})} = \frac{1}{E_{\beta} - E_{\alpha}} \sum_{\mathbf{k}} \left[ \frac{A_{\mathbf{k}}^{\dagger}}{2\varepsilon_{\mathbf{k}} - E_{\alpha}} - \frac{A_{\mathbf{k}}^{\dagger}}{2\varepsilon_{\mathbf{k}} - E_{\beta}} \right] = \frac{1}{E_{\beta} - E_{\alpha}} \left( B_{\alpha}^{\dagger} - B_{\beta}^{\dagger} \right) = \frac{B_{\alpha}^{\dagger} - B_{\beta}^{\dagger}}{E_{\alpha} - E_{\beta}} (-1).$$
(B42)

Flipping the sign in the denominator,

$$\sum_{\mathbf{k}} \frac{A_{\mathbf{k}}^{\dagger}}{(2\varepsilon_{\mathbf{k}} - E_{\alpha})(2\varepsilon_{\mathbf{k}} - E_{\beta})} = \frac{B_{\alpha}^{\dagger} - B_{\beta}^{\dagger}}{E_{\alpha} - E_{\beta}}.$$
(B43)

Insert them into Eq. (B40):

$$[K_{\alpha}, B_{\beta}^{\dagger}] = -2 \frac{B_{\alpha}^{\dagger} - B_{\beta}^{\dagger}}{E_{\alpha} - E_{\beta}}.$$
 (B44)

Equivalently,  $K_{\alpha}B_{\beta}^{\dagger} = B_{\beta}^{\dagger}K_{\alpha} - 2\frac{B_{\alpha}^{\dagger} - B_{\beta}^{\dagger}}{E_{\alpha} - E_{\beta}}$ . Now act with H on the ansatz state  $|\Psi_{2M}\rangle = \prod_{\lambda=1}^{M} B_{\lambda}^{\dagger}|0\rangle$ . Since  $H|0\rangle = 0$ , the commutator trick gives

$$\begin{split} H \big| \Psi_{2M} \big\rangle &= H \left( \prod_{\alpha=1}^{M} B_{\alpha}^{\dagger} \right) |0\rangle = \left( [H, \prod_{\alpha=1}^{M} B_{\alpha}^{\dagger}] + \prod_{\alpha=1}^{M} B_{\alpha}^{\dagger} H \right) |0\rangle \\ &= [H, \prod_{\alpha=1}^{M} B_{\alpha}^{\dagger}] |0\rangle \quad \text{(because } H |0\rangle = 0) \\ &= \left( \sum_{\alpha=1}^{M} \left( \prod_{\gamma < \alpha} B_{\gamma}^{\dagger} \right) [H, B_{\alpha}^{\dagger}] \left( \prod_{\gamma > \alpha} B_{\gamma}^{\dagger} \right) \big) |0\rangle \quad \text{(using } [H, XY] = [H, X]Y + X[H, Y] \right) \\ &= \sum_{\alpha=1}^{M} [H, B_{\alpha}^{\dagger}] \prod_{\gamma \neq \alpha} B_{\gamma}^{\dagger} |0\rangle. \end{split}$$

Inserting Eq. (B39), we obtain

$$H|\Psi_{2M}\rangle = \sum_{\alpha=1}^{M} \left( E_{\alpha} B_{\alpha}^{\dagger} + A^{\dagger} + g A^{\dagger} K_{\alpha} \right) \prod_{\gamma \neq \alpha} B_{\gamma}^{\dagger} |0\rangle.$$
 (B46)

The first term simplifies because all B's commute:

$$\sum_{\alpha} E_{\alpha} B_{\alpha}^{\dagger} \prod_{\gamma \neq \alpha} B_{\gamma}^{\dagger} |0\rangle = \sum_{\alpha} E_{\alpha} \left( \prod_{\gamma \neq \alpha} B_{\gamma}^{\dagger} \right) B_{\alpha}^{\dagger} |0\rangle = \sum_{\alpha} E_{\alpha} \left( \prod_{\lambda=1}^{M} B_{\lambda}^{\dagger} \right) |0\rangle = \left( \sum_{\alpha} E_{\alpha} \right) |\Psi_{2M}\rangle. \tag{B47}$$

We now push  $K_{\alpha}$  to the right in Eq. (B46). Using Eq. (B44) repeatedly,

$$K_{\alpha} \prod_{\gamma \neq \alpha} B_{\gamma}^{\dagger} = \left( \prod_{\gamma \neq \alpha} B_{\gamma}^{\dagger} \right) K_{\alpha} - 2 \sum_{\beta (\neq \alpha)} \frac{B_{\alpha}^{\dagger} - B_{\beta}^{\dagger}}{E_{\alpha} - E_{\beta}} \prod_{\substack{\gamma \neq \alpha \\ \gamma \neq \beta}} B_{\gamma}^{\dagger}. \tag{B48}$$

Acting on  $|0\rangle$  and using  $N_{\mathbf{k}}|0\rangle = 0$  gives  $K_{\alpha}|0\rangle = \sum_{\mathbf{k}} \phi_{\alpha}(\mathbf{k})|0\rangle$ . Therefore,

$$K_{\alpha} \prod_{\gamma \neq \alpha} B_{\gamma}^{\dagger} |0\rangle = \left( \prod_{\gamma \neq \alpha} B_{\gamma}^{\dagger} \right) K_{\alpha} |0\rangle - 2 \sum_{\beta(\neq \alpha)} \frac{B_{\alpha}^{\dagger} - B_{\beta}^{\dagger}}{E_{\alpha} - E_{\beta}} \prod_{\substack{\gamma \neq \alpha \\ \gamma \neq \beta}} B_{\gamma}^{\dagger} |0\rangle$$

$$= \left( \prod_{\gamma \neq \alpha} B_{\gamma}^{\dagger} \right) \left( \sum_{\mathbf{k}} \phi_{\alpha}(\mathbf{k}) (1 - N_{\mathbf{k}}) \right) |0\rangle - 2 \sum_{\beta(\neq \alpha)} \frac{B_{\alpha}^{\dagger} - B_{\beta}^{\dagger}}{E_{\alpha} - E_{\beta}} \prod_{\substack{\gamma \neq \alpha \\ \gamma \neq \beta}} B_{\gamma}^{\dagger} |0\rangle$$

$$= \left( \sum_{\mathbf{k}} \phi_{\alpha}(\mathbf{k}) \right) \prod_{\gamma \neq \alpha} B_{\gamma}^{\dagger} |0\rangle - 2 \sum_{\beta(\neq \alpha)} \frac{B_{\alpha}^{\dagger} - B_{\beta}^{\dagger}}{E_{\alpha} - E_{\beta}} \prod_{\substack{\gamma \neq \alpha \\ \gamma \neq \beta}} B_{\gamma}^{\dagger} |0\rangle \quad \text{(since } N_{\mathbf{k}} |0\rangle = 0)$$

Insert Eq. (B47) and Eq. (B49) into Eq. (B46):

$$H|\Psi_{2M}\rangle = \left(\sum_{\alpha} E_{\alpha}\right)|\Psi_{2M}\rangle + A^{\dagger} \sum_{\alpha} \left[1 + g\sum_{\mathbf{k}} \phi_{\alpha}(\mathbf{k})\right] \prod_{\gamma \neq \alpha} B_{\gamma}^{\dagger}|0\rangle - 2gA^{\dagger} \sum_{\alpha} \sum_{\beta(\neq \alpha)} \frac{B_{\alpha}^{\dagger} - B_{\beta}^{\dagger}}{E_{\alpha} - E_{\beta}} \prod_{\substack{\gamma \neq \alpha \\ \gamma \neq \beta}} B_{\gamma}^{\dagger}|0\rangle. \tag{B50}$$

Notice that the first term is already proportional to  $|\Psi_{2M}\rangle$ , so it contributes directly to the eigenvalue once the other terms cancel. Now our work is to show the second and third terms cancel term-by-term when Eq. (B25) holds. Define the M linearly independent states

$$|\Phi_{\mu}\rangle \equiv \mathcal{A}^{\dagger} \prod_{\gamma \neq \mu} B_{\gamma}^{\dagger} |0\rangle, \qquad \mu = 1, \dots, M.$$
 (B51)

Each  $|\Phi_{\mu}\rangle$  is "the product of all  $B_{\gamma}^{\dagger}$  except  $B_{\mu}^{\dagger}$ , then one extra  $\mathcal{A}^{\dagger}$ ." Our goal is to rewrite the 2nd and 3rd terms of Eq. (B50) as a linear combination  $\sum_{\mu} C_{\mu} |\Phi_{\mu}\rangle$ . Since the  $|\Phi_{\mu}\rangle$  are independent, we must have  $C_{\mu} = 0$  for every  $\mu$ . Those  $C_{\mu} = 0$  will be exactly Eq. (B25). For contribution from the second term, to look like  $|\Phi_{\mu}\rangle$ , the index must be  $\alpha = \mu$ . Hence,

$$C_{\mu}^{(2)} = \left[1 + g \sum_{\mathbf{k}} \phi_{\mu}(\mathbf{k})\right]. \tag{B52}$$

For contribution from the third term, the third line contains, for ordered pairs  $(\alpha, \beta)$  with  $\beta \neq \alpha$ ,

$$-2g\mathcal{A}^{\dagger} \frac{B_{\alpha}^{\dagger} - B_{\beta}^{\dagger}}{E_{\alpha} - E_{\beta}} \prod_{\substack{\gamma \neq \alpha \\ \gamma \neq \beta}} B_{\gamma}^{\dagger} |0\rangle. \tag{B53}$$

For a fixed  $\mu$ , the state  $|\Phi_{\mu}\rangle$  contains all  $B_{\gamma}^{\dagger}$  except  $B_{\mu}^{\dagger}$ . Thus only two cases contribute to the coefficient of  $|\Phi_{\mu}\rangle$  in

Case A:  $\alpha = \mu$ ,  $\beta \neq \mu$ . The product is missing  $B_{\mu}^{\dagger}$  and  $B_{\beta}^{\dagger}$ ; from  $(B_{\mu}^{\dagger} - B_{\beta}^{\dagger})$  only the  $-B_{\beta}^{\dagger}$  term yields  $|\Phi_{\mu}\rangle$ . The contribution is  $+\frac{2g}{E_{\mu}-E_{\beta}}$ .

Case B:  $\beta = \mu$ ,  $\alpha \neq \mu$ . The product is missing  $B_{\alpha}^{\dagger}$  and  $B_{\mu}^{\dagger}$ ; from  $(B_{\alpha}^{\dagger} - B_{\mu}^{\dagger})$  only the  $+B_{\alpha}^{\dagger}$  term yields  $|\Phi_{\mu}\rangle$ . The contribution is  $-\frac{2g}{E_{\alpha}-E_{\mu}} = +\frac{2g}{E_{\mu}-E_{\alpha}}$ . Summing over the remaining index gives

$$C_{\mu}^{(3)} = 2g \sum_{\nu \neq \mu} \frac{1}{E_{\mu} - E_{\nu}}.$$
 (B54)

Adding the second–line coefficient  $C_{\mu}^{(2)} = 1 + g \sum_{k} \phi_{\mu}(k)$  with  $\phi_{\mu}(k) = \frac{1}{2\varepsilon_{k} - E_{\mu}}$ , we obtain

$$C_{\mu} = \left[1 + g \sum_{\mathbf{k}} \phi_{\mu}(\mathbf{k})\right] + 2g \sum_{\nu \neq \mu} \frac{1}{E_{\mu} - E_{\nu}}.$$
 (B55)

Equivalently,

$$C_{\mu} = g \left[ \frac{1}{g} + \sum_{\mathbf{k}} \phi_{\mu}(\mathbf{k}) - \sum_{\nu \neq \mu} \frac{2}{E_{\nu} - E_{\mu}} \right]. \tag{B56}$$

Since the  $\{|\Phi_{\mu}\rangle\}$  are linearly independent, the unwanted pieces vanish iff  $C_{\mu}=0$  for every  $\mu$ . Dropping the overall factor  $g\neq 0$  and substituting  $\phi_{\mu}(\mathbf{k})$  yields the Richardson equations

$$\frac{1}{g} + \sum_{k} \frac{1}{2\varepsilon_{k} - E_{\mu}} - \sum_{\nu \neq \mu} \frac{2}{E_{\nu} - E_{\mu}} = 0, \qquad \mu = 1, \dots, M.$$
 (B57)

When these M equations hold, the second and third lines of Eq. (B50) cancel identically, leaving

$$H|\Psi_{2M}\rangle = \left(\sum_{\alpha=1}^{M} E_{\alpha}\right)|\Psi_{2M}\rangle,$$
 (B58)

as claimed [95].

b. Pair-Pair Correlators: Gaudin Matrix and Exact Formula

With the Cooper-pair operator  $A_k^{\dagger}$  and  $A_k$  defined in Eq. (B21), for a general many-body state, the pair–pair correlator is

$$\widetilde{C}_{kk'} \equiv \langle A_k^{\dagger} A_{k'} \rangle - \langle A_k^{\dagger} \rangle \langle A_{k'} \rangle ,$$
(B59)

where  $\langle ... \rangle$  is the average with respect to the state of interest. In the Richardson model we work with number-conserving eigenstates  $|\Psi_{2M}\rangle$  (fixed particle number 2M). Since  $A_{\mathbf{k}}$  lowers particle number by two,  $A_{\mathbf{k}}|\Psi_{2M}\rangle$  lies in the 2M-2 sector and is orthogonal to  $|\Psi_{2M}\rangle$ , hence

$$\langle A_{\mathbf{k}} \rangle = \langle \Psi_{2M} | A_{\mathbf{k}} | \Psi_{2M} \rangle = 0.$$
 (B60)

Therefore the connected and full correlators coincide.

$$\widetilde{C}_{kk'} = \langle A_k^{\dagger} A_{k'} \rangle. \tag{B61}$$

Writing out  $A_k^{\dagger}$  and  $A_{k'}$ ,

$$\langle A_{\mathbf{k}}^{\dagger} A_{\mathbf{k}'} \rangle = \langle c_{\mathbf{k}\uparrow}^{\dagger} c_{-\mathbf{k}\downarrow}^{\dagger} c_{-\mathbf{k}'\downarrow} c_{\mathbf{k}'\uparrow} \rangle, \tag{B62}$$

which is exactly the Cooper-channel combination of the 2-RDM defined in Eq. (1), i.e.

$$C_{kk'} \equiv \widetilde{C}_{kk'} = O_{k\uparrow, -k\downarrow, k'\uparrow, -k'\downarrow}. \tag{B63}$$

(For U(1)-breaking mean-field states we may have  $\langle A_{\mathbf{k}} \rangle \neq 0$ , in which case the connected correlator (B59) differs from the full 2-RDM matrix element by  $\langle A_{\mathbf{k}}^{\dagger} \rangle \langle A_{\mathbf{k'}} \rangle$ ; in our number-conserving case, (B60) ensures they are identical.)

Now we derive a general expression of  $\langle \Psi_{2M} | A_{\mathbf{k}}^{\dagger} A_{\mathbf{k}'} | \Psi_{2M} \rangle$  as shown in Ref. [116]. Firstly, push  $A_{\mathbf{k}'}$  through the ket using  $[A_{\mathbf{k}}, A_{\mathbf{p}}^{\dagger}] = \delta_{\mathbf{k}\mathbf{p}} (1 - N_{\mathbf{k}})$  and  $(1 - N_{\mathbf{k}})|0\rangle = |0\rangle$ . Then,

$$A_{\mathbf{k}'} \left( \prod_{\beta=1}^{M} B_{\beta}^{\dagger} \right) |0\rangle = \sum_{\mu=1}^{M} \left( \prod_{\beta<\mu} B_{\beta}^{\dagger} \right) [A_{\mathbf{k}'}, B_{\mu}^{\dagger}] \left( \prod_{\beta>\mu} B_{\beta}^{\dagger} \right) |0\rangle \qquad \text{(use } [X, YZ] = [X, Y]Z + Y[X, Z] \text{ with } X = A_{\mathbf{k}'})$$
(B64)

$$= \sum_{\mu=1}^{M} \left( \prod_{\beta < \mu} B_{\beta}^{\dagger} \right) \left( \sum_{\boldsymbol{p}} \phi_{\mu}(\boldsymbol{p}) \left[ A_{\boldsymbol{k}'}, A_{\boldsymbol{p}}^{\dagger} \right] \right) \left( \prod_{\beta > \mu} B_{\beta}^{\dagger} \right) |0\rangle \qquad \text{(since } B_{\mu}^{\dagger} = \sum_{\boldsymbol{p}} \phi_{\mu}(\boldsymbol{p}) A_{\boldsymbol{p}}^{\dagger} )$$
(B65)

$$= \sum_{\mu=1}^{M} \left( \prod_{\beta < \mu} B_{\beta}^{\dagger} \right) \left( \sum_{\boldsymbol{p}} \phi_{\mu}(\boldsymbol{p}) \, \delta_{k'p} \left( 1 - N_{\boldsymbol{k}'} \right) \right) \left( \prod_{\beta > \mu} B_{\beta}^{\dagger} \right) |0\rangle \qquad \text{(because } [A_{\boldsymbol{k}'}, A_{\boldsymbol{p}}^{\dagger}] = \delta_{k'p} (1 - N_{\boldsymbol{k}'})) \tag{B66}$$

$$= \sum_{\mu=1}^{M} \phi_{\mu}(\mathbf{k}') \left( \prod_{\beta < \mu} B_{\beta}^{\dagger} \right) (1 - N_{\mathbf{k}'}) \left( \prod_{\beta > \mu} B_{\beta}^{\dagger} \right) |0\rangle$$
(B67)

$$= \sum_{\mu=1}^{M} \phi_{\mu}(\mathbf{k}') \left( \prod_{\beta \neq \mu} B_{\beta}^{\dagger} \right) (1 - N_{\mathbf{k}'}) |0\rangle$$
(B68)

$$= \sum_{\mu=1}^{M} \phi_{\mu}(\mathbf{k}') \left( \prod_{\beta \neq \mu} B_{\beta}^{\dagger} \right) |0\rangle, \quad \text{(since } (1 - N_{\mathbf{k}'}) |0\rangle = |0\rangle).$$
 (B69)

Secondly, push  $A_{\mathbf{k}}^{\dagger}$  through the bra, using  $[B_{\nu}, A_{\mathbf{k}}^{\dagger}] = \phi_{\nu}(\mathbf{k}) (1 - N_{\mathbf{k}})$  and  $\langle 0 | (1 - N_{\mathbf{k}}) = \langle 0 |$ , we get

$$\langle 0| \left(\prod_{\alpha=1}^{M} B_{\alpha}\right) A_{\mathbf{k}}^{\dagger} = \sum_{\nu=1}^{M} \langle 0| \left(\prod_{\alpha<\nu} B_{\alpha}\right) \left[B_{\nu}, A_{\mathbf{k}}^{\dagger}\right] \left(\prod_{\alpha>\nu} B_{\alpha}\right) \quad \text{(use } [X, YZ] = [X, Y]Z + Y[X, Z])$$

$$= \sum_{\nu=1}^{M} \langle 0| \left(\prod_{\alpha<\nu} B_{\alpha}\right) \phi_{\nu}(\mathbf{k}) \left(1 - N_{\mathbf{k}}\right) \left(\prod_{\alpha>\nu} B_{\alpha}\right) \quad \text{(since } [B_{\nu}, A_{\mathbf{k}}^{\dagger}] = \phi_{\nu}(\mathbf{k}) (1 - N_{\mathbf{k}}))$$

$$= \sum_{\nu=1}^{M} \phi_{\nu}(\mathbf{k}) \langle 0| \left(\prod_{\alpha\neq\nu} B_{\alpha}\right) \left(1 - N_{\mathbf{k}}\right)$$

$$= \sum_{\nu=1}^{M} \phi_{\nu}(\mathbf{k}) \langle 0| \left(\prod_{\alpha\neq\nu} B_{\alpha}\right) \quad \text{(because } \langle 0| (1 - N_{\mathbf{k}}) = \langle 0| \right).$$
(B70)

Define the  $(M \times M)$  overlap matrix

$$S_{\nu\mu} \equiv \langle 0| \Big(\prod_{\alpha \neq \nu} B_{\alpha}\Big) \Big(\prod_{\beta \neq \nu} B_{\beta}^{\dagger}\Big) |0\rangle. \tag{B71}$$

Combining Eq. (B70) and Eq. (B69),

$$\left\langle \Psi_{2M} \middle| A_{\mathbf{k}}^{\dagger} A_{\mathbf{k}'} \middle| \Psi_{2M} \right\rangle = \left\langle 0 \middle| \left( \prod_{\alpha=1}^{M} B_{\alpha} \right) A_{\mathbf{k}}^{\dagger} A_{\mathbf{k}'} \left( \prod_{\beta=1}^{M} B_{\beta}^{\dagger} \right) \middle| 0 \right\rangle$$
 (B72)

$$= \sum_{\nu=1}^{M} \phi_{\nu}(k) \left\langle 0 \middle| \left( \prod_{\alpha \neq \nu} B_{\alpha} \right) A_{\mathbf{k}'} \left( \prod_{\beta=1}^{M} B_{\beta}^{\dagger} \right) \middle| 0 \right\rangle \quad \text{(by Eq. (26))}$$

$$= \sum_{\nu=1}^{M} \phi_{\nu}(k) \sum_{\mu=1}^{M} \phi_{\mu}(k') \left\langle 0 \middle| \left( \prod_{\alpha \neq \nu} B_{\alpha} \right) \left( \prod_{\beta \neq \mu} B_{\beta}^{\dagger} \right) \middle| 0 \right\rangle \quad \text{(by Eq. (25))}$$

$$= \sum_{\nu=1}^{M} \sum_{\mu=1}^{M} \phi_{\nu}(k) S_{\nu\mu} \phi_{\mu}(k') \qquad (\text{def. } S_{\nu\mu} \text{ in Eq. (27)}). \tag{B75}$$

So the problem is reduced to determining  $S_{\nu\mu}$ . Use the operator  $K_{\alpha} \equiv \sum_{\boldsymbol{p}} \phi_{\alpha}(\boldsymbol{p}) (1 - N_{\boldsymbol{p}})$  introduced earlier (the same weights as  $B_{\alpha}^{\dagger}$ ). Acting on the ket, we previously derived Eq. (B49). Multiply on the left by  $\langle 0 | \prod_{\delta \neq \nu} B_{\delta}$  and use only the commutativity of all  $B^{\dagger}$  and the definition of  $S_{\nu\mu}$ :

$$\langle 0| \Big(\prod_{\delta \neq \nu} B_{\delta}\Big) K_{\alpha} \prod_{\gamma \neq \alpha} B_{\gamma}^{\dagger} |0\rangle = \Big(\sum_{\boldsymbol{p}} \phi_{\alpha}(\boldsymbol{p})\Big) \langle 0| \Big(\prod_{\delta \neq \nu} B_{\delta}\Big) \Big(\prod_{\gamma \neq \alpha} B_{\gamma}^{\dagger}\Big) |0\rangle$$

$$-2 \sum_{\beta \neq \alpha} \frac{\langle 0| \Big(\prod_{\delta \neq \nu} B_{\delta}\Big) B_{\alpha}^{\dagger} \prod_{\gamma \neq \alpha} B_{\gamma}^{\dagger} |0\rangle - \langle 0| \Big(\prod_{\delta \neq \nu} B_{\delta}\Big) B_{\beta}^{\dagger} \prod_{\gamma \neq \alpha} B_{\gamma}^{\dagger} |0\rangle}{E_{\alpha} - E_{\beta}}$$
(B76)

$$\mathcal{L}_{\alpha\nu} \equiv \langle 0 | \Big( \prod_{\delta \neq \nu} B_{\delta} \Big) K_{\alpha} \Big( \prod_{\gamma \neq \alpha} B_{\gamma}^{\dagger} \Big) | 0 \rangle = \Big( \sum_{\mathbf{p}} \phi_{\alpha}(\mathbf{p}) \Big) S_{\nu\alpha} - 2 \sum_{\beta \neq \alpha} \frac{S_{\nu\beta} - S_{\nu\alpha}}{E_{\alpha} - E_{\beta}}$$
(B77)

Split the last term and rewrite each piece as a sum over  $\mu = 1, ..., M$ :

$$\sum_{\beta \neq \alpha} \frac{S_{\nu\beta}}{E_{\alpha} - E_{\beta}} = \sum_{\mu \neq \alpha} \frac{S_{\nu\mu}}{E_{\alpha} - E_{\mu}} = \sum_{\mu=1}^{M} \left(1 - \delta_{\alpha\mu}\right) \frac{S_{\nu\mu}}{E_{\alpha} - E_{\mu}} \tag{B78}$$

where we use  $\sum_{\mu \neq \alpha} f(\mu) = \sum_{\mu} (1 - \delta_{\alpha\mu}) f(\mu)$ . And the first term is

$$\left(\sum_{\boldsymbol{p}} \phi_{\alpha}(\boldsymbol{p})\right) S_{\nu\alpha} = \sum_{\mu=1}^{M} \left(\sum_{\boldsymbol{p}} \phi_{\alpha}(\boldsymbol{p})\right) \delta_{\alpha\mu} S_{\nu\mu}.$$
 (B79)

Insert:

$$\mathcal{L}_{\alpha\nu} = \sum_{\mu=1}^{M} \left[ \left( \sum_{\boldsymbol{p}} \phi_{\alpha}(\boldsymbol{p}) \right) \delta_{\alpha\mu} - 2(1 - \delta_{\alpha\mu}) \frac{1}{E_{\alpha} - E_{\mu}} + 2 \, \delta_{\alpha\mu} \sum_{\beta \neq \alpha} \frac{1}{E_{\alpha} - E_{\beta}} \right] S_{\nu\mu}. \tag{B80}$$

Compute the same matrix element  $\mathcal{L}_{\alpha\nu}$  but act with  $K_{\alpha}$  to the left (on the bra) instead of the ket. The identical derivation gives the same expression except the sign of the second term flips inside the parentheses. Therefore, the bra-side analogue of Eq. (B49) is:

$$\langle 0| \prod_{\delta \neq \nu} B_{\delta} K_{\alpha} = \left(\sum_{\boldsymbol{p}} \phi_{\alpha}(\boldsymbol{p})\right) \langle 0| \prod_{\delta \neq \nu} B_{\delta} + 2 \sum_{\eta(\neq \nu)} \frac{B_{\eta} - B_{\alpha}}{E_{\alpha} - E_{\eta}} \langle 0| \prod_{\delta \neq \nu, \delta \neq \eta} B_{\delta}.$$
(B81)

Multiplying on the right by  $\prod_{\gamma \neq \alpha} B_{\gamma}^{\dagger} |0\rangle$  gives the bra version of Eq. (B49) for the full matrix element  $\mathcal{L}_{\alpha\nu}$ . Using the same steps as before:

$$\mathcal{L}_{\alpha\nu} = \sum_{\mu=1}^{M} \left[ \left( \sum_{\boldsymbol{p}} \phi_{\alpha}(\boldsymbol{p}) \right) \delta_{\alpha\mu} + 2(1 - \delta_{\alpha\mu}) \frac{1}{E_{\alpha} - E_{\mu}} - 2\delta_{\alpha\mu} \sum_{\beta \neq \alpha} \frac{1}{E_{\alpha} - E_{\beta}} \right] S_{\nu\mu}, \tag{B82}$$

Since both Eq. (B80) and Eq. (B82) are the same scalar  $\mathcal{L}_{\alpha\nu}$  but opposite sign,

$$0 = \sum_{\mu=1}^{M} \left[ \left( \sum_{\mathbf{p}} \phi_{\alpha}(\mathbf{p}) \right) \delta_{\alpha\mu} - 2(1 - \delta_{\alpha\mu}) \frac{1}{E_{\alpha} - E_{\mu}} + 2 \delta_{\alpha\mu} \sum_{\beta \neq \alpha} \frac{1}{E_{\alpha} - E_{\beta}} \right] S_{\nu\mu}$$
 (B83)

Using the Richardson equations Eq. (B25) to eliminate  $\sum_{\boldsymbol{p}} \phi_{\alpha}(\boldsymbol{p})$  (indeed,  $\frac{1}{g} + \sum_{\boldsymbol{p}} \phi_{\alpha}(\boldsymbol{p}) + \sum_{\beta(\neq \alpha)} \frac{2}{E_{\alpha} - E_{\beta}} = 0$  so  $\sum_{\boldsymbol{p}} \phi_{\alpha}(\boldsymbol{p}) = -\frac{1}{g} - \sum_{\beta(\neq \alpha)} \frac{2}{E_{\alpha} - E_{\beta}}$ , the coefficients here rearrange into the Gaudin (Jacobian) matrix [116]

$$G_{\alpha\mu} \equiv \frac{\partial \mathcal{R}_{\alpha}}{\partial E_{\mu}}, \qquad \mathcal{R}_{\alpha} = \frac{1}{g} + \sum_{\mathbf{p}} \frac{1}{2\varepsilon_{\mathbf{p}} - E_{\alpha}} - 2\sum_{\beta \neq \alpha} \frac{1}{E_{\beta} - E_{\alpha}}$$
 (B84)

$$G_{\alpha\mu} = \begin{cases} \sum_{\mathbf{p}} \frac{1}{(2\varepsilon_{\mathbf{p}} - E_{\alpha})^2} - \sum_{\beta \neq \alpha} \frac{2}{(E_{\beta} - E_{\alpha})^2}, & \mu = \alpha, \\ \frac{2}{(E_{\mu} - E_{\alpha})^2}, & \mu \neq \alpha. \end{cases}$$
(B85)

where  $\mathcal{R}_{\alpha}$  is the left-hand side of Eq. (B25). Thus Eq. (B82) can be written compactly as

$$\sum_{\mu=1}^{M} G_{\alpha\mu} S_{\nu\mu} = 0 \quad \text{for all } \alpha \neq \nu; \quad \sum_{\mu=1}^{M} G_{\nu\mu} S_{\nu\mu} = \langle \Psi_{2M} | \Psi_{2M} \rangle.$$
 (B86)

From the bra-ket identities derived above we obtain the linear relations

$$\sum_{\mu=1}^{M} G_{\alpha\mu} S_{\nu\mu} = \delta_{\alpha\nu} \langle \Psi_{2M} | \Psi_{2M} \rangle, \qquad \alpha = 1, \dots, M,$$
(B87)

Therefore,

$$S_{\nu\mu} = \langle \Psi_{2M} | \Psi_{2M} \rangle \left( G^{-1} \right)_{\mu\nu}. \tag{B88}$$

Introduce the M-component vector

$$\phi(\mathbf{k}) \equiv (\phi_1(\mathbf{k}), \dots, \phi_M(\mathbf{k}))^\mathsf{T}, \quad \phi_\alpha(\mathbf{k}) = \frac{1}{2\varepsilon_{\mathbf{k}} - E_\alpha},$$
 (B89)

Use Eq. (B84) and Eq. (B88) in the expression for the matrix element, we obtain

$$\langle \Psi_{2M} | A_{\mathbf{k}}^{\dagger} A_{\mathbf{k}'} | \Psi_{2M} \rangle = \langle \Psi_{2M} | \Psi_{2M} \rangle \phi(\mathbf{k})^{\mathsf{T}} G^{-1} \phi(\mathbf{k}'). \tag{B90}$$

Dividing by the norm yields the compact normalized formula

$$\frac{\left\langle \Psi_{2M} \middle| A_{\mathbf{k}}^{\dagger} A_{\mathbf{k'}} \middle| \Psi_{2M} \right\rangle}{\left\langle \Psi_{2M} \middle| \Psi_{2M} \right\rangle} = \phi(\mathbf{k})^{\mathsf{T}} G^{-1} \phi(\mathbf{k'}). \tag{B91}$$

c. Complex Rapidities, Conjugation Pairing, and Reality of Energy and Correlators

In this part we prove some useful statements. We maintain exactly the notation of Eqs. Eq. (B22)–Eq. (B26). The rapidities  $E_{\alpha}$  solve the Richardson equations Eq. (B25),

$$\frac{1}{g} + \sum_{\mathbf{k}} \frac{1}{2\varepsilon_{\mathbf{k}} - E_{\alpha}} - 2\sum_{\beta(\neq\alpha)} \frac{1}{E_{\beta} - E_{\alpha}} = 0, \qquad \alpha = 1, \dots, M,$$
(B92)

Lemma H.1 (closure under complex conjugation). Assume  $g, \varepsilon_k \in \mathbb{R}$ . If  $\{E_\alpha\}_{\alpha=1}^M$  solves Eq. (B25), then the conjugated set  $\{E_\alpha^*\}_{\alpha=1}^M$  also solves Eq. (B25).

*Proof.* Taking complex conjugates of Eq. (B25) and using the reality of  $g, \varepsilon_k$  gives

$$\frac{1}{g} + \sum_{\mathbf{k}} \frac{1}{2\varepsilon_{\mathbf{k}} - E_{\alpha}^*} - 2\sum_{\beta(\neq\alpha)} \frac{1}{E_{\beta}^* - E_{\alpha}^*} = 0, \tag{B93}$$

which is the same system for the conjugated set.

Corollary H.2 (pairing). Because Eq. (B25) is permutation-invariant in  $\alpha$ , any non-real rapidity must be accompanied by its complex conjugate. After relabeling,

$$\{E_{\alpha}\} = \{\text{real roots}\} \cup \{z_1, z_1^*, \dots, z_r, z_r^*\}.$$
 (B94)

We can also show an explicit case where no purely real solution exists (complex roots are necessary): Take M = 2 and two single-particle levels symmetric about 0:

$$2\varepsilon_1 = -a, \quad 2\varepsilon_2 = +a, \quad a > 0 \quad \text{(i.e. } \varepsilon_1 = -a/2, \varepsilon_2 = +a/2\text{)}.$$
 (B95)

Seek two rapidities  $E_1, E_2$ . By Corollary H.2, a non-real solution can be written as a conjugate pair

$$E_1 = x + iy, \qquad E_2 = x - iy, \qquad x, y \in \mathbb{R}. \tag{B96}$$

Using Eq. (B25) with the two levels  $\{\pm a\}$  (Note  $E_2-E_1=-2iy$  and  $E_1-E_2=+2iy$ ),

$$0 = \frac{1}{g} + \frac{1}{-a - (x + iy)} + \frac{1}{a - (x + iy)} - \frac{2}{E_2 - E_1},$$

$$0 = \frac{1}{g} + \frac{1}{-a - (x - iy)} + \frac{1}{a - (x - iy)} - \frac{2}{E_1 - E_2}.$$
(B97)

Add the equations (a purely real relation fixing x and y given g):

$$0 = \frac{2}{g} + \sum_{i=1}^{2} \left( \frac{1}{2\varepsilon_i - (x+iy)} + \frac{1}{2\varepsilon_i - (x-iy)} \right).$$
 (B98)

Subtract the second from the first (an imaginary relation):

$$0 = \sum_{i=1}^{2} \left( \frac{1}{2\varepsilon_{i} - (x+iy)} - \frac{1}{2\varepsilon_{i} - (x-iy)} \right) - \frac{4}{E_{2} - E_{1}} = \sum_{i=1}^{2} \frac{2iy}{(2\varepsilon_{i} - x)^{2} + y^{2}} + \frac{2}{iy}.$$
 (B99)

Divide by 2i:

$$0 = y \sum_{i=1}^{2} \frac{1}{(2\varepsilon_i - x)^2 + y^2} - \frac{1}{y},$$
(B100)

hence

$$y^{2} = \frac{1}{\sum_{i=1}^{2} \frac{1}{(2\varepsilon_{i} - x)^{2} + y^{2}}} > 0.$$
 (B101)

Therefore  $y \neq 0$  and  $E_{1,2} = x \pm iy$  are necessarily complex in this case. Notice that the energy  $E = \sum_{\alpha} E_{\alpha}$  is real as expected (it is an observable) as non-real rapidities come in conjugate pairs, contributing  $z + z^* = 2\operatorname{Re} z \in \mathbb{R}$ . On the other hand, the pair-pair correlator is not required to be real in general, but for Richardson eigenstates, it is real as we can show below.

From Eq. (B91), the normalized pair-pair correlation function has the compact form

$$Q(k, k') := \phi(\mathbf{k})^{\mathsf{T}} G^{-1} \phi(\mathbf{k}'), \qquad \phi_{\alpha}(\mathbf{k}) = \frac{1}{2\varepsilon_{\mathbf{k}} - E_{\alpha}}, \tag{B102}$$

with the Gaudin (Jacobian) matrix  $G = (G_{\alpha\beta})$  symmetric:

$$G_{\alpha\beta} = \begin{cases} \sum_{\mathbf{p}} \frac{1}{(2\varepsilon_{\mathbf{p}} - E_{\alpha})^2} - \sum_{\gamma \neq \alpha} \frac{2}{(E_{\gamma} - E_{\alpha})^2}, & \alpha = \beta, \\ \frac{2}{(E_{\beta} - E_{\alpha})^2}, & \alpha \neq \beta, \end{cases} \Rightarrow G^{\mathsf{T}} = G, (G^{-1})^{\mathsf{T}} = G^{-1}. \tag{B103}$$

Let P be the permutation matrix that exchanges each non-real rapidity with its conjugate partner and fixes real ones  $(P^{-1} = P^{\mathsf{T}} = P)$ . From the definitions,

$$\phi(\mathbf{k})^* = P \phi(\mathbf{k}), \quad G^* = P G P^{\mathsf{T}}. \tag{B104}$$

Conjugating Eq. (B102) and using Eq. (B104).

$$Q(\mathbf{k}, \mathbf{k}')^* = (\phi(\mathbf{k})^\mathsf{T} G^{-1} \phi(\mathbf{k}'))^*$$

$$= \phi(\mathbf{k}')^{*\mathsf{T}} (G^{-1})^* \phi(\mathbf{k})^* = (P\phi(\mathbf{k}'))^\mathsf{T} (PG^{-1}P^\mathsf{T}) (P\phi(\mathbf{k}))$$

$$= \phi(\mathbf{k}')^\mathsf{T} (P^\mathsf{T} P) G^{-1} (P^\mathsf{T} P) \phi(\mathbf{k}) = \phi(\mathbf{k}')^\mathsf{T} G^{-1} \phi(\mathbf{k}).$$
(B105)

Since  $G^{-1}$  is symmetric,  $\phi(\mathbf{k}')^{\mathsf{T}}G^{-1}\phi(\mathbf{k}) = \phi(\mathbf{k})^{\mathsf{T}}G^{-1}\phi(\mathbf{k}') = Q(\mathbf{k}, \mathbf{k}')$ . Therefore

$$Q(\mathbf{k}, \mathbf{k}')^* = Q(\mathbf{k}, \mathbf{k}') \implies Q(\mathbf{k}, \mathbf{k}') \in \mathbb{R}.$$
 (B106)

d. Numerical Exact Pair-Pair Correlator Data

We solve the Richardson equations using the eigenvalue-based variables (EBV) formulation for  $v_i = g \Lambda_i$  [117], advance in g via a predictor-corrector plus Newton refinement, and reconstruct the rapidities through a Heine-Stieltjes polynomial collocation with Laguerre root-finding [118]. We consider the Richardson model. The number of (timereversal representative) levels is  $\Omega$ , and the number of Cooper pairs is M (electron filling  $\nu = 1/4$ ). On an  $L \times L$  BZ mesh we sample

$$\mathbf{k} = (k_x, k_y), \qquad k_x = \frac{2\pi}{L} n_x, \quad k_y = \frac{2\pi}{L} n_y, \qquad n_x, n_y \in \{0, 1, \dots, L-1\},$$
 (B107)

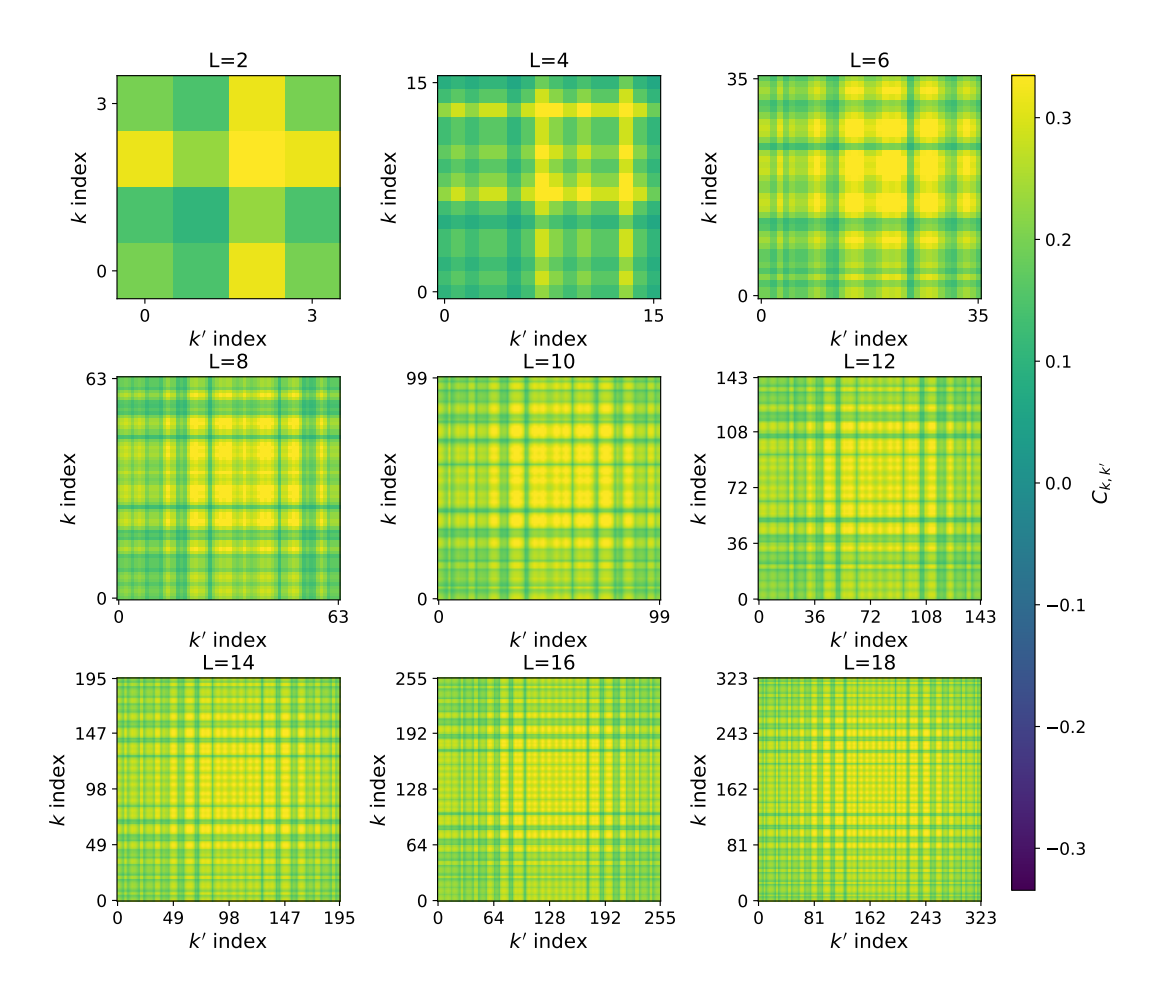


FIG. 7. Exact pair—pair correlators from the Richardson model across mesh sizes. Heat maps of the ground-state  $C_{k,k'}$  on the BZ for  $L=2,\ldots,18$  (time-reversal representatives expanded back to the full grid), computed from the exact Richardson solution. All panels share a single, zero-centered color scale (limits set by the 99th percentile of  $|C_{k,k'}|$ ).

with single-particle dispersion

$$\varepsilon_{\mathbf{k}} = t(\cos k_x + \cos k_y). \tag{B108}$$

We choose t = 0.1 in this work. The Richardson equations [93–95] as we saw are Eq. (B25),

$$1 + \frac{g}{2} \sum_{k=1}^{\Omega} \frac{1}{\varepsilon_k - E_\alpha} - g \sum_{\beta \neq \alpha} \frac{1}{E_\beta - E_\alpha} = 0, \quad \alpha = 1, \dots, M,$$
 (B109)

where adopt the numerical convention obtained by rescaling the one-body energies and coupling as  $\varepsilon_{\mathbf{k}}^{(\text{new})} = 2\varepsilon_{\mathbf{k}}$  and  $g^{(\text{new})} = 2g$ , so that  $B_{\alpha}^{\dagger} = \sum_{\mathbf{k}} A_{\mathbf{k}}^{\dagger}/(\varepsilon_{\mathbf{k}} - E_{\alpha})$ ; the physics is unchanged. For  $g \to 0^-$  the ground state connects to the Fermi sea with the M lowest  $\varepsilon_i$  occupied. Rapidities may be real or occur in complex-conjugate pairs; all physical observables remain real because they are symmetric functions of  $\{E_{\alpha}\}$ . A numerical challenge is that Eq. Eq. (B109) contains poles both at  $E_{\alpha} \to \varepsilon_i$  and  $E_{\alpha} \to E_{\beta}$ . We therefore pass to pole-free eigenvalue-based variables. Define, for each level i [117],

$$\Lambda_i \equiv \sum_{\alpha=1}^M \frac{1}{\varepsilon_i - E_\alpha}, \quad i = 1, \dots, \Omega$$
 (B110)

Sum over  $\alpha$ :

$$0 = \sum_{\alpha=1}^{M} \left[ 1 + \frac{g}{2} \sum_{i=1}^{\Omega} \frac{1}{\varepsilon_i - E_{\alpha}} - g \sum_{\substack{\beta=1\\\beta \neq \alpha}}^{M} \frac{1}{E_{\beta} - E_{\alpha}} \right] = \underbrace{\sum_{\alpha=1}^{M} 1 + \frac{g}{2} \sum_{i=1}^{\Omega} \sum_{\alpha=1}^{M} \frac{1}{\varepsilon_i - E_{\alpha}} - g \sum_{\alpha=1}^{M} \sum_{\substack{\beta=1\\\beta \neq \alpha}}^{M} \frac{1}{E_{\beta} - E_{\alpha}}$$
(B111)

where the last term is  $\sum_{\alpha=1}^{M} \sum_{\substack{\beta=1\\\beta\neq\alpha}}^{M} \frac{1}{E_{\beta}-E_{\alpha}} = \frac{1}{2} \sum_{\substack{\alpha,\beta=1\\\alpha\neq\beta}}^{M} \left(\frac{1}{E_{\beta}-E_{\alpha}} + \frac{1}{E_{\alpha}-E_{\beta}}\right) = 0$ . Thus Eq. (B111) becomes

$$M + \frac{g}{2} \sum_{i=1}^{\Omega} \Lambda_i = 0 \quad \Longrightarrow \quad \sum_{i=1}^{\Omega} \Lambda_i = -\frac{2M}{g}$$
 (B112)

Multiply Eq. (B109) by  $1/(\varepsilon_i - E_\alpha)$  and sum over  $\alpha$ :

$$0 = \sum_{\alpha=1}^{M} \frac{1}{\varepsilon_{i} - E_{\alpha}} \left[ \frac{2}{g} + \sum_{k=1}^{\Omega} \frac{1}{\varepsilon_{k} - E_{\alpha}} - 2 \sum_{\beta \neq \alpha} \frac{1}{E_{\beta} - E_{\alpha}} \right]$$

$$= \frac{2}{g} \sum_{\alpha} \frac{1}{\varepsilon_{i} - E_{\alpha}} + \sum_{\alpha} \sum_{k} \frac{1}{(\varepsilon_{k} - E_{\alpha})(\varepsilon_{i} - E_{\alpha})} - 2 \sum_{\alpha} \sum_{\beta \neq \alpha} \frac{1}{(E_{\beta} - E_{\alpha})(\varepsilon_{i} - E_{\alpha})}$$

$$= \frac{2}{g} \Lambda_{i} + \left[ \sum_{\alpha} \frac{1}{(\varepsilon_{i} - E_{\alpha})^{2}} + \sum_{k \neq i} \sum_{\alpha} \frac{1}{(\varepsilon_{k} - E_{\alpha})(\varepsilon_{i} - E_{\alpha})} \right] + \sum_{\substack{\alpha, \beta \\ \alpha \neq \beta}} \frac{1}{(\varepsilon_{i} - E_{\alpha})(\varepsilon_{i} - E_{\beta})}$$

$$= \frac{2}{g} \Lambda_{i} + S_{i} + \sum_{k \neq i} \sum_{\alpha} \frac{1}{\varepsilon_{i} - \varepsilon_{k}} \left[ \frac{1}{\varepsilon_{k} - E_{\alpha}} - \frac{1}{\varepsilon_{i} - E_{\alpha}} \right] + \sum_{\substack{\alpha, \beta \\ \alpha \neq \beta}} \frac{1}{(\varepsilon_{i} - E_{\alpha})(\varepsilon_{i} - E_{\beta})}$$

$$= \frac{2}{g} \Lambda_{i} + S_{i} + \sum_{k \neq i} \frac{\Lambda_{k} - \Lambda_{i}}{\varepsilon_{i} - \varepsilon_{k}} + (\Lambda_{i}^{2} - S_{i})$$

$$= \frac{2}{g} \Lambda_{i} + \sum_{k \neq i} \frac{\Lambda_{k} - \Lambda_{i}}{\varepsilon_{i} - \varepsilon_{k}} + \Lambda_{i}^{2}$$
(B113)

where  $S_i \equiv \sum_{\alpha=1}^M \frac{1}{(\varepsilon_i - E_\alpha)^2}$ . Multiply Eq. (B113) by  $g^2$  and set  $v_i = g\Lambda_i$ :

$$v_i^2 + 2v_i - g \sum_{k \neq i} \frac{v_i - v_k}{\varepsilon_i - \varepsilon_k} = 0, \quad i = 1, \dots, \Omega,$$
(B114)

with the sum rule from Eq. (B112):

$$\sum_{i=1}^{\Omega} v_i + 2M = 0. \tag{B115}$$

So instead of solving for the M rapidities  $E_{\alpha}$  directly, we solve these  $\Omega$  quadratic equations for  $\{\Lambda_i\}$  (or  $\{v_i\}$ ), which is smooth and well-suited to Newton steps and homotopy in g; then we reconstruct the  $E_{\alpha}$  afterwards. At  $g \to 0^-$  the ground state is the filled Fermi sea (the M lowest  $\varepsilon_i$ ). We construct an analytic first guess for  $\{v_i\}$  at tiny |g| from first-order perturbation around that occupation pattern, and adiabatically continue to the target g < 0 via small increments in g with Newton updates on Eq. (B114). This tracks the same eigenbranch and hence the many-body ground state for the given  $(\{\varepsilon_i\}, M, g)$ . Given  $\{\Lambda_i\}$ , the rapidities  $\{E_{\alpha}\}$  are the zeros of a degree-M polynomial  $g(z) = \prod_{\alpha=1}^{M} (z - E_{\alpha})$  that satisfies the Heine–Stieltjes ODE

$$y''(z) + F(z)y'(z) - G(z)y(z) = 0, F(z) = \frac{2}{g} + \sum_{k=1}^{\Omega} \frac{1}{\varepsilon_k - z}, G(z) = \sum_{i=1}^{\Omega} \frac{\Lambda_i}{\varepsilon_i - z},$$
 (B116)

see [117, 118]. A Lagrange-interpolation representation of y on support points  $\{z_j\}$  away from  $\{\varepsilon_i\}$  gives a linear system for the interpolation weights; the roots of y (found e.g. by Laguerre's method) are precisely  $\{E_{\alpha}\}$ . As a check,

$\overline{L}$	g	u	$\max_{\alpha}  R_{\alpha} $	$\max_i  \mathrm{EBV}_i $	$\left \sum_{i} v_{i} + 2M\right $
2	-0.250000	-1	$1.11 \times 10^{-16}$	$9.42 \times 10^{-12}$	0.00
4	-0.062500	-1	$5.01 \times 10^{-16}$	$3.82 \times 10^{-12}$	0.00
6	-0.027778	-1	$2.56 \times 10^{-15}$	$5.91 \times 10^{-13}$	$1.78 \times 10^{-15}$
8	-0.015625	-1	$5.65 \times 10^{-12}$	$1.01 \times 10^{-13}$	0.00
10	-0.010000	-1	$1.34 \times 10^{-12}$	$4.66 \times 10^{-14}$	0.00
12	-0.006944	-1	$9.74 \times 10^{-15}$	$2.89 \times 10^{-15}$	$-7.11 \times 10^{-15}$
14	-0.005102	-1	$1.25 \times 10^{-14}$	$2.33 \times 10^{-15}$	$-7.11 \times 10^{-15}$
16	-0.003906	-1	$2.63 \times 10^{-14}$	$2.41 \times 10^{-14}$	0.00
18	-0.003086	-1	$6.85 \times 10^{-12}$	$1.097 \times 10^{-13}$	0.00

TABLE II. Verification metrics across mesh sizes. For each L, we report the coupling  $g \equiv u/L^2$ , the maximum Richardson residual, and the EBV and sum-rule defects; all runs meet the tolerances  $\max_i |\text{EBV}_i| \le 10^{-12}$  and  $\left|\sum_i v_i + 2M\right| \le 10^{-14}$ .

Eq. (B109) is satisfied at these roots and  $\sum_{\alpha} E_{\alpha}$  is real. Let  $N_i = b_i^{\dagger} b_i$  be the pair number operator at level i. In seniority zero the diagonal pair-pair correlator is

$$C_{ii} \equiv \langle b_i^{\dagger} b_i \rangle = \langle N_i \rangle \in [0, 1].$$
 (B117)

Using Hellmann-Feynman together with the Richardson-Gaudin algebra we obtain, in terms of the scaled variables  $v_i$ ,

$$\langle N_i \rangle = \frac{1}{2} \left( -1 - v_i + g \,\partial_g v_i \right), \tag{B118}$$

which is numerically stable and exactly number-conserving:

$$\sum_{i=1}^{\Omega} \langle N_i \rangle = M. \tag{B119}$$

These  $C_{ii}$  constitute the ground-truth pair-pair correlators for our model training. For each mesh size L we report the target coupling g used in the run and the maximum residual from Eq. (B109),  $\max_{\alpha} |R_{\alpha}| \equiv \max_{\alpha} \left| 1 + \frac{g}{2} \sum_{i=1}^{\Omega} \frac{1}{\varepsilon_i - E_{\alpha}} - g \sum_{\beta \neq \alpha} \frac{1}{E_{\beta} - E_{\alpha}} \right|$ . We also monitor the eigenvalue-based residuals from Eq. (B114),  $\max_{i} |\text{EBV}_{i}| \equiv \max_{i} \left| v_i^2 + 2v_i - g \sum_{k \neq i} \frac{v_i - v_k}{\varepsilon_i - \varepsilon_k} \right|$  and the sum-rule defect  $\left| \sum_{i} v_i + 2M \right|$  from Eq. (B115). (see Fig. 7 for visualization)

#### e. Exact-Diagonalization (ED) Validation

To validate the Richardson solutions, we diagonalize the Richardson Hamiltonian in the seniority-zero sector, and compare with our numerical results. For L=2, g=-0.25, the ED eigenvalue  $E_{\rm ED}$  matches exactly Richardson root solving Eq. (B109); the residual is  $\max_{\alpha} |R_{\alpha}| = 4.44 \times 10^{-16}$ , and the ED-implied  $g\Lambda_i = g/(\varepsilon_i - E)$  matches the EBV solution to machine precision. For L=4, g=-1/16, the two rapidities satisfy  $\sum_{\alpha} E_{\alpha} = E_{\rm ED}^{\rm (gs)}$  with

$$\Delta = \sum_{\alpha} E_{\alpha} - E_{\rm ED}^{\rm (gs)} = -1.33 \times 10^{-15}$$

and  $\max_{\alpha} |R_{\alpha}| = 2.10 \times 10^{-14}$ . It confirms that our numerical solver tracks the correct ground-state branch and that the reported pair-pair correlators are exact.

#### 2. ML Results

We wish to train a NN on the pair-pair correlation function  $C \in \mathbb{R}^{L^2 \times L^2}$ , which has  $L^4$  elements in total. Since the self-attention mechanism has quadratic time and space complexity, the memory requirements are proportional to  $L^8$ , which can be extremely difficult for large L. Therefore, we chose to focus exclusively on the SIREN architecture

Hyperparameter	Trained on $L=6$	Trained on $L = 10$		
Total Epochs	100	100		
$d_H$	280	722		
L'	18	16		
ζ	linear	linear		
${\cal P}$	$\mathcal{P}_{ ext{L}1}$	$\mathcal{P}_{ ext{L1}}$		
λ	$1 \times 10^{-4}$	$1 \times 10^{-4}$		

TABLE III. List of hyperparameters used for training a SIREN on L=6 or L=10 for the Richardson model. "Total Epochs" is the total number of training iterations that the SIREN was allowed to be trained for.  $d_H$  is the hidden size and L' is the size of the finer mesh that we downsample from as defined in Sec. A 2 c.  $\zeta$  is the downsampling method,  $\mathcal{P}$  is the chosen prior, and  $\lambda$  is a regularization coefficient, as defined in Sec. A 2 c.

for this model. Sec. A 2 b contains a discussion on how to construct 2D normalized coordinates for the input to the SIREN. We now show how we construct four-dimensional normalized coordinates for the Richardson model in a similar approach. We store the correlator as a rank-4 tensor

$$C_{ijk\ell} \equiv C_{\mathbf{k}(i,j),\mathbf{k}(k,\ell)}, \qquad C \in \mathbb{R}^{L \times L \times L \times L}.$$
 (B120)

where  $\mathbf{k}(i,j) \equiv \frac{i}{L} \mathbf{b}_1 + \frac{j}{L} \mathbf{b}_2$ ,  $i,j \in \{0,\ldots,L-1\}$  from Eq. (A2). To encode periodicity explicitly, define the wrap map

$$\pi_L : \{0, \dots, L\} \to \{0, \dots, L-1\}, \qquad \pi_L(m) \equiv m \bmod L,$$
 (B121)

and form the grid of size  $(L+1)^4$ 

$$\widetilde{C}_{mnpq} = C_{\pi_L(m) \, \pi_L(n) \, \pi_L(p) \, \pi_L(q)}, \qquad m, n, p, q \in \{0, \dots, L\}.$$
 (B122)

Following Eq. (A46), normalize indices to [-1,1] with  $\phi_L(m) = 2m/L - 1$  and define the NN input coordinates

$$\mathbf{v}(m, n, p, q) = (\phi_L(m), \phi_L(n), \phi_L(p), \phi_L(q)) \in [-1, 1]^4, \tag{B123}$$

so training pairs are  $(v(m, n, p, q), \widetilde{C}_{mnpq})$ . Finally, the physical tensor is recovered by:

$$C_{ijk\ell} = \widetilde{C}_{ijk\ell}, \qquad i, j, k, \ell \in \{0, \dots, L-1\}.$$
(B124)

Our task is thus reduced to learning a mapping (parameterized by a SIREN) from the space of 4D coordinates in  $[-1,1]^4$  to their corresponding values in  $\widetilde{C}$  (from which we can determine C via Eq. (B124)). We use the same NN architecture and training scheme as described in Sec. A 2. In the loss function, we average the SIREN predictions for large L with all of their rotations and reflections (i.e. the entire group  $D_4$  of symmetries of the square) before downsampling back down to the training system size. For the Richardson model, in addition to the FH and TV priors defined in Eq. (A58) for the general SIREN architecture, we also allow for an additional prior which consists of the  $\ell^1$  norm on the values the SIREN takes at a randomly sampled set of points. It is defined by:

$$\mathcal{P}_{L1}(\theta) = \frac{1}{N} \sum_{i=1}^{N} \|\Phi_{\theta}(u_i)\|_{1}, \tag{B125}$$

where  $\{u_i\}_{i=1}^N \subset [-1,1]^4$  is a randomly sampled set of N points in the domain,  $\Phi_{\theta}$  is the SIREN with learnable parameters  $\theta$ , and  $\|\cdot\|_1$  denotes the  $\ell^1$  norm. Finally, we use the Tree-Structured Parzen Estimation (TPE) [119] algorithm to search for the optimal hyperparameter configuration that can enable the SIREN to generalize effectively to larger L, as intended. A list of the hyperparameters used can be seen in Tab. III.

We trained two SIRENs on  $\widetilde{C}$ , and evaluated their performance on C. One SIREN was trained on L=6 and tested on  $L=8,10,\ldots 18$ , and the other was trained on L=10 and tested on L=12,14,16,18. For the Richardson model, the mean squared error (MSE) between the SIREN-predicted final C and the true final C is defined as:

$$MSE(C, C^{SIREN}) = \frac{1}{L^4} \sum_{i=1}^{L} \sum_{j=1}^{L} \sum_{k=1}^{L} \sum_{\ell=1}^{L} \left( C_{ijk\ell}^{SIREN} - C_{ijk\ell} \right)^2,$$
(B126)

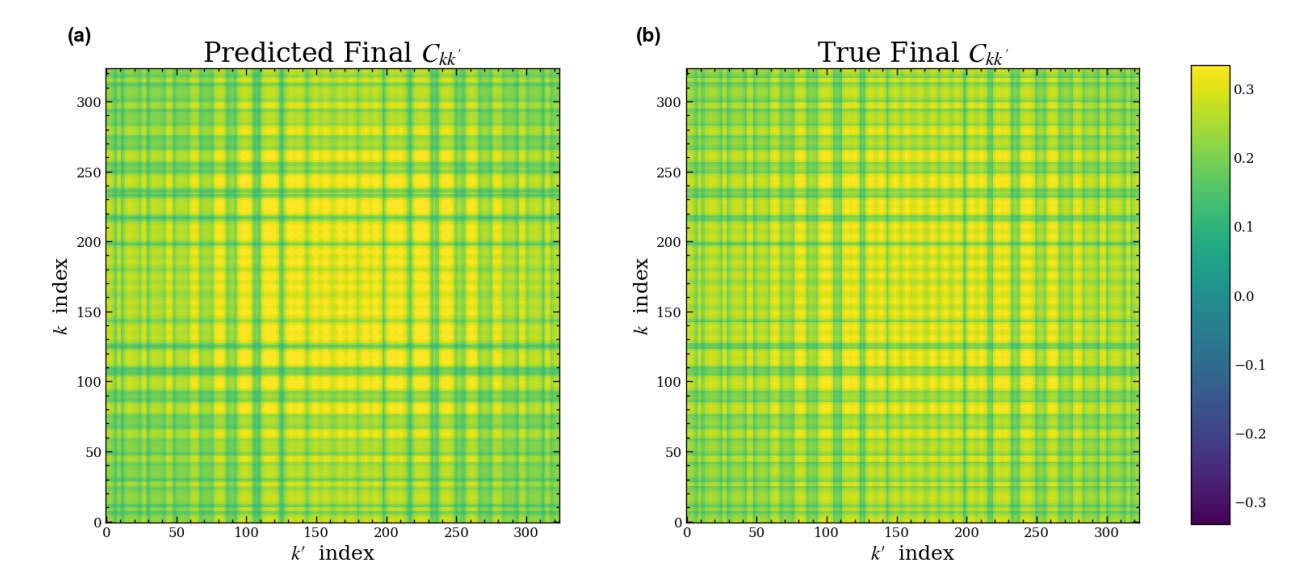


FIG. 8. Comparison between (a) the predicted final L=18  $C_{kk'}$  given by a SIREN trained on L=10 and (b) the true final  $C_{kk'}$  for L=18. Indices  $k,k'\in\{0,\ldots,L^2-1\}$  enumerate the  $L\times L$  k-points by flattening  $(\ell_1,\ell_2)$  with  $\ell_{1,2}\in\{0,\ldots,L-1\}$  via  $k=\ell_1+L$   $\ell_2$  with its momentum vector in Eq. (A2), and similarly for k'.

where  $C^{\text{SIREN}}$  is the matrix of pair-pair correlators predicted by the SIREN. In order to evaluate the trained SIREN's performance, we take the square root of Eq. (B126), i.e.  $\sqrt{\text{MSE}}$ , in order to ensure that the power on the unit of the error is the same as that for C and  $C^{\text{SIREN}}$ . To measure the relative accuracy  $r_n$ , we consider the  $\sqrt{\text{MSE}}$  as a fraction of the total range of values of the original C, as seen in Eq. (21). Results are shown in Tab. I. We can also compare the predicted final 2-RDM from the SIREN to the true final 2-RDM (i.e. the actual values of C) visually, as shown in Fig. 8 for the SIREN trained on L=10. (See Fig. 4 in the maintext for a comparison with the SIREN trained on L=6.)

#### Appendix C: Translation-invariant 1-RDM in a four-band model

#### 1. Model Set-Up

We work on an  $L \times L$  Bravis lattice with a four-component orbital (or layer/sublattice) spinor  $\psi_{\mathbf{r}} = (\psi_{\mathbf{r},1}, \dots, \psi_{\mathbf{r},4})^{\mathsf{T}}$  at site  $\mathbf{r} \in \mathbb{Z}^2$ . The real-space single-particle Hamiltonian contains on-site and short-range hoppings written with  $4 \times 4$  matrices  $h(\boldsymbol{\delta})$  that connect  $\mathbf{r}$  to  $\mathbf{r} + \boldsymbol{\delta}$ :

$$H_0 = \sum_{\mathbf{r}} \psi_{\mathbf{r}}^{\dagger} h(\mathbf{0}) \psi_{\mathbf{r}} + \sum_{\mathbf{r}} \sum_{\delta \neq \mathbf{0}} \left( \psi_{\mathbf{r}+\delta}^{\dagger} h(\delta) \psi_{\mathbf{r}} + \text{h.c.} \right).$$
 (C1)

We choose the five gamma matrices as

$$\Gamma_1 = \sigma_x \otimes \sigma_x, \quad \Gamma_2 = \sigma_x \otimes \sigma_y, \quad \Gamma_3 = \sigma_x \otimes \sigma_z, \quad \Gamma_4 = \sigma_y \otimes \mathbb{I}, \quad \Gamma_5 = \sigma_z \otimes \mathbb{I},$$
 (C2)

where  $\sigma_x$ ,  $\sigma_y$  and  $\sigma_z$  are Pauli matrices. The hoppings have the following form:

on-site:  $h(\mathbf{0}) = \Gamma_5$ , NN (odd, along x, y):  $h(+\hat{x}) = \frac{1}{2i}\Gamma_1$ ,  $h(-\hat{x}) = -\frac{1}{2i}\Gamma_1$ ,  $h(+\hat{y}) = \frac{1}{2i}\Gamma_2$ ,  $h(-\hat{y}) = -\frac{1}{2i}\Gamma_2$ , NNN(odd, along x, y):  $h(+2\hat{x}) = \frac{1}{2i}\Gamma_3$ ,  $h(-2\hat{x}) = -\frac{1}{2i}\Gamma_3$ ,  $h(+2\hat{y}) = \frac{1}{2i}\Gamma_4$ ,  $h(-2\hat{y}) = -\frac{1}{2i}\Gamma_4$ , (C3) NN (even, in the  $\Gamma_5$  channel):  $h(\pm \hat{x}) = \frac{1}{2}\Gamma_5$ ,  $h(\pm \hat{y}) = \frac{1}{2}\Gamma_5$ .

Here "NN" denotes nearest–neighbor displacements  $\boldsymbol{\delta}$  with  $|\boldsymbol{\delta}|=1$  ( $\pm\hat{\boldsymbol{x}},\pm\hat{\boldsymbol{y}}$ ); "NNN" denotes next–nearest neighbors along the axes  $|\boldsymbol{\delta}|=2$  ( $\pm2\hat{\boldsymbol{x}},\pm2\hat{\boldsymbol{y}}$ ). Unlisted  $h(\boldsymbol{\delta})$  are zero. With the lattice Fourier transform

$$\psi_{\mathbf{r}} = \frac{1}{\sqrt{L^2}} \sum_{\mathbf{k}} e^{i\mathbf{k}\cdot\mathbf{r}} \psi_{\mathbf{k}}, \qquad \mathbf{k} = (k_x, k_y) \in [0, 2\pi)^2,$$
(C4)

Eq. (C1) becomes

$$H_{0} = \sum_{\mathbf{r}} \psi_{\mathbf{r}}^{\dagger} h(\mathbf{0}) \psi_{\mathbf{r}} + \sum_{\mathbf{r}} \sum_{\delta \neq \mathbf{0}} \left( \psi_{\mathbf{r}+\delta}^{\dagger} h(\delta) \psi_{\mathbf{r}} + \text{h.c.} \right)$$

$$= \frac{1}{L^{2}} \sum_{\mathbf{r}} \sum_{\mathbf{k}, \mathbf{k}'} e^{-i\mathbf{k}' \cdot \mathbf{r}} \psi_{\mathbf{k}'}^{\dagger} h(\mathbf{0}) e^{i\mathbf{k} \cdot \mathbf{r}} \psi_{\mathbf{k}} + \frac{1}{L^{2}} \sum_{\mathbf{r}} \sum_{\delta \neq \mathbf{0}} \sum_{\mathbf{k}, \mathbf{k}'} e^{-i\mathbf{k}' \cdot (\mathbf{r}+\delta)} \psi_{\mathbf{k}'}^{\dagger} h(\delta) e^{i\mathbf{k} \cdot \mathbf{r}} \psi_{\mathbf{k}} + \text{h.c.}$$

$$= \sum_{\mathbf{k}, \mathbf{k}'} \psi_{\mathbf{k}'}^{\dagger} h(\mathbf{0}) \psi_{\mathbf{k}} \frac{1}{L^{2}} \sum_{\mathbf{r}} e^{i(\mathbf{k}-\mathbf{k}') \cdot \mathbf{r}} + \sum_{\delta \neq \mathbf{0}} \sum_{\mathbf{k}, \mathbf{k}'} \psi_{\mathbf{k}'}^{\dagger} h(\delta) \psi_{\mathbf{k}} \frac{1}{L^{2}} \sum_{\mathbf{r}} e^{i(\mathbf{k}-\mathbf{k}') \cdot \mathbf{r}} e^{-i\mathbf{k}' \cdot \delta} + \text{h.c.}$$

$$= \sum_{\mathbf{k}} \psi_{\mathbf{k}}^{\dagger} h(\mathbf{0}) \psi_{\mathbf{k}} + \sum_{\delta \neq \mathbf{0}} \sum_{\mathbf{k}} \psi_{\mathbf{k}}^{\dagger} \left( e^{i\mathbf{k} \cdot \delta} h(\delta) \right) \psi_{\mathbf{k}} + \text{h.c.} \qquad \left( \frac{1}{L^{2}} \sum_{\mathbf{r}} e^{i(\mathbf{k}-\mathbf{k}') \cdot \mathbf{r}} = \delta_{\mathbf{k}, \mathbf{k}'} \right)$$

$$= \sum_{\mathbf{k}} \psi_{\mathbf{k}}^{\dagger} \left[ h(\mathbf{0}) + \sum_{\delta \neq \mathbf{0}} \left( e^{i\mathbf{k} \cdot \delta} h(\delta) + e^{-i\mathbf{k} \cdot \delta} h^{\dagger}(\delta) \right) \right] \psi_{\mathbf{k}}$$

$$\equiv \sum_{\mathbf{k}} \psi_{\mathbf{k}}^{\dagger} H_{\mathbf{0}}(\mathbf{k}) \psi_{\mathbf{k}}, \qquad H_{\mathbf{0}}(\mathbf{k}) = h(\mathbf{0}) + \sum_{\delta \neq \mathbf{0}} \left( e^{i\mathbf{k} \cdot \delta} h(\delta) + e^{-i\mathbf{k} \cdot \delta} h^{\dagger}(\delta) \right) = \sum_{a=1}^{5} d_{a}(\mathbf{k}) \Gamma_{a},$$
(C5)

and the form factors are

$$d_1 = \sin k_x$$
,  $d_2 = \sin k_y$ ,  $d_3 = \sin(2k_x)$ ,  $d_4 = \sin(2k_y)$ ,  $d_5 = 1 + \cos k_x + \cos k_y$ . (C6)

The odd/even harmonics follow from  $e^{\pm i \mathbf{k} \cdot \mathbf{\delta}} = (\cos \mathbf{k} \cdot \mathbf{\delta}) \pm i (\sin \mathbf{k} \cdot \mathbf{\delta})$ : antisymmetric pairs  $h(+\delta) = -h(-\delta)$  generate sin, while symmetric pairs  $h(+\delta) = h(-\delta)$  generate cos. By the Clifford algebra of the  $\Gamma_a$ , the spectrum is doubly degenerate with

$$E_{\pm}(\mathbf{k}) = \pm ||d(\mathbf{k})|| = \pm \sqrt{\sum_{a=1}^{5} d_a(\mathbf{k})^2}.$$
 (C7)

At filling f=1 we occupy the lower two bands. We diagnose its topology via the Wilson loop  $W_x(k_y)$  of the occupied projector  $P(\mathbf{k})$  in Eq. (C14), yielding the  $\mathbb{Z}_2$  index

$$\nu_{\mathbb{Z}_2} = 1. \tag{C8}$$

This certifies that our training/benchmark data come from a  $\mathbb{Z}_2$  non-trivial phase. For the interaction in second quantization and its lattice Fourier transform Eq. (B2),

$$H_{\text{int}} = \frac{1}{2} \sum_{\mathbf{r}} \sum_{\mathbf{R}} V(\mathbf{R}) \, n_{\mathbf{r}} \, n_{\mathbf{r}+\mathbf{R}}$$

$$= \frac{1}{2} \sum_{\mathbf{r},\mathbf{R}} V(\mathbf{R}) \left( \frac{1}{\sqrt{N}} \sum_{\mathbf{k}} e^{i\mathbf{k}\cdot\mathbf{r}} \, \psi_{\mathbf{k}}^{\dagger} \right) \left( \frac{1}{\sqrt{N}} \sum_{\mathbf{k'}} e^{-i\mathbf{k'}\cdot\mathbf{r}} \, \psi_{\mathbf{k'}} \right) \left( \frac{1}{\sqrt{N}} \sum_{\mathbf{p}} e^{i\mathbf{p}\cdot(\mathbf{r}+\mathbf{R})} \, \psi_{\mathbf{p}}^{\dagger} \right) \left( \frac{1}{\sqrt{N}} \sum_{\mathbf{p'}} e^{-i\mathbf{p'}\cdot(\mathbf{r}+\mathbf{R})} \, \psi_{\mathbf{p'}} \right)$$

$$= \frac{1}{2N^{2}} \sum_{\mathbf{R}} V(\mathbf{R}) \sum_{\mathbf{k},\mathbf{k'},\mathbf{p},\mathbf{p'}} \left( \sum_{\mathbf{r}} e^{i(\mathbf{k}-\mathbf{k'}+\mathbf{p}-\mathbf{p'})\cdot\mathbf{r}} \right) e^{i(\mathbf{p}-\mathbf{p'})\cdot\mathbf{R}} \, \psi_{\mathbf{k}}^{\dagger} \psi_{\mathbf{k'}} \psi_{\mathbf{p}}^{\dagger} \psi_{\mathbf{p'}}$$

$$= \frac{1}{2N} \sum_{\mathbf{R}} V(\mathbf{R}) \sum_{\mathbf{k},\mathbf{k'},\mathbf{q}} e^{-i\mathbf{q}\cdot\mathbf{R}} \, \psi_{\mathbf{k}+\mathbf{q}}^{\dagger} \psi_{\mathbf{k}} \, \psi_{\mathbf{k'}-\mathbf{q}}^{\dagger} \psi_{\mathbf{k'}} \qquad (\mathbf{q} \equiv \mathbf{p'} - \mathbf{p})$$

$$= \frac{1}{2N} \sum_{\mathbf{q}} \left( \sum_{\mathbf{R}} V(\mathbf{R}) e^{-i\mathbf{q}\cdot\mathbf{R}} \right) \sum_{\mathbf{k},\mathbf{k'}} \psi_{\mathbf{k}+\mathbf{q}}^{\dagger} \psi_{\mathbf{k}} \, \psi_{\mathbf{k'}-\mathbf{q}}^{\dagger} \psi_{\mathbf{k'}}. \tag{C9}$$

Thus the translation-invariant interaction enters through the lattice Fourier transform,

$$U(q) = \sum_{\mathbf{R}} V(\mathbf{R}) e^{-iq \cdot \mathbf{R}}.$$
 (C10)

For our specific short-range choice

$$V(\mathbf{R}) = U_0 \left[ \delta_{\mathbf{R},\mathbf{0}} + \frac{1}{2} \left( \delta_{\mathbf{R},\hat{\mathbf{x}}} + \delta_{\mathbf{R},-\hat{\mathbf{x}}} + \delta_{\mathbf{R},\hat{\mathbf{y}}} + \delta_{\mathbf{R},-\hat{\mathbf{y}}} \right) \right]$$
(C11)

Therefore,

$$U(\mathbf{q}) = \sum_{\mathbf{R}} V(\mathbf{R}) e^{-i\mathbf{q}\cdot\mathbf{R}} = U_0 \left[ 1 + \frac{1}{2} \left( e^{-iq_x} + e^{+iq_x} + e^{-iq_y} + e^{+iq_y} \right) \right] = U_0 \left( 1 + \cos q_x + \cos q_y \right).$$
 (C12)

So the momentum-space interaction is

$$H_{\text{int}} = \frac{1}{2N} \sum_{\mathbf{q}} U_0 \left( 1 + \cos q_x + \cos q_y \right) \sum_{\mathbf{k}, \mathbf{k}'} \psi_{\mathbf{k}+\mathbf{q}}^{\dagger} \psi_{\mathbf{k}} \psi_{\mathbf{k}'-\mathbf{q}}^{\dagger} \psi_{\mathbf{k}'}. \tag{C13}$$

The mean-field order parameter is the 1-RDM (projector onto occupied HF bands) at each momentum:

$$P(\mathbf{k}) = \sum_{n=1}^{f} |u_n(\mathbf{k})\rangle \langle u_n(\mathbf{k})|, \tag{C14}$$

where n is the band index, and  $f \in \{1, 2, 3, 4\}$  is the filling (number of occupied bands per k). We choose f = 1 for our ML training. The projector obeys

$$P^{\dagger}(\mathbf{k}) = P(\mathbf{k}), \qquad P^{2}(\mathbf{k}) = P(\mathbf{k}), \qquad \operatorname{tr} P(\mathbf{k}) = f.$$
 (C15)

Normal ordering the interaction with respect to P(k) yields the self-consistent HF Hamiltonian

$$H_{HF}(\mathbf{k}) = H_0(\mathbf{k}) + \Sigma_H + \Sigma_F(\mathbf{k}; [P]), \tag{C16}$$

with a Hartree shift

$$\Sigma_H = U(0)\,\bar{n}\mathbb{I}_4, \quad \bar{n} \equiv \frac{1}{L^2} \sum_{\mathbf{k}} \operatorname{tr} P(\mathbf{k}),$$
 (C17)

and a Fock self-energy given by a BZ convolution

$$\Sigma_F(\mathbf{k}; [P]) = -\frac{1}{L^2} \sum_{\mathbf{q}} U(\mathbf{q}) P(\mathbf{k} + \mathbf{q}).$$
 (C18)

Because  $\Sigma_H \propto \mathbb{I}_4$  and  $\operatorname{tr} P(\mathbf{k}) = f$  is fixed by the filling, the Hartree term produces a uniform band shift and does not affect the projector; symmetry breaking (if any) is controlled by  $\Sigma_F$ . We monitor the total energy density (per unit cell)

$$\mathcal{E}[P] = \frac{1}{2L^2} \sum_{\mathbf{k}} \operatorname{tr} \left[ \left( H_{HF}(\mathbf{k}) + H_0(\mathbf{k}) \right) P(\mathbf{k}) \right], \tag{C19}$$

where the factor 1/2 avoids double counting. A typical stopping criterion is  $|\mathcal{E}_{n+1} - \mathcal{E}_n| < 10^{-6}$ , supplemented by the mean-squared change of the projector between iterations. Arrays  $H_0(\mathbf{k})$ ,  $U(\mathbf{q})$ , and  $P(\mathbf{k})$  live on the BZ grid. Given  $P^{(n)}$ , we build  $\Sigma_H[P^{(n)}]$  and  $\Sigma_F[P^{(n)}]$ , diagonalize  $H_{\rm HF}[P^{(n)}](\mathbf{k})$  at each  $\mathbf{k}$ , and update

$$P^{(n+1)}(\mathbf{k}) = \sum_{m=1}^{f} |u_m^{(n)}(\mathbf{k})\rangle\langle u_m^{(n)}(\mathbf{k})|,$$
 (C20)

selecting the f eigenvectors with the lowest eigenvalues (ordered by real part). The loop terminates when the energy criterion above is satisfied.

The four-band model supplies the final HF labels — P(k) at filling f=1 and band energies  $\mathcal{E}$  — from a translation-invariant HF calculation, by which we pretrain and validate our NN architectures. It provides a clean benchmark to quantify acceleration: we compare HF iteration counts when initialized with the NN-predicted final 1-RDM versus a random initial 1-RDM at a fixed tolerance.

#### ML Results

Translation-invariant systems are simpler because the one-body correlator is diagonal in momentum  $(\mathbf{k} = \mathbf{k}')$ , so inference reduces to a sequence of  $L^2$  matrices. The lower dimensionality lets us use a conventional self-attention NN without neural representation (SIREN). We again work on the discrete BZ with k in Eq. (A2). Index grid points by their integers  $(l_1, l_2)$  with  $l_{1,2} \in \{0, \dots, L-1\}$ , so that

$$m{k}(l_1, l_2) = rac{l_1}{L} \, m{b}_1 + rac{l_2}{L} \, m{b}_2.$$

To encode relative position with periodic boundary conditions, use the wrapped (minimum-image) index differences

$$\Delta l_1 = ((l_1 - l_1' + \lfloor L/2 \rfloor) \bmod L) - \lfloor L/2 \rfloor, \quad \Delta l_2 = ((l_2 - l_2' + \lfloor L/2 \rfloor) \bmod L) - \lfloor L/2 \rfloor, \tag{C21}$$

so we can define the 2D coordinate

$$x_{(l_1,l_2),(l'_1,l'_2)} = \left(\frac{\Delta l_1}{L}, \frac{\Delta l_2}{L}\right).$$
 (C22)

For brievity we denote  $x_{(l_1,l_2),(l'_1,l'_2)}$  as  $x_{ij}$ . For the four-band model we keep the architecture of Sec. A 1 but, given the simplicity here, replace the custom Fourier-based bias by a small MLP, following the formulation of Ref. [120]. That is,

$$B_{ij} = f_{\theta}(\mathbf{k}_i, \mathbf{k}_j) = \text{GELU}(\mathbf{x}_{ij}W_1 + \mathbf{b}_1)W_2 + b_2. \tag{C23}$$

where  $x_{ij}$  represents the relative coordinate between two k-points in 2D momentum space and  $W_1 \in \mathcal{M}_{2 \times d_{\text{MLP}}}(\mathbb{R})$ ,  $\boldsymbol{b}_1 \in \mathbb{R}^{d_{\text{MLP}}}, W_2 \in \mathcal{M}_{d_{\text{MLP}} \times 1}(\mathbb{R}), \boldsymbol{b}_2 \in \mathbb{R}$  are all filled with learnable parameters to be optimized during training, and  $d_{\text{MLP}}$  represents the size of the hidden layer in the MLP. Eq. (C23) replaces Eq. (A27) for the bias function in the four-band model. Thus, the output of  $f_{\theta}$  is a scalar bias (that quantifies how closely related the corresponding k-points are), which is then added to the self-attention computation via Eq. (A30), thereby injecting relative positional information into the NN.

#### Hyperparameters

To train the self-attention NN, we used a constant learning rate of  $3 \times 10^{-4}$ . A full list of the hyperparameters used can be seen in Tab. IV.

Hyperparameter	Value
Epochs	300
N	3
$N_{ m head}$	2
D	32
$D_{ m ff}$	256
$d_{\mathrm{MLP}}$	32
p	0.0

TABLE IV. List of hyperparameters for training a self-attention NN on the four-band model. "Epochs" is the number of training iterations. N is the number of attention layers in the NN and D is the dimensionality (i.e. the "model width") as defined in Sec. A1c. N<sub>head</sub> is the number of attention heads in a single attention block, as defined in Sec. A1d. D<sub>ff</sub> is the size of the hidden layer in the FFN, as defined in Sec. A1e. p is the probability with which elements are set to 0 in the Dropout operation, according to Eq. (A37).

#### b. Standardization

For the translation-invariant case, given  $O_{\mathbf{k},\alpha\alpha'}^{\mathbf{q}=0}$  we construct  $X_{\mathrm{init}}$  and  $X_{\mathrm{tgt}}$  as in Eq. (A11) and Eq. (A5). To standardize the data, we compute the mean and standard deviations across all features  $f \in \{1, \dots 2\xi^2\}$ . That is, for

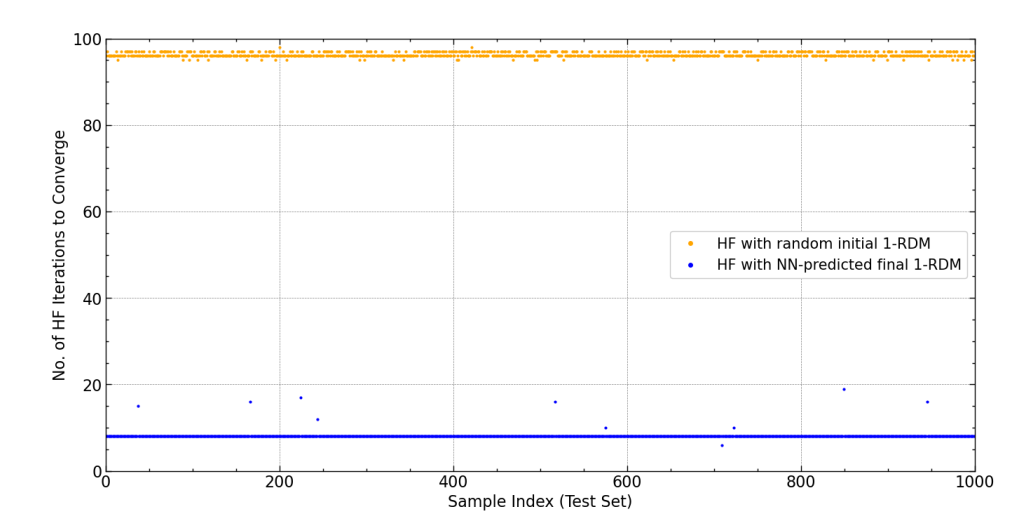


FIG. 9. HF iteration test on translationally-invariant four-band model (see Eqs. (C1) to (C20)) for L = 50 using a self-attention NN trained only on L = 6 and L = 8. The x-axis enumerates the 1000 test samples; the y-axis shows the number of HF iterations required to reach the convergence criterion when using the predicted final 1-RDM from the NN as the initial 1-RDM (blue) and when using a random initial 1-RDM (orange).

all  $N_{\text{sample}}$  training samples with  $\beta \in \{\text{init}, \text{tgt}\}$ :

$$\mu_f^{(\beta)} \equiv \frac{1}{N_{\text{sample}} L^2\left(2\xi^2\right)} \sum_{\text{sample}} \sum_{i=1}^{L^2} \sum_{f=1}^{2\xi^2} X_{i,f}^{(\beta)}, \qquad \left(\sigma_f^{(\beta)}\right)^2 \equiv \frac{1}{N_{\text{sample}} L^2\left(2\xi^2\right) - 1} \sum_{\text{sample}} \sum_{i=1}^{L^2} \sum_{f=1}^{2\xi^2} \left(X_{i,f}^{(\beta)} - \mu_f^{(\beta)}\right)^2. \quad (C24)$$

Eq. (C24) replaces Eq. (A10) for computing  $\mu_f^{(\beta)}$  and  $\sigma_f^{(\beta)}$  in the four-band model. We then use these values to standardize  $X_{\rm init}$  and  $X_{\rm tgt}$  following Eq. (A11).

#### c. Weight Initialization

The initial values for all NN parameters were drawn from the default distributions in PyTorch's initialization scheme. Specifically, we use Kaiming (He) [121] initialization for all weight matrices and bias vectors in the input and output layers (i.e.  $W_{\rm in}$ ,  $b_{\rm in}$  and  $W_{\rm out}$ ,  $b_{\rm out}$ ) as well as in the FFNs (see Eq. (A43)) and the MLPs for  $f_{\theta}$  (from Eq. (C23)), and in the self-attention mechanism (i.e.  $W_Q^{(h)}$ ,  $W_K^{(h)}$ ,  $W_V^{(h)}$ ,  $W_O$ ). Unlike the general case in Eq. (A36), we do not use a learnable bias vector  $b_O$  when mixing information across attention heads. For the LayerNorm operation (see Eq. (A40)), the weights  $\gamma$  and the biases  $\beta$  are initialized to all 1's and all 0's, respectively. Finally, we choose the learnable scalar s in Eq. (A30) in each attention head to be initialized to 1. All learnable parameters are trained by backpropagation to minimize the loss.

#### d. Results

We train a self-attention model on 10,000 (input,label) 1-RDM pairs at L=6 and L=8, and evaluate on 1,000 held-out systems with  $L \in \{10, 12, \dots, 50\}$ . For each test instance we run two HF solvers with identical tolerance and settings: (i) initialized from a random 1-RDM, and (ii) initialized from the NN-predicted final 1-RDM. We report the percent reduction in iteration count. At L=50 the mean reduction is 91.63%. Results for all L are in Fig. 9 and Tab. V.

In order to test how well the NN generalizes to larger system sizes, we also computed the MSE loss between the predicted final 1-RDM from the NN and the true final 1-RDM for up to L=50, where the MSE is defined as in Eq. (A21). The results can be seen in Fig. 10.

$oldsymbol{L}$	Original	with NN	% Reduction
10	97.62	5.63	94.24
12	96.31	7.00	92.73
14	96.58	7.00	92.75
16	96.29	7.00	92.73
18	96.31	7.35	92.36
20	96.32	7.96	91.74
22	96.28	8.00	91.69
24	96.27	8.00	91.69
26	96.23	8.00	91.69
28	96.29	8.00	91.69
30	96.28	7.94	91.75
32	96.28	8.00	91.70
34	96.24	8.00	91.69
36	96.27	8.00	91.69
38	96.27	8.00	91.69
40	96.24	8.02	91.67
42	96.25	8.00	91.69
44	96.23	8.08	91.61
46	96.24	8.04	91.64
48	96.24	8.04	91.64
50	96.30	8.06	91.63

TABLE V. Table showing results for the translationally-invariant HF calculation as described in Eqs. (C1) to (C20), using a self-attention NN trained on L=6 and L=8 and evaluated on  $L=10,12,\ldots 50$ . Here, "Original" refers to the average number of HF iterations with a random initial 1-RDM, while "with NN" refers to the average number of iterations when using the predicted final 1-RDM from the NN as the initial 1-RDM for HF. "% Reduction" refers to the percent difference between the two quantities.

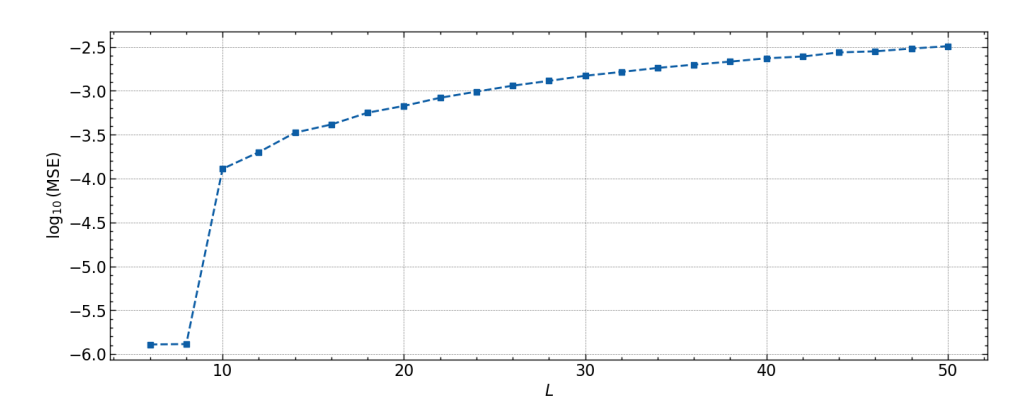


FIG. 10. Generalization test for the translationally-invariant HF calculation (see Eqs. (C1) to (C20)) using a self-attention NN trained only on L=6 and L=8, showing the MSE loss (defined in Eq. (A21)) as a function of the system size L.

#### Appendix D: Square-lattice Hubbard model

# 1. Model Set-Up

We study the spinful Hubbard model on a 2D square lattice [97, 98] with size  $N \equiv L \times L$ . In real space,

$$H = -t \sum_{\langle \boldsymbol{r}, \boldsymbol{r}' \rangle, \sigma} \left( c_{\boldsymbol{r}\sigma}^{\dagger} c_{\boldsymbol{r}'\sigma} + \text{h.c.} \right) + U \sum_{\boldsymbol{r}} n_{\boldsymbol{r}\uparrow} n_{\boldsymbol{r}\downarrow}, \tag{D1}$$

with  $c_{r\sigma}$  the annihilation operator at site r and spin  $\sigma \in \{\uparrow, \downarrow\}$ , and  $n_{r\sigma} = c^{\dagger}_{r\sigma} c_{r\sigma}$ . With the lattice Fourier transform

$$c_{\boldsymbol{r}\sigma} = \frac{1}{\sqrt{L^2}} \sum_{\boldsymbol{k}} e^{i\boldsymbol{k}\cdot\boldsymbol{r}} c_{\boldsymbol{k}\sigma}, \quad c_{\boldsymbol{k}\sigma} = \frac{1}{\sqrt{L^2}} \sum_{\boldsymbol{r}} e^{-i\boldsymbol{k}\cdot\boldsymbol{r}} c_{\boldsymbol{r}\sigma}, \quad \boldsymbol{k} = (k_x, k_y) \in [0, 2\pi)^2.$$
 (D2)

The nearest-neighbor hopping  $\boldsymbol{\delta} \in \{\pm \hat{\boldsymbol{x}}, \pm \hat{\boldsymbol{y}}\}$  gives

$$H_0 = -t \sum_{\langle \boldsymbol{r}, \boldsymbol{r}' \rangle, \sigma} \left( c_{\boldsymbol{r}\sigma}^{\dagger} c_{\boldsymbol{r}'\sigma} + \text{h.c.} \right) = -t \sum_{\boldsymbol{r}, \sigma} \sum_{\boldsymbol{\delta} \in \{\pm \hat{\boldsymbol{x}}, \pm \hat{\boldsymbol{y}}\}} c_{\boldsymbol{r}\sigma}^{\dagger} c_{\boldsymbol{r}+\boldsymbol{\delta}, \sigma}$$
(D3)

$$= -\frac{t}{N} \sum_{\mathbf{r}, \sigma} \sum_{\boldsymbol{\delta}} \sum_{\mathbf{k}, \mathbf{k}'} e^{-i\mathbf{k}\cdot\mathbf{r}} c_{\mathbf{k}\sigma}^{\dagger} e^{i\mathbf{k}'\cdot(\mathbf{r}+\boldsymbol{\delta})} c_{\mathbf{k}'\sigma}$$
(D4)

$$= -t \sum_{\mathbf{k},\sigma} \left( \sum_{\delta} e^{i\mathbf{k}\cdot\delta} \right) c_{\mathbf{k}\sigma}^{\dagger} c_{\mathbf{k}\sigma} \qquad \left( \text{here} \quad \frac{1}{N} \sum_{\mathbf{r}} e^{i(\mathbf{k}'-\mathbf{k})\cdot\mathbf{r}} = \delta_{\mathbf{k},\mathbf{k}'} \right)$$
(D5)

$$\equiv \sum_{\mathbf{k},\sigma} \varepsilon(\mathbf{k}) c_{\mathbf{k}\sigma}^{\dagger} c_{\mathbf{k}\sigma}, \qquad \varepsilon(\mathbf{k}) = -t \sum_{\delta} e^{i\mathbf{k}\cdot\delta}$$
 (D6)

$$= -t(e^{ik_x} + e^{-ik_x} + e^{ik_y} + e^{-ik_y}) = -2t(\cos k_x + \cos k_y).$$
 (D7)

Choosing 2t = 1 yields

$$\varepsilon(k) = \cos k_x + \cos k_y,\tag{D8}$$

so the single-particle block reads

$$H_0(\mathbf{k}) = \varepsilon(\mathbf{k}) \mathbb{I}_2, \tag{D9}$$

with  $\mathbb{I}_2$  the identity in spin space. The on-site repulsion is local in r:

$$H_{\rm int} = U \sum_{\boldsymbol{r}} n_{\boldsymbol{r}\uparrow} n_{\boldsymbol{r}\downarrow} = \frac{U}{L^2} \sum_{\boldsymbol{k},\boldsymbol{k}',\boldsymbol{q}} c^{\dagger}_{\boldsymbol{k}+\boldsymbol{q},\uparrow} c_{\boldsymbol{k},\uparrow} c^{\dagger}_{\boldsymbol{k}'-\boldsymbol{q},\downarrow} c_{\boldsymbol{k}',\downarrow}.$$

The spin-resolved 1-RDM (occupied-band projector) in momentum space is

$$[O_{\sigma}]_{kk'} = \langle c^{\dagger}_{k'\sigma} c_{k\sigma} \rangle, \qquad \sigma \in \{\uparrow, \downarrow\}.$$
 (D10)

At temperature T=0 and for collinear states  $O_{\sigma}$  is a projector onto the occupied subspace,

$$O_{\sigma}^{\dagger} = O_{\sigma}, \qquad O_{\sigma}^{2} = O_{\sigma}, \qquad \text{Tr } O_{\sigma} = N_{\text{occ.}\sigma}.$$
 (D11)

We assume the spin U(1) symmetry is not spontaneously broken, i.e.,  $[O]_{\uparrow\downarrow} = [O]_{\downarrow\uparrow} = 0$ . We further assume spin fillings to be

$$N_{\text{occ},\uparrow} = N_{\text{occ},\downarrow} \equiv \frac{1}{2} N_{\text{occ}} \iff n_{\uparrow} = n_{\downarrow} = \frac{n}{2},$$
 (D12)

but we do not otherwise constrain translational symmetry a priori. To diagnose antiferromagnetism we monitor the (staggered) magnetization at a general wavevector Q,

$$m_{\mathbf{Q}} = \frac{1}{L^2} \sum_{\mathbf{r}} e^{i\mathbf{Q}\cdot\mathbf{r}} \left\langle n_{\mathbf{r}\uparrow} - n_{\mathbf{r}\downarrow} \right\rangle = \frac{1}{L^2} \sum_{\mathbf{k}} \left( [O_{\uparrow}]_{\mathbf{k},\mathbf{k}+\mathbf{Q}} - [O_{\downarrow}]_{\mathbf{k},\mathbf{k}+\mathbf{Q}} \right). \tag{D13}$$

With the collinear ansatz  $\langle c_{\mathbf{k}\uparrow}^{\dagger} c_{\mathbf{k}\downarrow} \rangle = 0$ , the on-site Hubbard interaction generates a uniform Hartree shift and a mixing between  $\mathbf{k}$  and  $\mathbf{k} + \mathbf{Q}$  mixing proportional to  $m_{\mathbf{Q}}$ .

At each iteration we diagonalize the and refill the  $N_{\text{occ},\sigma}$  lowest eigenstates to update 1-RDM.

This HF set-up provides true final 1-RDM labels (benchmarks to train and validate the ML model), and to quantify HF iteration savings at fixed discretization, filling, and U.

Hyperparameter	Value		
Epochs	3201		
N	3		
$N_{ m head}$	4		
D	64		
$D_{ m ff}$	128		
m	48		
p	0.1		

TABLE VI. List of hyperparameters for training a self-attention NN on the Hubbard model. "Epochs" is the number of training iterations. N is the number of attention layers in the NN and D is the dimensionality (i.e. the "model width") as defined in Sec. A1c.  $N_{\text{head}}$  is the number of attention heads in a single attention block and m is the total number of frequencies, as defined in Sec. A1d.  $D_{\text{ff}}$  is the size of the hidden layer in the FFN, as defined in Sec. A1e. p is the probability with which elements are set to 0 in the Dropout operation in Eq. (A37).

#### 2. ML Results

Despite spontaneous translation breaking, the order parameters of Hubbard model can be simplified to be similar enough to the translation-invariant case to use the same techniques according to Sec. A 1 a.

Label the  $L \times L$  BZ grid by integer coordinates Eq. (A46).

We investigated two approaches. Firstly, we trained a self-attention NN on the combined  $L^2$ -long sequence. Additionally, for this model we also trained SIRENs separately on the central diagonal and off-diagonal elements, and then combined the outputs to form the new 1-RDM. For both models, the training data was generated via HF calculations (for systems with small L) that had a convergence criterion of  $2 \times 10^{-5}$ . The trained model was then used to predict a density matrix for larger L which was subsequently used as the initial guess for the density matrix in the HF algorithm, using the same convergence criterion.

The self-attention NN was trained only for U=1 (due to limited data), while we also trained additional SIREN models for U=2 and U=3. In each case, the resultant reduction in the number of HF iterations required for convergence was noted, where the reduction is defined as the percent difference between the average number of HF iterations before and after using the NN outputs as the initial guess for the density matrix.

The training process for both NN architectures is detailed below.

# a. Self-Attention NN

For each k we transform 1-RDM into a real vector of length  $2\xi^2$  and standardize them as described in Sec. A 1 b and Sec. A 1 a

For the self-attention NN for the Hubbard model, we initialize  $W_{\rm in}$  and  $W_{\rm out}$  from a truncated normal distribution with  $\sigma=0.02$ . Kaiming (He) normal initialization [121] is used for the learnable weight matrices in the feedforward layers, while Xavier (Glorot) initialization [122] is used for each of the matrices  $W_Q^{(h)}$ ,  $W_K^{(h)}$ ,  $W_V^{(h)}$ ,  $W_Q^{(h)}$ , in the attention heads. The matrix of frequencies  $W_r$  from Eq. (A23) is initialized with values drawn from a standard normal distribution. Furthermore, the weights  $\gamma$  for the LayerNorm operation from Eq. (A40), the vector of coefficients C (Eq. (A26)), the power p (Eq. (A27)), and the learnable scalar s (Eq. (A30)) are each initialized to be 1. All bias vectors are set to 0 initially. After initialization, these learnable parameters are updated by backpropagation to minimize the loss, as indicated in Sec. A 1 c.

In order to train the NN, we used a custom learning rate schedule consisting of a linear warmup phase followed by cosine annealing (without restarts) [123], which is a well-established method for training self-attention models with adaptive optimizers. This learning rate cycle is repeated twice: initially, we train for 500 epochs, and then for 5000 epochs. Each time, the warmup phase lasts for 20 epochs followed by cosine decay for the rest of the cycle. Thus, we train for a total of 5500 training epochs. Nevertheless, we found that the loss decreased to a minimum around 3200 epochs, which is the checkpoint used for evaluation. The self-attention NN was trained on 467 samples (i.e. input/output pairs) for L=8 and 1001 samples for L=10, and performance was observed to vary noticeably based on the random seed used (where "random seed" refers to the initializer for the pseudorandom number generator(s) of the computer), corroborating the findings in [110]. A full list of hyperparameters can be seen in Tab. VI.

L	10	12	14	16	18	20	22	24	26	28	30
Self-Attention NN, $U = 1$	N/A	66.19	73.51	76.63	80.63	83.62	84.93	82.55	81.55	81.70	79.89
${\rm SIREN}, U=1$	60.79	64.34	73.25	73.15	73.27	77.48	88.70	75.72	77.21	78.81	79.25
${\bf SIREN}, U=2$	82.94	83.27	83.16	83.84	83.41	92.59	86.27	85.84	86.33	86.36	92.78
${\rm SIREN}, U=3$	81.25	81.64	82.30	82.11	82.61	83.00	82.79	82.96	82.97	83.18	83.24

TABLE VII. % Reduction (as defined in Eq. (24)) across various system sizes ( $10 \le L \le 30$ ) for the Hubbard model. For U = 1, results are shown using both the self-attention NN and the SIREN, while for U = 2 and U = 3 we only obtained results for the SIREN due to limited training data.

#### b. SIREN

As aforementioned, each set of "significant" points forms a tensor of shape  $L \times L \times 2 \times 2$ . To take full advantage of dimensionality reduction, we trained a separate SIREN for every index of the  $2 \times 2$  matrix at each k that had significantly nonzero elements. That is, each SIREN was trained on an  $L \times L$  matrix (for the Hubbard model, each of the SIRENs was trained on L=8), and the outputs were then combined to reconstruct the original shape. Of course, just like with the Richardson model in Eq. (B121) - Eq. (B122), we extend the size of the matrix to  $(L+1) \times (L+1)$  by "wrapping" around the first element of each dimension in order to satisfy normalization constraints. Due to the large search space of possible hyperparameter configurations, we used Tree-Structured Parzen Estimation (TPE) [119] through the Optuna and RayTune libraries to optimize hyperparameters individually for each SIREN model trained in this way.

#### c. Results

After training, we evaluate acceleration by re-running HF initialized with the NN-predicted final 1-RDM and reporting the percent reduction in iteration count relative to HF started from a random 1-RDM under the same tolerance and settings. Results are shown in Tab. VII